# Representations of Boundary Layer Cloudiness and Surface Wind Probability Distributions in Subtropical Marine Stratus and Stratocumulus Regions

A Dissertation
Presented to
The Academic Faculty

By

Yanping He

In Partial Fulfillment
Of the Requirements for the Degree
Doctor of Philosophy in Atmospheric Dynamics

Georgia Institute of Technology

May 2007

**Representations of Boundary Layer Cloudiness and Surface Wind Probability Distributions in Subtropical Marine Stratus and Stratocumulus Regions**

Approved by:

Dr. Robert E. Dickinson
School of Earth and Atmospheric Science
*Georgia Institute of Technology*

Dr. Judth Curry
School of Earth and Atmospheric Science
*Georgia Institute of Technology*

Dr. Irina Sokolik
School of Earth and Atmospheric Science
*Georgia Institute of Technology*

Dr. Rong Fu
School of Earth and Atmospheric Science
*Georgia Institute of Technology*

Dr. Peter Webster
School of Civil and Environmental Engineering
*Georgia Institute of Technology*

Date Approved: January 9, 2007

To beautiful nature and sweet family

I am the daughter of Earth and Water
And the nursling of the Sky;
I pass through the pores of the ocean and shores;
I change, but I cannot die.
For after the rain when with never a stain
The pavilion of Heaven is bare,
And the winds and sunbeams with their convex gleams
Build up the blue dome of air,
I silently laugh at my own cenotaph,
And out of the caverns of rain,
Like a child from the womb, like a ghost from the tomb,
I arise and unbuild it again.

“The Cloud”, by Percy Bysshe Shelley.

# ACKNOWLEDGEMENTS

I would like to extend my deepest appreciation for my supervisor Prof. Robert Dickinson, for his encouragement, support, and patience on my thesis; for the careful thought he gave to the numerous issues that arose along the way; for his splendid and insightful class notes on atmospheric boundary layer and convection; and for guiding me in such a way that I could develop my own ideas and the ability to independent work. His genius, great passion, and enormous creativity make my study an exceptional beautiful journey.

It is such a pleasure to have Prof. Rong Fu, Prof. Peter Webster, Prof. Judth Curry, and Prof. Irina Sokolik on my PhD committee. Prof.Webster and Prof. Sokolik are splendid teachers who make knowledge-passing process such an enjoyable and wonderful experience. The three-tier forecast system developed by Prof. Webster and his group is really amazing. Prof. Curry is the leader of our school; she helps to provide a nice and efficient working environment between faculty and students. Prof. Fu is always there ready to support students. She encouraged me particularly during my hardest time, and provided me a nice model as a female scientist.

I feel so lucky to have some very good friends accompanied me, encouraged me, and supported me during my research study. This thesis would not have been achievable without the support and advice by many of my friends and colleagues. My great thank gives to my friend Prof. Yongjiu Dai in Beijing Normal University, for his continuous support, encouragement, inspirations, discussion, and version. I thank Prof. Xubin Zeng and his lovely wife Dr. Qingqiu Shao in the University of Arizona to initiate my passion for

atmospheric science and to provide insight suggestions on many scientific questions. I thank my university classmate Dr. Baijun Tian in the Jet Propulsion Laboratory for frequent discussions on cloud in the tropics and for providing me the radiation data and surface flux data in the tropical Pacific; I thank Prof. William Rossow, Dr. Yuanchong Zhang, and their group in GISS for providing me ISCCP FP radiation profile data; I thank Prof. Judith Curry and her group in UC to provide me radiation profile data in tropics; I thank Dr. Robert Woods in the University of Washington for discussion on MSC issues and for providing MODIS high resolution cloud data; I thank Prof. Adam Monahan in the University of Victoria for suggestions and feedbacks on stochastic dynamics of ocean surface winds; I thank Dr. Wenhong Li for discussions of tropical dynamics and providing much support; I thank Dr. Shaikh and Mingxuan Chen for their expert helps in Unix script writing and data fetching; I thank Dr. William Shem for correcting my English and creating a nice office environment. I greatly appreciate the members of Dickinson's group and Fu's group for frequent supports and contributions: Dr. Wanru Wu, Dr. Hui Wang, Dr. Yuhong Tian, Dr. Liming Zhou, Dr. Qing Liu, Dr. Mi Zhou, Dr. Yan Huang, Dr. Haishan Chen, Dr. Huiling Gao, Yan Zhang, and Jiangfeng Wei.

At the moments of completing this dissertation, my deepest thoughts are addressed toward my sweet husband. He is the sunshine during my darkest days; he encourages me to reveal nature's secret; he carefully cultivates my childish part and helps me to maintain great curiosity and passion toward science. I also want to express my deep love toward my parents and my sister who encourages me and give me the freedom to explore the world in my own way.

This research is sponsored under the National Science Foundation.

# TABLE OF CONTENTS

# LIST OF TABLES

# LIST OF FIGURES

FIGURE

# SUMMARY

A simple low cloud cover scheme is developed for the subtropical marine stratus and stratocumulus (MSC) regions. It is based on a modified CIN concept named the Lower Troposphere Available Dry Inhibition Energy (ADIN). The e-folder time for the local change of ADIN is found to be approximately 6 to 7 hours. On monthly and longer timescales, local productions of ADIN are balanced by local destructions of ADIN within lower troposphere. Dynamical transport of environmental dry static energy and surface evaporation lead to the variations of cloud top radiative cooling, which is a linear function of low cloud cover. Data analysis suggests that total ADIN dynamical transport plays the most important role in determining the seasonal variations and spatial variations of low cloud amounts。

The new scheme produces realistic seasonal and spatial variations of both EECRA ship observation and satellite observations in all MSC regions. It explains 25% more covariance than that using Klein-Hartmann (KH) scheme for monthly ISCCP low cloud amount near the Peruvian and Canarian region during the period from 1985 to 1997，it better represents the relationship between ENSO index and low cloud cover variations near the Peruvian region. When implemented into NCAR CAM3.1, it systematically reduces the model biases in the summertime spatial variations of low cloud amount and downward solar radiation in the Peruvian, California, and Canarian regions. Model simulated summertime cloud liquid water path, large scale precipitation, and surface fluxes are also significantly changed.

A single predictor named Lower troposphere available thermal inhibition energy (ATIN) is also shown to be more skillful than the lower tropospheric stability in diagnosing low cloud stratiform clouds in the monthly and seasonal timescales. On synoptic timescale, dynamical transport of available dry inhibition energy and surface evaporation are better correlated with marine low cloud amount variations than ATIN and lower troposphere stability.

The influence of boundary layer clouds, ocean surface SST, and large scale divergence on the stochastic dynamics of local ocean surface winds are addressed using QuikSCAT and AIRS satellite observations and a simple conceptual model in the southeast Pacific. The ocean surface pressure gradient depends on both the boundary layer height and temperature inversion strength. Marine boundary clouds are diagnosed using the cloud cover scheme developed in Chapter 2. The model successfully reproduces the observed mean state, the standard deviation, and skewness of local surface wind speeds in the southeast Pacific.

# CHAPTER 1

# INTRODUCTION

## 1.1 Significance of Marine Boundary Clouds in Climate Modeling

Marine stratus and stratocumulus are beautiful objects which show the complexity and order of nature. As an integral component of the climate system, they work closely with large scale circulations and underlying ocean surface to keep nature in a harmonious mean state. They are central to many questions related to climate change, particularly to global warming, which is one of greatest challenges facing global society. Even under conservative projections, climate models predict several degrees of warming this century, which could change precipitation patterns, melting polar ice sheet and so raise ocean levels, destroy ecosystems, and disrupt agriculture. Understanding and accurate predictions of global warming and energy redistributions play key roles in developing the most effective strategies to battle global warming. Hence, marine boundary clouds have to be realistically represented in climate models to accurately predict climate change.

The extensive and remarkably persistent marine stratus and stratocumulus (MSC) in the cold tongue and the east coast of subtropical oceans exert a strong cooling effect in the local and global heat balance. As low optically thick clouds, their albedo effects act like a huge refrigerator and significantly cool the ocean surface at the rate of approximately -1.00 W $m^{-2}$ per percent cloudiness in stratus regions (Klein, 1993). It has been suggested that a 10%~15% increase of low level cloud fraction could balance the global warming due to doubling $CO_2$ (Slingo, 1990).Three current leading US GCMs suggest a dominant role for boundary layer clouds in the change of net cloud radiative

forcing (Wyant MC, et. al. 2006). Indeed, marine boundary clouds are at the heart of tropical cloud feedbacks; however current global climate models disagree the most with observations in the net radiative forcing and cloud albedo change due to sea surface temperature change (Bony S, and Dufresne JL, 2005). One of biggest challenges is to realistically represent marine boundary clouds in global climate models. To determine when and where low clouds will be formed in large scale environments is to understand how boundary layer clouds interact with large scale circulation and ocean surface SST in marine stratus and stratocumulus regions.

## 1.2 Previous Studies on the Influence of General Circulation and Ocean Surface SST on Marine Boundary Clouds

Previous theoretical studies of MSC formation and breakup have been focused on the role of local boundary layer turbulence in the formation and dissipation of marine boundary clouds. Proposed mechanisms have been related to the strength of temperature inversion, cloud top radiation cooling, cloud top entrainment, and drizzle effects in the subcloud layer (Lilly 1968, Deardorff 1980, Randall 1980, Betts and Boers 1990, Bretherton and Wyant 1997). Small scale models such as single column models, large eddy models, and cloud resolving models have been used to study the cloud processes under varying large scale boundary conditions (see Moeng et al. 1996 for state of the art model intercomparisons). These small scale models are appropriate to study local thermodynamic processes in the timescales of hours to days with fixed large scale parameters as boundary conditions. They are not able to simulate interactions of the general circulation with marine boundary clouds.

Spectral analysis of nine years of ISCCP D-series data reveals that seasonal to annual timescales dominate most of the time variability of cloud properties (Rozendaal and Rossow, 2003), suggesting that the majority of marine low cloud variations are influenced by large scale circulations and their interactions with local boundary turbulence, rather than being a response to local turbulence alone. Previous observational studies have found empirical relationships between low stratiform cloud amounts and large scale circulations associated with ocean surface wind, subsidence, large scale divergence, and horizontal advection on synoptic, seasonal, and interannual timescales. The observed relationship among low cloud structure, sea surface temperature, and large scale circulation was investigated in the summertime Northeast Pacific (Klein, Hartmann, and Norris, 1994). Summertime interannual variations of low cloud amounts were better correlated with local upper air temperature and SST that was 24-30 hours upwind than with the local SST and free air temperature. A positive anomaly of boundary layer cloudiness was related to a stronger subtropical high because the later results in increased surface wind, large scale subsidence, and cold advection. Seasonal and interannual variations of stratiform cloud from ship records were studied by Bajuk and Leovy (1998) using ship records for the tropical Pacific and Indian oceans during the period from 1952 to 1992. Cloud frequency anomalies were found to be related to anomalies in ocean surface SST and surface wind divergence. The strongest stratiform and convective cloud frequency was associated with the seasonal shift of the ITCZ and SST. Synoptic variations of low stratiform cloudiness were found to be most strongly correlated with cold temperature advection, cloud top temperature inversion strength, and cloud layer relative humidity (Klein 1997).

Influences of large scale circulations and underlying ocean surface on variations of marine low clouds have been confirmed by observational study and regional atmosphere model sensitivity tests in the southeast Pacific (Xu et al, 2004, 2005). The observed subseasonal variations of marine boundary clouds were closely related to surface wind speed, lower troposphere water vapor, sea surface pressure, and 500hpa geopotential height. Large scale divergence and the cloud top temperature inversion were affected by the Andes Mountains. When the mountain was removed during a model experiment, the large scale divergence became weaker, and the temperature inversion height was lower, resulting in less marine stratus and stratocumulus formed within the boundary layer, and more solar radiation reaching the ocean surface in the southeast Pacific. Previous observational studies and model simulations have provided evidence relating the variations of marine boundary clouds to the large scale environment. To proceed, a physical picture has to be developed to represent marine cloud fractions based on large scale circulations and local thermal structures.

## 1.3 A Simplified Physical Picture of Convection Interacting with Large Scale Flows and Ocean Surface SST over Tropical and Subtropical Oceans

### 1.3.1 Observed Seasonal Variations of Marine Boundary Clouds and Large Scale Circulations over Subtropical Oceans

Marine stratus and stratocumulus clouds are integral components of the climate system. They are tightly coupled with the tropical circulation and local thermal structures, and affect both the mean state and variability of tropical climate change. When the Hadley circulation transports moist static energy out of the tropics, clouds are formed locally to adjust the atmosphere back to its preferred mean states. It has been suggested

that the net cloud forcing, not the surface latent heat flux, nor the clear sky radiation forcing, provides the major local energy source to balance the divergence of annual mean atmospheric moist static energy (MSE) in the warm pool region (Tian et al 2001, Tian and Ramanathan 2002). Deep convection and high clouds form in the ascending branch of Hadley circulation, exert positive 70 W $m^{-2}$ energy within the atmosphere, and a negative 70 W $m^{-2}$ CRF at the ocean surface. Marine boundary layer clouds form in the descending branch of Hadley circulation, with strong or moderate subsidence and a supply of moisture from the ocean surface with vertical mixing throughout the atmospheric boundary layer (ABL). When extra moist static energy is transported from the tropics into this region, MSC has to be developed to cool the atmosphere. From surface observations, the statistical structure of the seasonal cycle of MSC off the Peruvian region is characterized by two stable modes with quick transitions from one mode to another (see Figure 27 of Kiehl et. al, 1997).

Figure 1.1 describes the seasonal variations of Hadley circulation and boundary layer clouds in the southeast Pacific. The seasonal march of climate over the tropical Pacific is dominated by the seasonal variation of solar radiation. In boreal summer (June to November), maximum solar radiation is located in the northern tropics; the seasonal Hadley circulation (its annual mean removed) has its ascending branch near 10 degree north, and its descending branch in the southern subtropics (Dima and Wallace, 2003). MSC is at its seasonal maximum, the ITCZ becomes most active and reaches its northern-most position; meanwhile the equatorial upwelling of cold, nutrient-rich water is strongest in the cold tongue region, and the SST off the Peruvian coast is colder than its annual mean. In boreal winter (January to May), the ascending branch of seasonal Hadley

circulation is located in the southern tropics. MSC is at its seasonal minimum, the ITCZ is much weaker, and the SSTs are warmer than average. At this time, the temperature difference between South America and the surrounding ocean is large, and deep convection is significantly enhanced in the Amazon; the wet season has begun over South American. During transition periods (May to June), the seasonal Hadley circulation suddenly jumps from the boreal summer cell to the boreal winter cell. The transition of MSC should follow this jump during this period. From surface observations, the statistical structure of the seasonal cycle of MSC off the Peruvian region is characterized by two stable modes (one from January to May with Low MSC, another from June to December with High MSC) with quick transitions from one mode to another (see Figure 27 of Kiehl et. al, 1997).

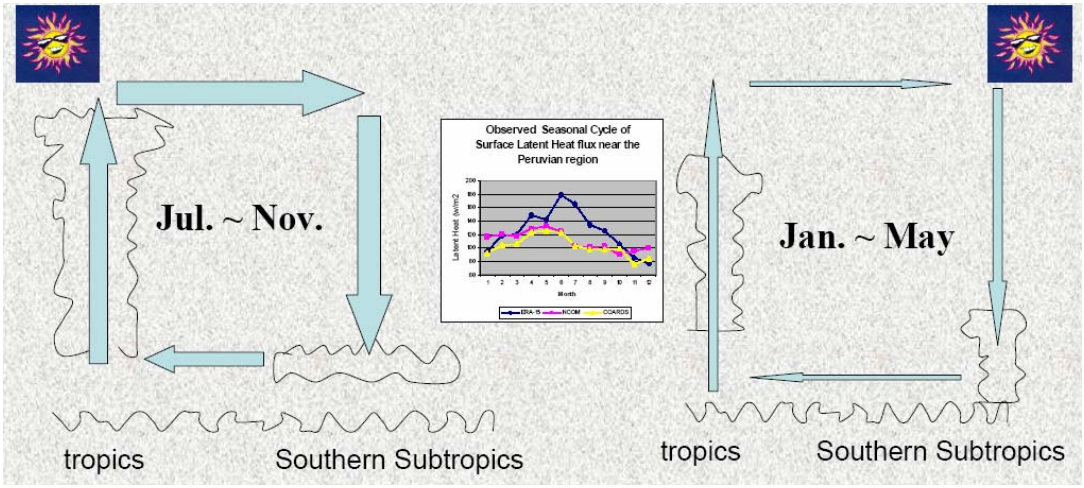


**Figure 1.1** Cartoon of seasonal variation of Hadley circulation and clouds in the southeast Pacific; the left one is during the season of July to November; the right one is during the season of January to May. The seasonal cycle of surface latent heat flux from ERA40 (blue), NCOM (pink), and COADS (yellow) is plotted in the middle.

In summary, the mean climate over the tropical Pacific is characterized by the bimodal structure induced by the seasonal march of solar radiation. As one important component in atmosphere-ocean land interaction, MSC also undergoes a similar bimodal structure. Lower troposphere stability has been used to diagnose the low stratiform cloud amounts in previous simple box models and some GCMs; however, it failed to simulate the "two steady state one jump" seasonal pattern of MSC near the Peruvian region, and underestimated low cloud amounts in most MSC regions. How can we better represent marine low clouds based on the large scale environments? What physical picture can link low cloud amounts with large scale circulations and local thermal structures?

### 1.3.2 Previous Studies on the Interaction of Deep Convection with Large Scale Flows

Previous studies have been focused on answering to what extend and how deep convection is controlled by large scale circulation in the tropics. Deep convection occurs when a near surface parcel with higher moist static energy overcomes an energy barrier called the Convective Inhibition Energy (CIN) and is lifted above its lifting condensation levels (LFC). The parcel then undergoes a spontaneous ascent until it reaches the Level of Neutral Buoyancy (LNB). The available energy released from LFC to LNB is called the Convective Available Potential Energy (CAPE). The occurrence of deep convection is related to both the change rate of CAPE and CIN. Most previous work has been focused on equilibrium control, which assumes that the occurrence rate of deep convection is controlled by the production and destruction of CAPE due to slowly varying large scale circulation. Quasi-Equilibrium (QE) of the cloud work function was proposed by Arakawa and Schubert (1974) as a cumulus closure assumption for global

climate modeling. Its key idea is that convective and non-convective processes are nearly balanced, so that the available energy measured by the cloud work function (Arakawa and Schubert 1974), CAPE (Emanuel 1994), or by moist static energy (Randall and Wang 1992) is quasi-invariant. Many tropical convective models have been developed based on QE thermodynamic closures (Zhang and McFarlane, 1995; Neelin and Zeng, 2000).

The QE hypothesis is valid if the adjustment time for convection to consume the available energy CAPE is much faster than that of large scale forcing. It is valid for the deep convection mode at the largest space scale and climate time scales when the atmosphere is in radiative-convective equilibrium. On smaller space and time scales, active control theory has been proposed to determine the large scale variations of deep convection (Mapes and Houze, 1992). It is hypothesized that the occurrence rate of deep convection is controlled by the triggering rate of small scale boundary layer lifting processes to overcome the convective inhibition energy CIN. A familiar example of active control is the existence of the trade wind inversion near 800 hpa which acts to prevent the formation of deep convection over large fractions of the tropical and subtropical oceans. Once deep convection is developed, then later it acts to reduce the available energy and to adjust the environmental density profile toward a preferred mean state.

### 1.3.3 A Synthesized Picture for Interactions of Deep Convection and Marine Boundary Clouds with Large Scale Flows

Based on the observed seasonal variations of marine boundary clouds and tropical circulations and previous theoretical studies, a highly idealized physical picture can be

summarized in Figure. 1.2 to describe interactions of clouds with large scale flows over tropical and subtropical oceans.

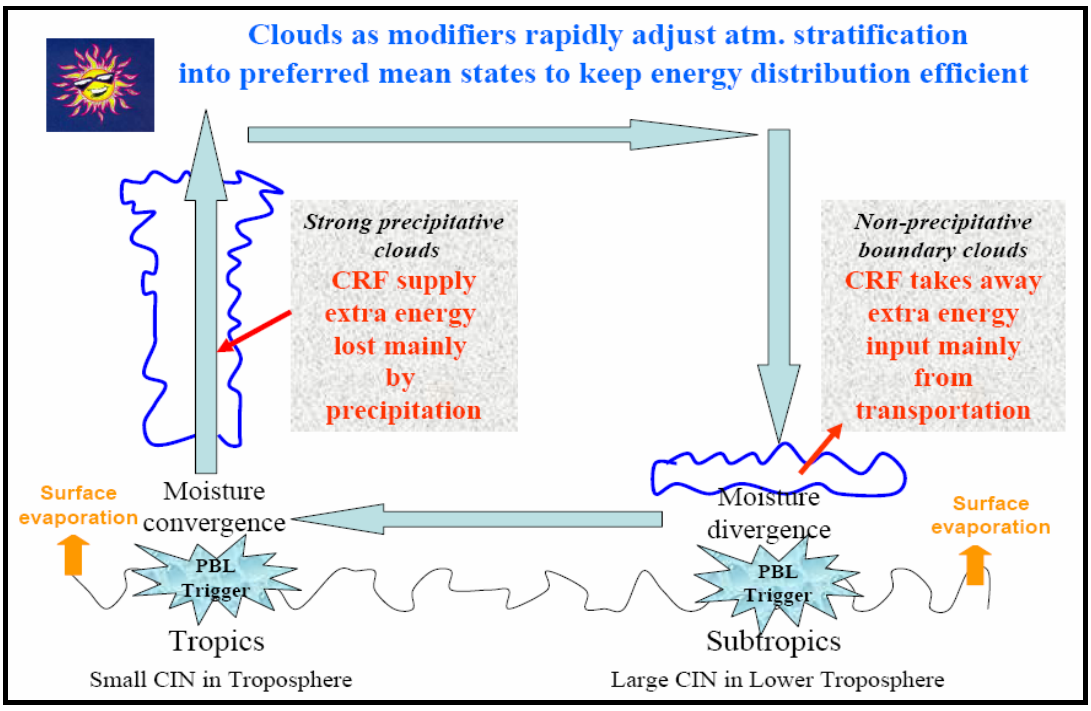


**Figure 1.2** The idealized picture for interactions between clouds and large scale flows.

One fundamental feature of the tropical atmosphere is its redistribution of energy from sources to ex-tropical regions. Clouds interact with large scale flows in order to keep this energy distribution efficient. Surface heating is maximum in the tropics and relatively weak in subtropical regions due to the distribution of solar heating. The atmospheric stratification is characterized by large Available Potential Energy (APE) and small Convective Inhibition Energy (CIN) in the tropics and small APE but large CIN in subtropics. When the boundary layer is supplied with similar amounts of energy, then

convection can be developed deeply from the near surface to the upper troposphere near the equatorial region but it is restricted to beneath the trade wind inversion in the subtropical regions due to large CIN. In this way, huge amounts of dry static energy are transported from deep convection regions into subtropical shallow convection regions. In the ascending branch of the Hadley circulation, cloud radiative heating due to solar heating absorption supplies extra dry energy to balance the moist energy lost by strong precipitation; in the subsidence branch of Hadley circulation, marine boundary clouds are developed to take away extra amounts of dry energy transported from tropics through strong cloud top radiative cooling. In both regions, clouds act as modifiers to rapidly adjust atmosphere stratification back to its preferred mean state to keep the tropical heat engine efficient. Quasi equilibrium theory and active control theory have been developed in previous studies to link deep convection with large scale flows. This dissertation completes the physical picture by successfully coupling the above ideas with the properties of marine boundary clouds.

## 1.4 Thesis Contributions

### 1.4.1 New Cloud Cover Schemes Linking Large Scale Circulations with Local Thermal Structures

A cloud cover scheme is a relationship or a simple model linking the partial grid cloud fraction to the resolvable GCM state variables. To develop such a scheme for large scale models is to seek one or a few factors which broadly determine where and when the boundary layer clouds form in large scale environments. In Chapter 2, "A simple low cloud cover scheme based on lower tropospheric stability and convective inhibition energy transport in the subtropical marine stratus and stratocumulus regions Part I:

Scheme development," a conceptual model is developed to link boundary layer clouds with large scale circulation and local thermal structures. The model is based on a modified concept named Lower Troposphere Available Dry Inhibition Energy (ADIN). In monthly and longer timescales, local production of ADIN is balanced by local destructions of ADIN within the lower troposphere. Dynamical transport of environmental dry static energy and surface evaporation lead to variations of cloud top radiative cooling, which is a linear function of low cloud cover. Data analysis suggests total ADIN dynamical transport plays the most important role in determining the seasonal variations and spatial variations of low cloud amounts。

Chapter 3 develops "A simple low cloud cover scheme based on lower tropospheric stability and convective inhibition energy transport in the subtropical marine stratus and stratocumulus regions part II: seasonal and interannual simulations." The new scheme developed in Chapter 2 produces realistic seasonal, interannual, and spatial variations of both EECRA ship observations and satellite observations in all MSC regions. It better represents the relationship between the ENSO index and low cloud amount variations near the Peruvian region. When implemented into NCAR CAM3.1, 15% to 20% more low cloud has been simulated in the four MSC regions. The new scheme systematically reduces the model biases in spatial distributions of low cloud fraction and net radiation fluxes at the surface in all MSC regions.

### 1.4.2 A Simple Predictor Based on Available Thermal Stability for Low Stratiform Cloud Amounts

In Chapter 4, "On the relationship between lower troposphere gross dry thermal stability and low stratiform cloud amount", a simple index based on lower troposphere

thermal inhibition energy (ATIN) is defined and used to diagnose the low stratiform cloud amount on monthly and seasonal time scales. Compared with EECRA ship observations and ISCCP satellite observations, ATIN is more skillful in simulating grid monthly and seasonal low cloud amount than an expression that uses lower troposphere stability $\Delta\theta_{700}$. The largest improvement is in the regions of China where EECRA has the most complete cloud record; and it also significantly improved the low cloud amount simulations near the Peruvian, North Atlantic, and North Pacific regions. However, on synoptic timescales, dynamical transport is most closely related to ISCCP low cloud amount variations. Therefore, the cloud cover scheme developed in Chapter 2 performs better than any single predictor such as ATIN or $\Delta\theta_{700}$.

### 1.4.3 Influences of Boundary Layer Clouds, SST, and Large Scale Divergence on Mean States and Probability Distributions of Surface Winds

Marine stratus and stratocumulus are formed over subtropical cold oceans with sufficient moisture transported from the ocean surface. Surface latent heat flux is primarily determined by surface wind speed and ocean surface temperature. Surface pressure gradient is determined by both boundary layer height and SST variations. Previous observational studies found a close relationship between ocean surface evaporation, surface winds, and MSC cloud variations. During the seasonal transition of May to June, southerly winds are anomalously increased; extensive MSC is rapidly developed near the Peruvian region due to proposed positive feedback among surface wind-evaporation-MSC (Nigam et al, 1997), pushing the seasonal climate from one equilibrium state into another equilibrium state. During the ENSO event, ocean surface SST becomes anomaly warm near the Peruvian region and surface evaporation is

enhanced in large fractions of the tropical Pacific. The equatorial easterly wind is weaker, and the center of deep convection is shifted from the western Pacific to the central Pacific. In Chapter 5, the marine boundary layer cloud cover scheme developed in Chapter 2 is successfully coupled with a simple ocean surface wind model to study the influence of ocean SST, large scale divergence, and marine boundary layer clouds on ocean surface winds in the southeast Pacific. The developed 1D simple conceptual model simulates well the observed relationships among ocean SST, marine boundary layer cloud amount, and mean states and the probability distribution of ocean surface winds in the southeast Pacific regions. Implications for Walker circulation, Kelvin wave, and the Rossby adjustment based on the linearized 2D version of this model are briefly described.

# CHAPTER 2

# A SIMPLE LOW CLOUD COVER SCHEME BASED On LOWER TROPOSPHERIC STABILITY and AVAILABLE DRY INHIBITION ENERGY TRANSPORT IN THE SUBTROPICAL MSC REGIONS Part I: SCHEME DEVELOPMENT

## 2.1 Introduction

Marine Stratus and Stratocumulus (MSC) clouds have an important influence on the global radiation budget, ocean-atmospheric coupling, and the mean atmospheric circulation. Their albedo affects the amount of radiation reaching the earth's surface; their strong cloud top radiative cooling is the main driver for the cloud-top boundary layer turbulence over the cold ocean surface, and their persistence over the subtropical ocean surface enhances the latitudinal gradient of atmospheric long wave radiative cooling and reinforces the radiative forcing of the tropical atmospheric circulation. However, the development of a realistic cloud cover parameterization in a global climate model is a major challenge, and current cloud cover schemes underestimate low cloud fraction in almost all GCMs (Kiehl et al. 1998; Siebesma et al. 2003; Zhang et al. 2005).

Most past cloud cover schemes in GCMs have been relative humidity (RH) based. However, the observed relationships between low cloud amount and various meteorological variables suggested that the lower atmospheric stability is a better indicator for low cloud cover in the MSC regions on daily to inter-annual timescales (Slingo 1987; Klein and Hartmann 1993; Klein 1997; Wood and Hartmann 2005). A recent review work of Steven (2005) summarizes the boundary layer structure as either a one-layer well-mixed boundary structure or a two-layer decoupled boundary structure. In

both cases there exists a large thermal contrast between the underlying moist and cold ocean surface and the upper laying dry and warm free atmosphere. Lower tropospheric stability is a good indicator for describing this thermal contrast, the linear relationship proposed by Klein and Hartmann (1993, after here called the KH scheme) has been used in the NCAR CCM3, CAM3, and simple box models to simulate clouds and to study atmospheric-cloud interaction in climate sensitivity and global warming (NCAR CAM3.1 document; Clement & Seager 1999; Larson, Hartmann, and Klein 1999). However, the KH scheme underestimates low cloudiness in MSC regions and it can not explain the "two-steady states one jump" seasonal patterns observed near Peruvian region (see Figure 28 of Kiehl et al.1998). Betts proposed a simple linear parameterization for cloud fraction in terms of mixing line stability for shallow cumulus and stratocumulus (Betts 1990). It needs high vertical resolution within cloud layers which is difficult to be implemented in GCMs with low vertical resolution. Both stability based schemes assume that boundary layer cloud variation is uniquely decided by atmospheric thermal structure. They miss feedbacks between low cloudiness and their large scale circulation.

Previous observational studies suggested that the low cloud variations are correlated not only with stability but also with various meteorological variables associated with large scale circulation such as large scale subsidence, near surface temperature advection, the strength of subtropical high, and ocean surface wind speed (Klein, Hartmann, and Norris 1994; Klein 1997; Norris 1997; Bajuk and Leovy 1998). In the subsidence branch of Hadley circulation, a large amount of dry static energy is transported from the free atmosphere into the marine boundary layer. Boundary layer cloud is developed to cool the lower troposphere by cloud top radiative cooling, which further enhances the moist

and mass transport from ocean surface. The development and the dissipation of boundary layer cloud variations are decided by local thermal structure and large scale circulation. Physically consistent prognostic cloud cover schemes were developed for GCMs (Sundqvist 1988; Tiedtke 1993). These schemes are capable of fully coupling between clouds and the hydrological cycle, and they treat all types of cloud in a unified approach. However, these fully coupled schemes underestimate low stratiform clouds (Siebesma et al, 2003) and depend greatly on variables related to cloud entrainment, detrainment, and cloud microphysics, which are difficult to be verified and interpreted.

A new low cloud cover scheme is developed in this study linking boundary layer cloudiness variations with large scale circulation and local thermal structure in the subtropical MSC regions. Lower Troposphere Available Inhibition Energy (ADIN) is defined and the formation and destruction of ADIN are assumed to be balanced within the lower troposphere. CAPE and CIN are two primary thermodynamic parameters for assessing the occurrence of deep moist convection in the atmosphere. Previous study has focused primarily on the roles of CAPE and CIN in triggering, developing, and suppressing deep convection (Mapes and Houze, 1992; Chaboureau, Guichard, and Lafore, 2004; Tailleux and Grandpeix, 2004). Apparently no work has simulated marine boundary layer cloudiness based on CAPE or CIN. According to Parker (2002), the effects of CAPE and CIN on the thermal and humidity profiles of the atmosphere can be understood in terms of direct effects and indirect effects. A direct effect involves changes in the profile in the absence of parcel changes, and an indirect effect involves changes in air-parcel evolution in a developed convective boundary layer. Our study includes both

direct effects of environmental profile change by large scale circulation and diabatic forcing and indirect effects of air-parcel profile change by ocean surface SST.

The study combines both EERCA COADS ship observation with ISCCP D-series satellite observation, and focuses on understanding and representing low cloudiness in seasonal and inter-annual variations in the subtropical MSC regions. The structure of this chapter is as follows: the dataset used is briefly described in section 2.2; the low cloud cover scheme based on ADIN conservation is developed in section 2.3; Monthly low cloud amounts from EERCA, ISCCP D-series, and simulation results with the new scheme are presented in section 2.4; discussions and conclusions are given in section 2.5.

## 2.2 Data Descriptions

### 2.2.1 Cloud Cover Dataset from EECRA and ISCCP D-Series

The Extended Edited Cloud Report Archive (EECRA) provides 46 years (1952-1997) of ship cloud data which has passed through various data quality checking, and therefore is useful for cloud climatology study and satellite data validation. The suggested bias in the ship cloud data includes night/daytime detection bias, day-night sampling bias, clear-sky bias, and sky-obscured bias. Only the dominant cloud type is reported in ship cloud data, and the surface data is discontinuous in time and space. Table 1 is the number of EECRA COADS low cloud observations during the period of 1985 to 1997 in four MSC regions with horizontal resolution of $2.5^{\circ} \times 2.5^{\circ}$. It shows the irregularity of ship observations in these regions. Satellite data provides continuous observations in time and on all spatial scales. However, satellite data underestimate low cloudiness when there are high cloud and middle cloud presented above. It also has difficulty in detecting low level

**Table 2.1** Number Records of EECRA COADS Low Cloud Observations during the Period from 1985 to 1997

| | | | | | | |
|---|---|---|---|---|---|---|
| per | | | | | | |
| | 33 | 32 | 26 | 31 | 66 | 48 |
| | 15 | 28 | 38 | 37 | 63 | 141 |
| | 18 | 16 | 35 | 45 | 85 | 250 |
| | 15 | 23 | 25 | 64 | 203 | 665 |
| | 34 | 37 | 45 | 97 | 1237 | 1206 |
| | 196 | 105 | 75 | 189 | 695 | 913 |
| nam | | | | | | |
| | 155 | 180 | 51 | 831 | 902 | 122 |
| | 107 | 42 | 525 | 1571 | 143 | 161 |
| | 38 | 242 | 1838 | 161 | 178 | 118 |
| | 114 | 1728 | 504 | 194 | 65 | 115 |
| | 1228 | 960 | 257 | 106 | 77 | 154 |
| | 1493 | 165 | 108 | 111 | 165 | 216 |
| cal | | | | | | |
| | 284 | 210 | 184 | 156 | 161 | 179 |
| | 294 | 257 | 159 | 185 | 180 | 170 |
| | 189 | 333 | 303 | 179 | 130 | 131 |
| | 211 | 186 | 287 | 290 | 237 | 294 |
| | 438 | 279 | 299 | 458 | 635 | 705 |
| | 688 | 905 | 1122 | 1058 | 922 | 713 |
| can3 | | | | | | |
| | 284 | 210 | 184 | 156 | 161 | 179 |
| | 294 | 257 | 159 | 185 | 180 | 170 |
| | 189 | 333 | 303 | 179 | 130 | 131 |
| | 211 | 186 | 287 | 290 | 237 | 294 |
| | 438 | 279 | 299 | 458 | 635 | 705 |
| | 688 | 905 | 1122 | 1058 | 922 | 713 |

broken cloudiness or thin cirrus cloud (Rossow and Schiffer, 1991). The agreement between ISCCP and surface observations is excellent over the MSC regions. However, the ISCCP results are biased a few percent lower than the surface observations. To better understand low cloud variations, we use both EERCA ship data and ISCCP D1 satellite data in our study. This study focuses on observational data in subtropical marine stratus and stratocumulus regions during the periods from 1985 to 1997.

### 2.2.2 ISCCP FD Dataset

The three-hour daily ISCCP FD dataset used in this study was developed by Zhang, Rossow, Lacis, Oinas, and Mishchenko (2004) on an $2.5^{\circ}$ x $2.5^{\circ}$ global grid and at five pressure levels (surface, 680hpa, 440hpa, 100hpa, TOA) during the period of January 1985 to December 2000. The cloud amount and cloud property information uses the ISCCP D-series dataset. The FD dataset contains not only the satellite measured radiative flux at the top of atmosphere and at the surface, but also contains the vertical profiles of radiative flux obtained using satellite measured cloud information and a radiative transfer model. It contains three-hour cloud cover information and sea surface temperature from 1985 to 2000. In this study, the low cloud cover is the sum of cloud amounts in all low cloud types. This ISCCP FD dataset has been obtained directly from Zhang and Rossow. The information on the data inputs and data quality can be found in Rossow and Zhang (1995) and Zhang and Rossow (1995).

### 2.2.3 ERA-40 and NCAR NCEP Reanalysis Data

The six-hour surface flux, air temperature, specific humidity, and relative humidity at 1000hPa and air temperature at 700hpa used in this study are obtained from the

ERA-40 website at http://data.ecmwf.int/data/d/era40_daily/. The study period is from January 1985 to December 2000. The publications related to ERA-40 data quality can be found at http://www.ecmwf.int/publications/library/do/references/list/192.

The monthly mean data for surface fluxes, temperature, specific humidity and RH at 1000hPa, and 700hPa were obtained from NCEP-NCAR reanalysis during January 1985 to December 2000 (Kalnay et al, 1996).

This study focuses on the four subtropical regions. They are listed in Table 2.2.

**Table 2.2** Geographical Extent of Four Subtropical MSC Regions

| MSC regions | Locations |
|---|---|
| Peruvian | 5°–20° S, 80° –95° W |
| Namibian | 5°–20° S, 5° W–10° E |
| California | 17.5°–32.5° N, 120°–135° W |
| Canarian | 12.5°–27.5° N,45W–30W |

## 2.3 Low Cloud Cover Scheme

### 2.3.1 Concept and Available Dry Inhibition Energy Budget Equation

Marine stratus and stratocumulus are low-lying clouds typically formed near the boundary layer top in large scale subsidence regions, where there exists great thermal contrast between the overlying free atmosphere and underlying surface. Inter-annual variations of low cloud amounts are observed to be well correlated with lower troposphere stability (Klein and Hartmann, 1993); however cold advection and upstream

air conditions becomes more important for shorter timescale cloud amount variations (Klein, 1997; Mansbach and Norris 2006). A new physical picture is necessary to link lower troposphere stability and large scale circulation in order to better explain MSC amount variations on various time scales. It is the focus of this chapter.

Among all types of moist convection, MSC are most analogous to dry convection. To understand where and when MSC occur in the large scale flow let's begin our journey from the basic thermodynamics of dry convection. Convection typically happens when an air parcel is lifted upward from the surface. This is done when the parcel has positive vertical acceleration, which is associated with buoyancy force due to temperature and pressure perturbations as shown in the vertical momentum equation:

$$\frac{dw}{dt} = -g\frac{\rho'}{\rho} - \frac{\partial p'}{\partial z} + \upsilon\nabla^2 w \tag{2.1}$$

where $w$ is the vertical velocity, $\rho$ is the air density, $p$ is air pressure, $\upsilon$ is the kinematic viscosity, and primes denote deviations from a hydrostatic reference state. In a dry atmosphere, the density perturbation can be linearized when the pressure perturbation is neglected as

$$\frac{\rho'}{\rho_0} \approx -\frac{T'}{T_0} \approx -\frac{\theta'}{\theta_0} \tag{2.2}$$

where $T$ is the air temperature, and $\theta$ is the potential temperature. It is easy to tell from this equation that in a nondiffusive, inviscid, and horizontally homogenous fluid, at any point originally at rest, whether the fluid becomes stable, neutral, or unstable to a small perturbation depends on the potential temperature lapse rate $\frac{\partial\theta}{\partial z}$. When $\frac{\partial\theta}{\partial z} \le 0$, dry convection is developed to rearrange air parcels to produce neutral stability $\frac{\partial\theta}{\partial z} = 0$.

Water phase change has to be considered for moist convection. Therefore it is nature to measure the convective instability as the work done by a test parcel moving from an initial position $z_1$ to a final position $z_2$.

$$W(z_1, z_2) = \int_{z_1}^{z_2} g \frac{T_{env} - T_{pal}}{T_{env}} dz \tag{2.3}$$

Figure2.1 is the lower troposphere thermal structure in a typical MSC region. MSC is formed under a strong temperature inversion near the boundary layer top at $z_i$. With respect to Figure 2.1, $W(0, z_i)$ measures the positive area and is called the convective potential energy CAPE in most literature; and $W(z_i, z_T)$ measures the negative area on the thermodynamic diagram and is called the convective inhibition CIN for a parcel to move from somewhere near the boundary layer height to the trade wind inversion. CIN represents the amount of negative buoyant energy available to inhibit or suppress upward vertical acceleration. CAPE and CIN are key concepts for understanding how convection interacts with large scale flows in the tropical atmosphere.

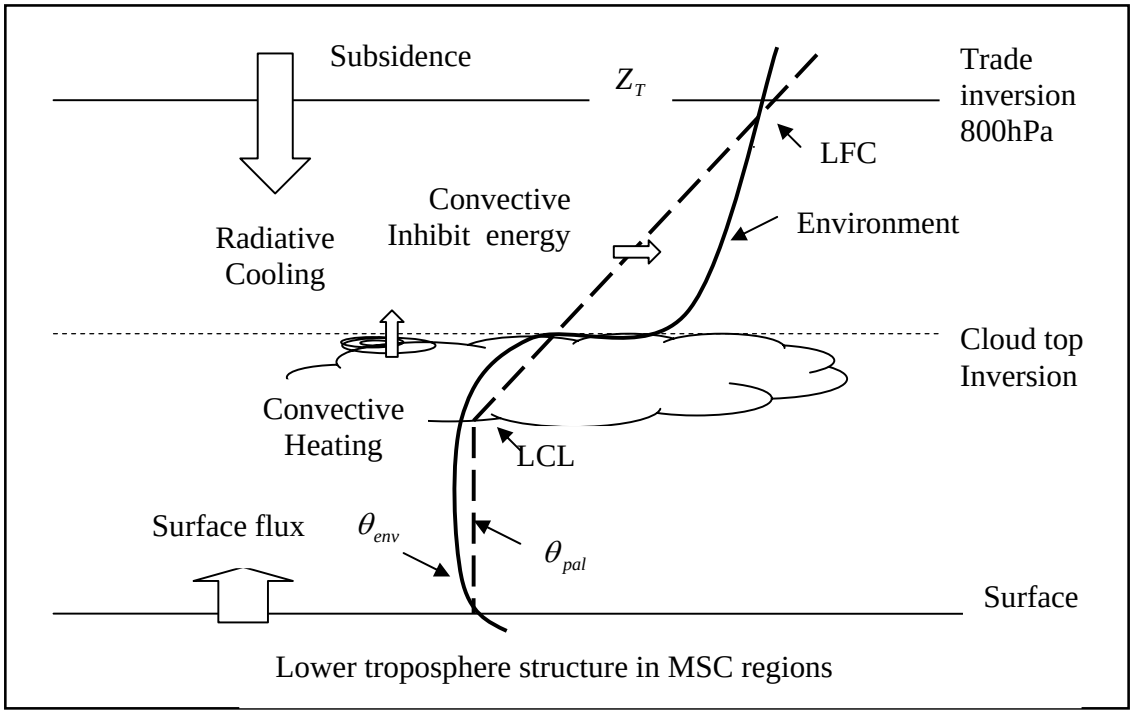


**Fig.2.1** Cartoon of lower troposphere thermal structure. The dashed line above the lifting condensation level (LCL) shows a pseudo-moist adiabatic, and the solid line shows the environmental potential temperature profile.

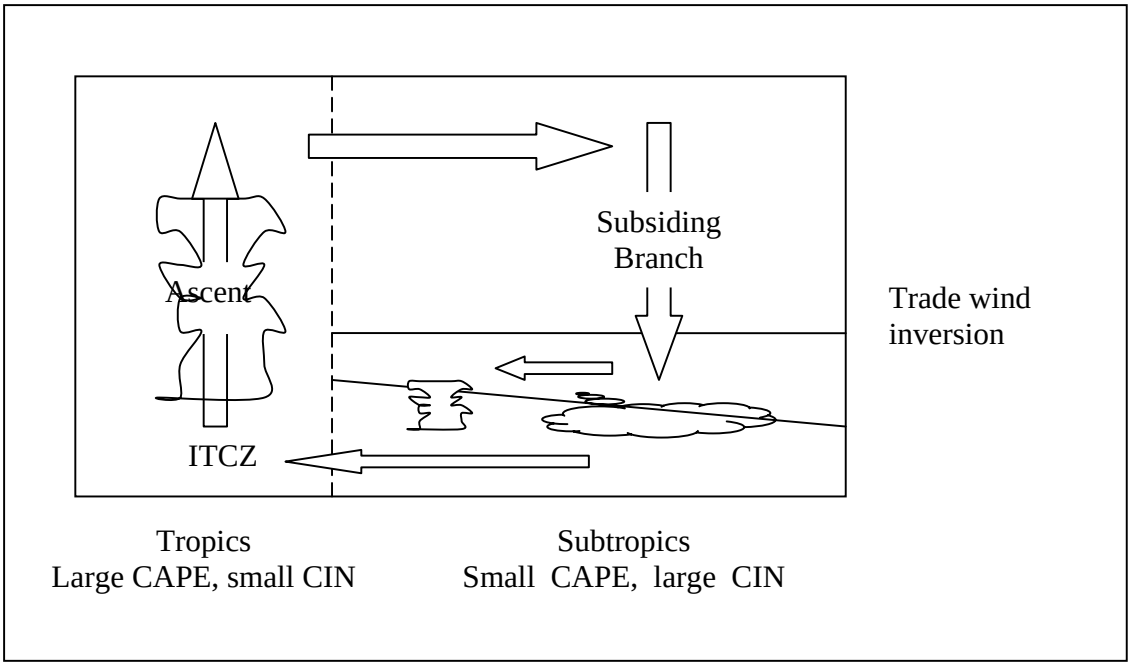


**Figure 2.2** The idealized single tropical circulation

Figure 2.2 is a highly idealized picture of tropical circulation. Solar radiation is strongest in the tropical region, and relatively small in the subtropical regions. The tropical atmosphere frequently becomes very unstable with large CAPE, deep convection is quickly developed to destroy CAPE and to adjust the air temperature to neutral stability. A large amount of dry static energy is transported from the upper troposphere into subtropical subsiding regions, where large scale subsidence warms the lower troposphere. A strong temperature inversion is formed near the boundary layer top, and strong returning flow brings sufficient moisture back into the tropics to fuel this tropical heat engine. CAPE is a good indicator for deciding where and when the deep convection occurs. The basis of convection parameterization in the past century has been the so called Quasi-Equilibrium (QE) hypothesis (Arakawa and Schubert 1974). The key idea of

QE is that $\partial CAPE/\partial t$ is small, so whenever the atmosphere becomes convectively unstable, deep convection is rapidly developed to adjust the temperature and humidity profile to nearly neutral stable. CAPE becomes a key player in current deep convection parameterizations of state of the art GCMs (Zhang and McLane, 1996). The QE hypothesis links deep convection with large scale flows, but it is less important for cloud parameterization in MSC regions where CAPE is very small. Indeed, subtropical MSC regions are dominated by clear sky with no deep convection but large CIN in the lower troposphere. Existence of this large CIN guarantees no convection is developed above the trade inversion in order to keep the engine efficient. Traditionally, CIN is defined as the amount of work the environment must do on the parcel to raise the parcel from its Lifting Condensation Level (LCL) to its Level of Free Convection (LFC). In the subtropical MSC regions, air parcels can be lifted from any position near the surface and can reach potentially any position near the trade wind inversion. To represent boundary layer cloud variations in global circulation models with low vertical resolutions, it is useful to calculate the net negative buoyancy changes from ocean surface to trade wind inversion typically at around 800mb over tropical oceans and at around 700mb over subtropical land. A new concept named Lower Troposphere Available Inhibition Energy (ADIN) is defined in this study to distinguish it from the traditional definition of CIN.

$$\int_0^{z_T} \rho g \frac{T - T_{pal}}{T} dz \approx \frac{g}{\theta_0} \int_0^{z_T} \rho\left(\theta - \theta_{pal}\right) dz = \frac{g}{c_p \theta_0} ADIN \tag{2.4}$$

The time derive of ADIN is

$$\frac{d}{dt} ADIN \approx \frac{d}{dt} \int_0^{z_T} \rho c_p \left(\theta - \theta_{pal}\right) dz \tag{2.5}$$

To understand the evolution of ADIN and how it links marine boundary cloudiness with large scale flow, let's first derive the conservation equations for thermodynamic energy and moisture. The theoretical foundation of our understanding of MSC is Lilly's mixed-layer theory (1968). In his well-mixed layer model for dry cloud, the conservation equations for thermodynamic energy and total moisture are written as:

$$\frac{d}{dt}\int_0^{Z_i}\theta dz = S_\theta^{PBL} + \overline{w'\theta'}^{0} - \overline{w'\theta'}^{z_i} \tag{2.6}$$

$$\frac{\partial}{\partial t}\int_0^{Z_i} q dz = S_q^{PBL} \tag{2.7}$$

where $\frac{dx}{dt}$ is the total time derivative of variable $x$, $\frac{\partial x}{\partial t}$ is the local time derivative of variable $x$, $S_\theta^{PBL}$ and $S_q^{PBL}$ are the sources of $\theta$ and $q_l$ within boundary layer, $\overline{w'\theta'}$ is eddy transport of temperature fluctuations and humidity fluctuations respectively. The vertically integrated dry energy and total moisture equations for the free atmosphere from boundary layer top to trade wind inversion can be expressed similarly.

$$\frac{d}{dt}\int_{Z_i}^{Z_T}\theta dz = S_\theta^{free} + \overline{w'\theta'}^{Z_i} - \overline{w'\theta'}^{z_T} \tag{2.8}$$

$$\frac{\partial}{\partial t}\int_{Z_i}^{Z_T} q dz = S_{q_l}^{free} \tag{2.9}$$

The vertically integrated dry energy and total moisture within the lower troposphere are a combination of the equations (2.6) and equation (2.8).

$$\frac{d}{dt}\int_0^{Z_T}\theta dz = \frac{d}{dt}\int_0^{Z_i}\theta dz + \frac{d}{dt}\int_{z_i}^{z_T}\theta dz = S_\theta^{free} + S_\theta^{PBL} + \overline{w'\theta'}^{0} - \overline{w'\theta'}^{z_T} \tag{2.10}$$

$$\frac{\partial}{\partial t}\int_{Z_i}^{Z_T} q dz = \frac{\partial}{\partial t}\int_{0}^{Z_i} q dz + \frac{\partial}{\partial t}\int_{z_i}^{z_T} q dz = S_q^{free} + S_q^{PBL} \tag{2.11}$$

At the trade wind inversion top around 800mb over subtropical oceans, the turbulent fluctuations are close to zero. The sources of $\theta$ within the lower troposphere are net convective heating $Q_c$ and net radiatve cooling $R$ .

$$S_\theta^{free} + S_\theta^{PBL} = (Q_C - R)/(\rho c_P) \tag{2.12}$$

The sources of $q$ within the lower troposphere are net condensation $C$ within lower troposphere are and net precipitation rate $P$ .

$$S_{q_l}^{free} + S_{q_l}^{PBL} = C - P \tag{2.13}$$

Here $C = c_p Q_c / L_v$ , $c_p$ is the specific heat capacity, $L_v$ is the latent heat of condensation. Lilly's mixing layer model does not consider horizontal transport in its time derivative, but horizontal transport of dry energy is observed to be important for marine boundary layer cloud amount variations, and so is considered in the dry static energy equation. The conservation of dry energy and total moisture within lower troposphere becomes

$$(\frac{\partial}{\partial t} + \vec{V} \bullet \nabla)\int_0^{Z_T} \rho c_p \theta dz = Q_c - R + \rho c_p \overline{w'\theta'}^0 \tag{2.14}$$

$$\frac{\partial}{\partial t}\int_0^{Z_T} \rho L_v q dz = Q_c - \rho L_v P \tag{2.15}$$

The local total moisture budget is assumed to be in balance.

$$Q_c - L_v P = 0 \tag{2.16}$$

Condensation is balanced by local precipitation rate, which can be approximated as

$$L_v P = \beta F_{LH}^{eff} \tag{2.17}$$

where $\beta$ is the local precipitation coefficient. From previous study, local precipitatio n is determined by how much of surface evaporated water vapor being transported into cloud layer. It depends on the effective surface evaporation $F_{LH}^{eff}$ which is di scussed and parameterized in section 2.3.4.

The time derive of a parcel's dry energy equation is

$$\left(\frac{\partial}{\partial t} + \vec{V} \bullet \nabla\right) \int_0^{z_t} \theta_{pal} dz = S_{\theta_{pal}} \tag{2.18}$$

where $S_{\theta_{pal}}$ is the source of $\theta_{pal}$. Combining equation (2.5), (2.10), (2.14), (2.16) and (2.17), the ADIN budget equation becomes

$$\frac{\partial}{\partial t} ADIN = -\vec{V} \bullet \nabla(\rho c_p \int_0^{Z_T} (\theta - \theta_{pal}) dz) + (\beta F_{LH}^{eff} - R + \rho c_p \overline{w'\theta'}^0) - \rho c_p S_{\theta_{pal}} \tag{2.19}$$

On the right side of the equation, the first two terms are related to horizontal transport, precipitation due to stratiform clouds, and surface heat and moisture flux; they are controlled by slowly varying large scale processes. The last source term for air parcel potential temperature is determined by fast varying convection. Convection is much weaker in MSC regions than that occurring in deep convection regions. The parcel's dry energy change due to ensemble convective process is a key term to balance large scale forcing in QE models, but it is assumed to be small for non-convective MSC cases in this study. In MSC regions, the surface sensible heat flux is very small, local precipitation is determined primarily by local evaporation. The net radiative cooling within the lower troposphere is composed of both clear sky radiative cooling $R_{clr}$ and cloud radiative cooling $R_{crf}$.

$$R = R_{clr} + R_{crf} \tag{2.20}$$

The local change of ADIN now becomes

$$\frac{\partial}{\partial t} ADIN = -\vec{V} \bullet \nabla (c_p \int_0^{Z_T} (\theta - \theta_{pal}) dz) + (\beta F_{LH}^{eff} - R_{clr} - R_{crf}) \tag{2.21}$$

Clear sky radiative cooling below 800hPa is assumed to be proportional to clear sky radiative cooling below 680hPa, which balances part of the total dynamical transport of available dry inhibition energy.

$$R_{clr} = -\alpha \vec{V} \bullet \nabla A_{dyn}(ADIN) + c \tag{2.22}$$

Here $\alpha$ is a constant value between 0 and 1, $c$ is an empirical constant. Combing the equations (5.21) and (5.22), we get

$$\frac{\partial}{\partial t} ADIN = -(1-\alpha)\vec{V} \bullet \nabla (ADIN) + \beta F_{LH}^{eff} - R_{crf} - c \tag{2.23}$$

The dynamical transport term in the right side of equation (2.23) includes horizontal transport and vertical transport terms. In a typical stratocumulus topped boundary layer, the potential temperature is well-mixed close to the ocean surface, and the subsidence rate in the free atmosphere is relatively unchanged from the trade wind inversion down to boundary layer top, The resulting vertical transport term is determined by the mean vertical velocity of free air $\overline{w}^{free}$ which is assumed to be proportional to vertical velocity at 850hpa $w_{850}$ and the lower troposphere stability $\Delta\theta_{700} = \theta_{700} - T_s$.

$$\int_0^{Z_{800}} \rho c_p w (\frac{\partial \theta}{\partial z})_{env} dz = \rho c_p \overline{w}^{free} \Delta\theta_{700} \approx \rho c_p w_{850} \Delta\theta_{700} \tag{2.24}$$

Here $a_0$ is an empirical coefficient. The horizontal transport of ADIN is determined by the horizontal transport of environmental dry energy and air parcel dry energy, the later is

typically determined by subcloud dry energy at around 1000 hpa. The resulting total dynamical transportation is now in the form of

$$-\vec{V} \bullet \nabla(ADIN) \approx - \rho c_p w_{850} \Delta\theta_{700} - \int_0^{Z_{800}} \rho c_p \vec{v}_H \cdot \nabla_H (\theta_{env} - \theta_{scl}) dz \quad (2.25)$$

We define $S$ as the changing rate of Available Dry Inhibition Energy (ADIN).

$$S = \frac{\partial}{\partial t} ADIN \quad (2.26)$$

Combining the equations (2.23), (2.24), and (2.25), we get

$$S = (1-\alpha) \ (- \rho c_p w_{850} \Delta\theta_{700} - \int_0^{Z_{800}} \rho c_p \vec{v}_H \cdot \nabla_H (\theta_{env} - \theta_{scl}) dz) + \beta F_{LH}^{eff} - R_{crf} - c \quad (2.27)$$

### 2.3.2 E-folding time for $S$

Using 6hr ERA-40 reanalysis data and ISCCP FD SST 3hr data, there is a linear relationship between $S$ and its local change rate as shown in Figure 2.3.

$$\frac{\partial S}{\partial t} = -\frac{S}{T_{efold}} \quad (2.28)$$

The analytic solution of $S$ is

$$S(t) = S_0 e^{-t/T_{efold}} \quad (2.29)$$

When $t >> T_{efold}$, we get $S(t) = 0$ .Fig.2.3 shows that the e-folding time $T_{efold}$ is approximately 6 to 7 hours for subtropical MSC regions. For timescales on daily, monthly and seasonal time scales, the local change of ADIN is zero.

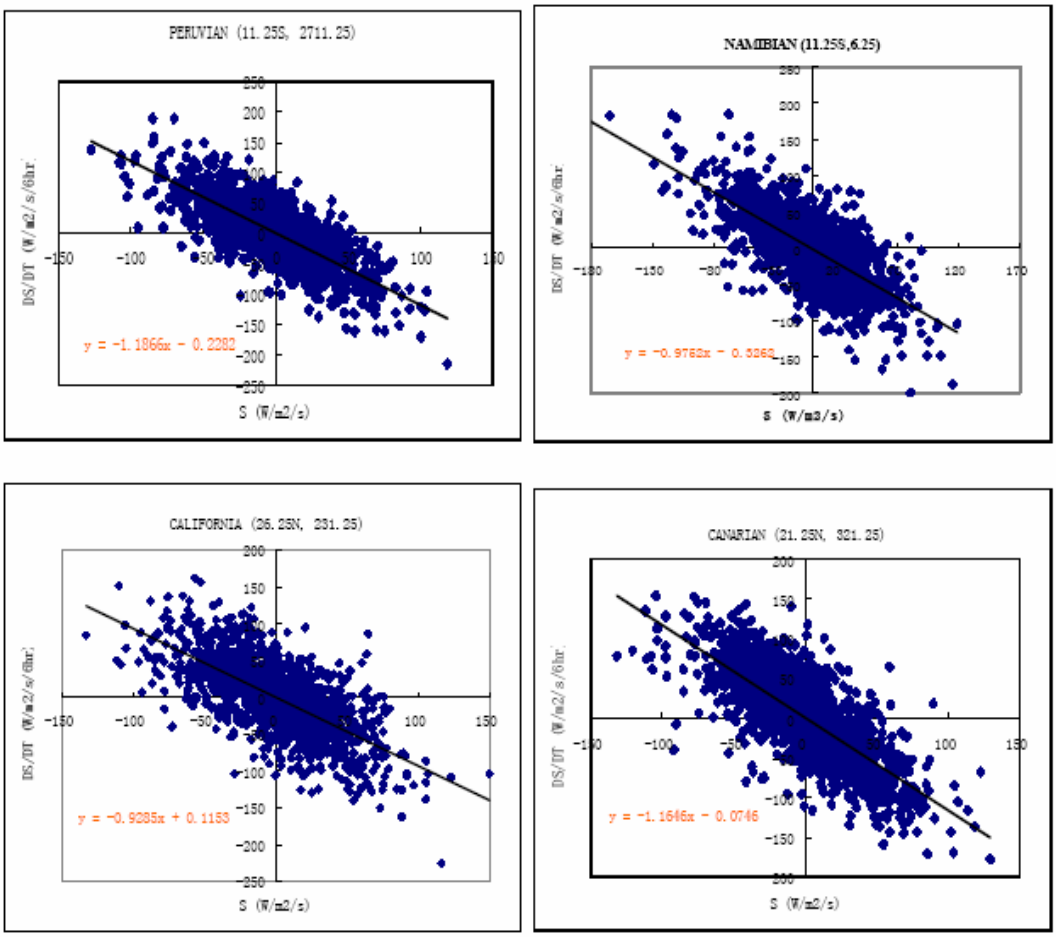


**Figure 2.3** $\partial_t S$ verse $S$ based on area-averaged 6-hour ERA40 reanalysis data in four MSC regions in 1985.

### 2.3.3. Cloud Radiative Forcing within the Lower Troposphere

The cloud top radiative cooling is determined by the dynamical transport heating and the surface latent heat flux.

$$R_{crf} = -(1-\alpha)\left(aw_{850}\,\Delta\theta_{700} + \int_0^{Z_{800}} c_p \vec{v}_h \cdot \nabla_h \left(\theta_{env} - \theta_{scl}\right) dz\right) + Q_c \qquad (2.30)$$

The atmospheric cloud top radiative cooling is defined as the difference between full sky radiative cooling and the clear sky radiative cooling within the atmosphere. ISCCP FD

data has full sky and clear sky radiative flux at surface and at 680hPa. Because the boundary layer cloud is observed to be suppressed below the trade wind inversion, little low cloud occurs above 800hPa. As a result, cloud top radiative cooling below 800hPa is almost the same as cloud top radiative cooling below 680hPa.

$$R_{crf}^{b800} \approx R_{crf}^{b680} = R_{full}^{b680} - R_{clr}^{b680} \tag{2.31}$$

where $R_{crf}^{b800}$ and $R_{crf}^{b680}$ are respectively the cloud radiative cooling from surface to 800hPa and 680hPa; $R_{full}^{b680}$ and $R_{clear}^{b680}$ are respectively the ISCCP FD full sky and clear sky radiative cooling in the air column from surface to 680hPa. ISCCP FD has three-hour global radiative vertical profile data at $2.5^{\circ} \times 2.5^{\circ}$ spatial resolutions which is used to calculate the atmospheric cloud radiative forcing in the subtropics. Figure 2.4 suggests a linear relationship between monthly ISCCP low cloud cover and ISCCP FD monthly cloud radiative forcing within the lower troposphere in all four subtropical MSC regions. As a result, the atmospheric cloud radiative forcing can be described as a function of low cloud cover $A_c$.

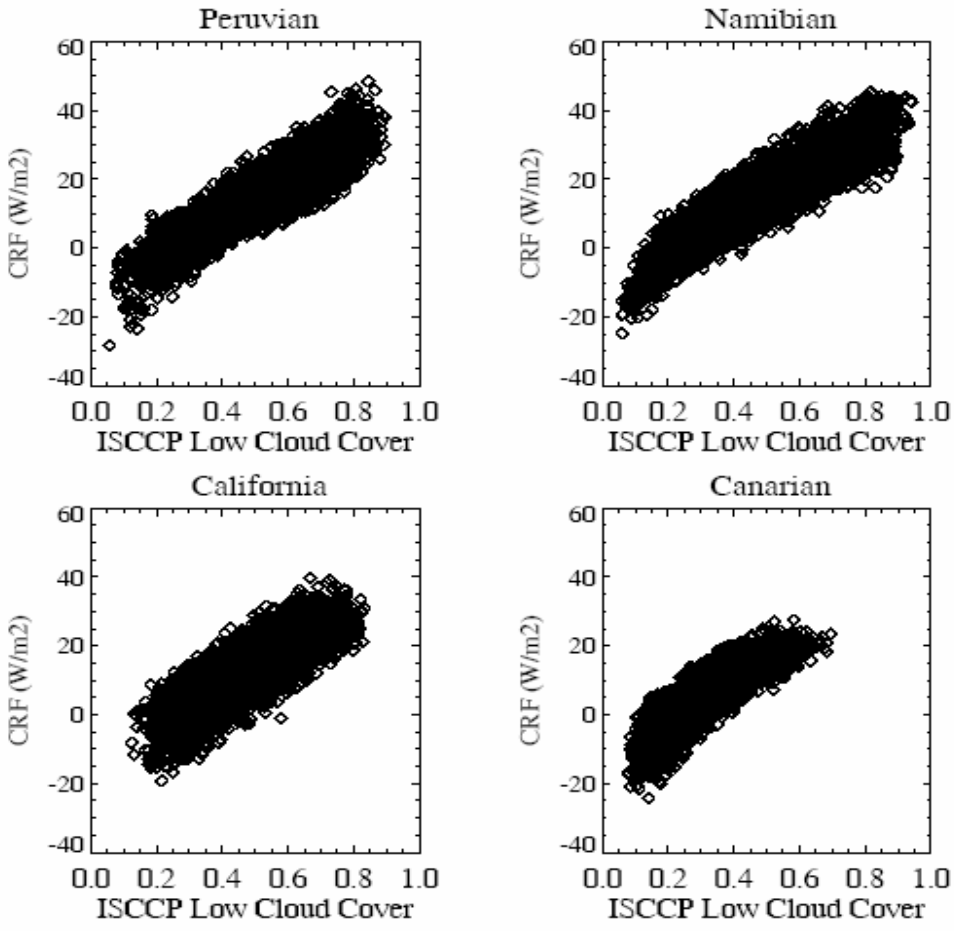


**Figure 2.4** ISCCP-FD monthly cloud radiative forcing (W $m^{-2}$) within the lower troposphere verses the ISCCP monthly low cloud cover in four subtropical MSC regions during the period from 1985 to 1997.

$$R_{crf} = R^0_{crf} A_c - R_0, \text{ when } A_c \geq 0.05 \quad (2.32)$$

The unit area cloud radiative forcing within the lower troposphere $R^0_{crf}$ is approximately 70 W m$^{-2}$ and $R_0$ is approximately 20 W m$^{-2}$. From Fig.2.4, the grid averaged low cloud fraction at $2.5^\circ$ x $2.5^\circ$ horizontal resolution is seldom less than 5%. When $A_c = R_0 / R^0_{crf} \approx 0.285$, the net cloud radiative cooling is zero because solar heating is balanced by longwave radiative cooling within cloud. From observations, shallow cumulus cloud has small cloud fraction between 10% to 25%, its cloud radiative cooling is negative because shallow cumulus cloud absorbs more solar heating than its longwave emission. The empirical relationship between cloud fraction and cloud top radiative cooling is not applicable to the nearly clear sky case when the grid averaged low cloud fraction is less than 5%, which is seldom observed in the marine stratus and stratocumulus regions. Seasonal variation of cloud radiative forcing produces the seasonal variation of low cloud cover in subtropical regions.

A simple cloud cover formula can be derived by combining (2.30) and (2.32).

$$A_c = [-(1-\alpha)(\rho c_p w_{850} \Delta\theta_{700} - \int_0^{800mb} \rho c_p \vec{v}_h \cdot \nabla_h (\theta_{env} - \theta_{scl}) dz) + \beta F^{eff}_{LH} + R_0 + c] / R^0_{crf} \quad (2.33)$$

The first term on the right represents the effect of large scale subsidence, the second term represents the horizontal transport of ADIN; and the third term represents the surface evaporation contribution. The large scale subsidence is controlled by the slowly varying annual cycle of solar heating and rapid variations due to waves and turbulence. In order to capture the seasonal variations of low cloud amount, the six hour ERA-40 large scale subsidence is smoothed by a 30-day average in the offline experiments. In the following section, we parameterize the surface latent heat flux by relating it to the lower

tropospheric stability. This is plausible because the surface latent heat flux is determined by ocean surface temperature, near surface relative humidity, and surface wind speed. The stability of the lower troposphere is a good indicator for ocean surface temperature, and it controls the ocean surface wind and near surface relative humidity. We use both ERA-40 and NCAR NCEP reanalysis data to parameterize the surface latent heat flux. Any current reanalysis data has uncertainties in ocean surface wind, surface latent heat flux, and near surface humidity, but if a relationship between two variables is supported by two independent datasets, we can have more confidence in it.

### 2.3.4 Surface Evaporation and Convective Heating: Empirical Parameterizations

Surface flux plays important roles in boundary layer formations and air-sea interaction. It is well known that surface latent heat flux is determined primarily by ocean surface wind speed and near surface relative humidity. In the marine stratus and stratocumulus regions, analysis with a mixed layer model have suggested that surface fluxes depend significantly on entrainment, which is sensitive to the local thermal structure such as the strength of cloud top inversion (Stevens 2002). The lower tropospheric stability represents the difference between tropical ocean SST and the subtropical ocean SST, which determines the ocean surface pressure gradient anomaly and surface wind speed. Here we re-formulate the surface latent heat flux based on lower tropospheric stability and sea surface temperature.

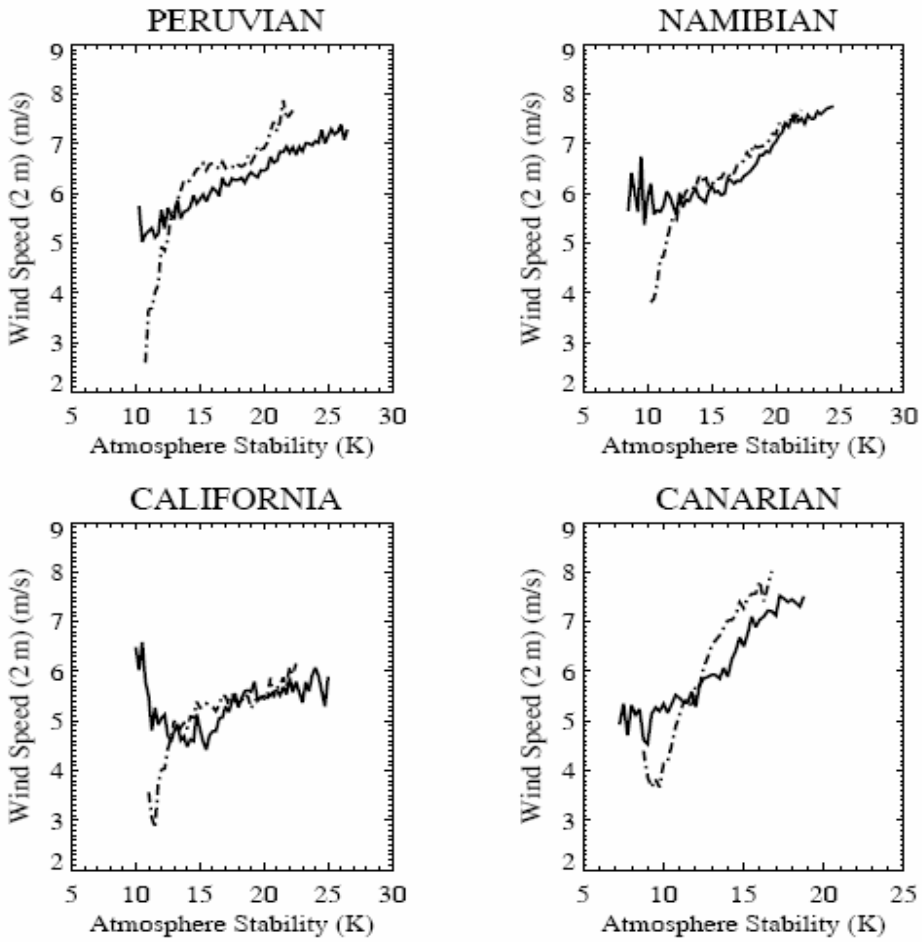


**Figure 2.5** Monthly surface wind speed (m $s^{-1}$) at 2 m as a function of area-averaged monthly atmospheric stability (0.25 K bin width) using daily ERA-40 reanalysis data (solid line) and monthly NCEP-NCAR reanalysis data (dot-dashed line) in four Subtropical MSC regions during the period from 1985 to 1997.

We use a bulk parameterization for the surface latent heat flux:

$$F_{LH} = L_c \rho_a \overline{w'q'}^0 = L_c \rho_a C_E \overline{U}_a (q_s - q_a) = L_c \rho_a C_E \overline{U}_a q_s (1 - RH) \qquad (2.34)$$

The surface latent heat flux is evidently determined by the air density $\rho_a$ , the turbulence coefficient $C_E$ , surface wind speed $\overline{U}_a$ , and the near surface humidity difference $q_s - q_a$.

Monthly surface wind speed at 2 m is plotted in Figure 2.5 as a function of monthly atmospheric stability using daily ERA-40 reanalysis data (solid line) and monthly NCEP-NCAR reanalysis data (dot-dashed line) in four Subtropical MSC regions during the period from 1985 to 2000. A nearly linear relationship between the surface wind speed and the atmospheric stability is suggested by both the ERA-40 and NCEP-NCAR reanalysis in the four subtropical MSC regions. The surface wind speed increases by approximately 0.15 m $s^{-1}$ for every 1 K increase of atmospheric stability.

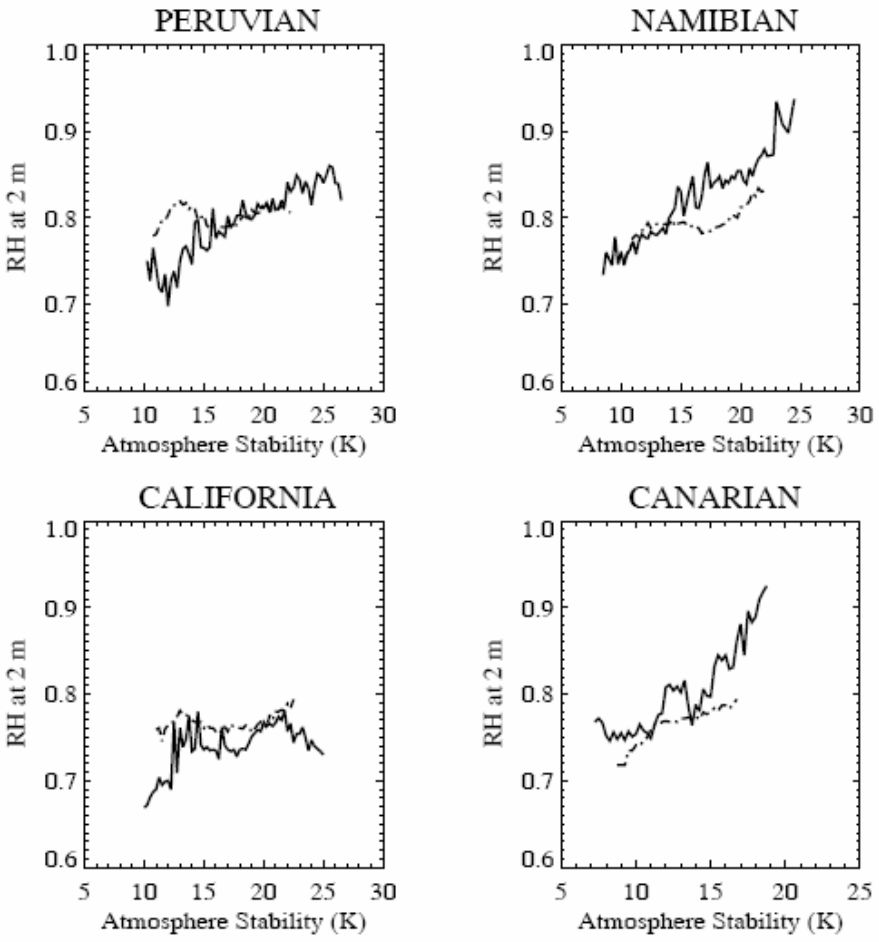


**Figure 2.6** As in Figure 2.5 but for monthly surface relative humidity at 2 m.

The surface humidity difference is determined by ocean surface temperature and near surface relative humidity, which is defined as $RH = q_a / q_s$. The symbols $q_a$ and $q_s$ represent the air temperature at 2 m and the saturated specific humidity of sea surface temperature respectively. The near surface relative humidity is calculated here using ERA-40 daily dew point temperature at 2m and $q_s$. Monthly mean near surface RH is plotted in Figure2.6 as a function of monthly atmospheric stability in 0.25 K bin width using the daily ERA-40 reanalysis data (solid line) and monthly NCEP-NCAR reanalysis data (dot-dashed line) in four Subtropical MSC regions during the period from1985 to 2000. ERA-40 RH is calculated using the ERA-40 2 m dew point temperature at 2 m and SSTs from the ISCCP FD data. The NCEP-NCAR RH is calculated using the NCEP specific humidity at 2 m and NCEP skin temperature.

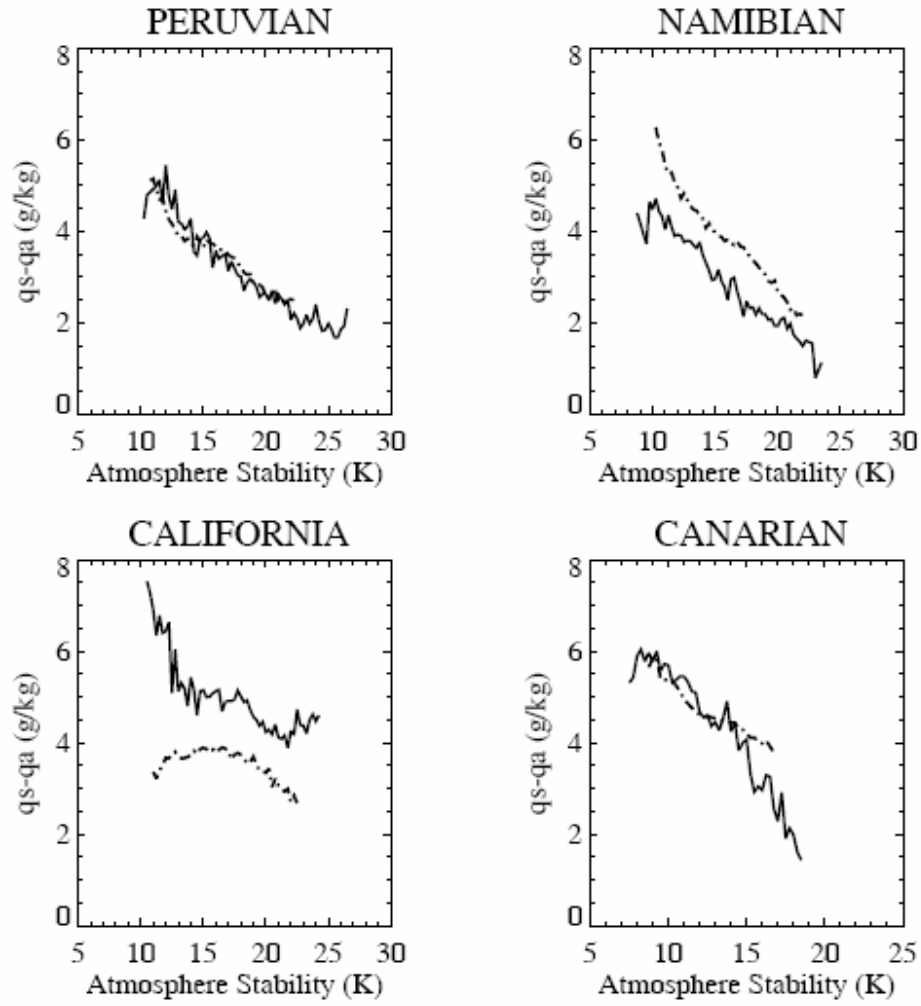


**Figure 2.7** As in Figure 2.5 but for monthly specific humidity difference (g $(kg)^{-1}$) at 2 m.

Figure 2.6 illustrates a strong linear relationship between the near surface relative humidity and lower troposphere stability.

$$RH = RH_0 + a_{RH}\Delta\theta \tag{2.35}$$

From Figure 2.6, there is approximately 2% increase in the near surface relative humidity for every 1 K increase in lower troposphere stability. Stronger stability isolates the warm and dry free air from mixing into the boundary layer, and it also enhances the moisture transport from the surface, hence raising the near surface relative humidity. The resulting specific humidity difference $q_s - q_a$ is negatively correlated with lower troposphere stability in the subtropical ocean as shown in Figure 2.6.

This negative relationship can be simplified using equation as follows:

$$q_s - q_a = q_s(1-RH) = q_s(1-RH_0 - a_{RH}\Delta\theta) = \Delta q_0\left(1-\frac{\Delta\theta}{\Delta\theta_{\max}}\right) \tag{2.36}$$

$$\Delta\theta_{\max} = (1-RH_0)/a_{RH} \tag{2.37}$$

In equation (2.36) and (2.37), $\Delta q_0 = q_s(1-RH_0)$ and $\Delta\theta_{\max}$ is called the maximum stability capacity. When the lower troposphere stability exceeds $\Delta\theta_{\max}$, according to this expression the atmosphere can no longer gain the moisture from the ocean surface. In each subtropical MSC region, ocean surface is cold, $\Delta q_0$ is assumed to be constant. Figure 2.27 shows a nearly linear relationship between $q_s - q_a$ and $\Delta\theta$ in each region. However, the negative slope between $q_s - q_a$ and $\Delta\theta$ is larger near the Peruvian and Namibian regions where SST is colder than California and Canarian regions, which suggests that a unified parameterization of humidity difference $q_s - q_a$ for all MSC

regions should be based on both lower troposphere stability and ocean surface SST. In summary, the surface evaporation is expressed as

$$F_{LH} = d\ \Delta\theta\left(1-\frac{\Delta\theta}{\Delta\theta_{\max}}\right)+\ e \qquad (2.38)$$

where $d$ and $e$ are statistical coefficients, using least square fitting with ERA-40 surface latent heat flux, we get $d = 15\ W/m^2/K$ and $e = 20\ W/m^2$. Based on ERA-40 reanalysis, the maximum stability capacity $\Delta\theta_{\max}$ is approximately 30 K. Figure 2.8 is the relationship found between surface latent heat flux and the lower tropospheric stability using monthly data from ERA-40 reanalysis, NCEP NCAR reanalysis, and empirical parameterization shown in equation (2.38) during the period from1985 to 1989 in four subtropical MSC regions. In a low stability regime, when the atmospheric stability increases, the surface wind speed increases, providing a larger surface latent heat flux. However, when the stability is greater than a critical value, increasing the atmospheric stability leads to a higher near surface relative humidity, hence a smaller surface latent heat flux.

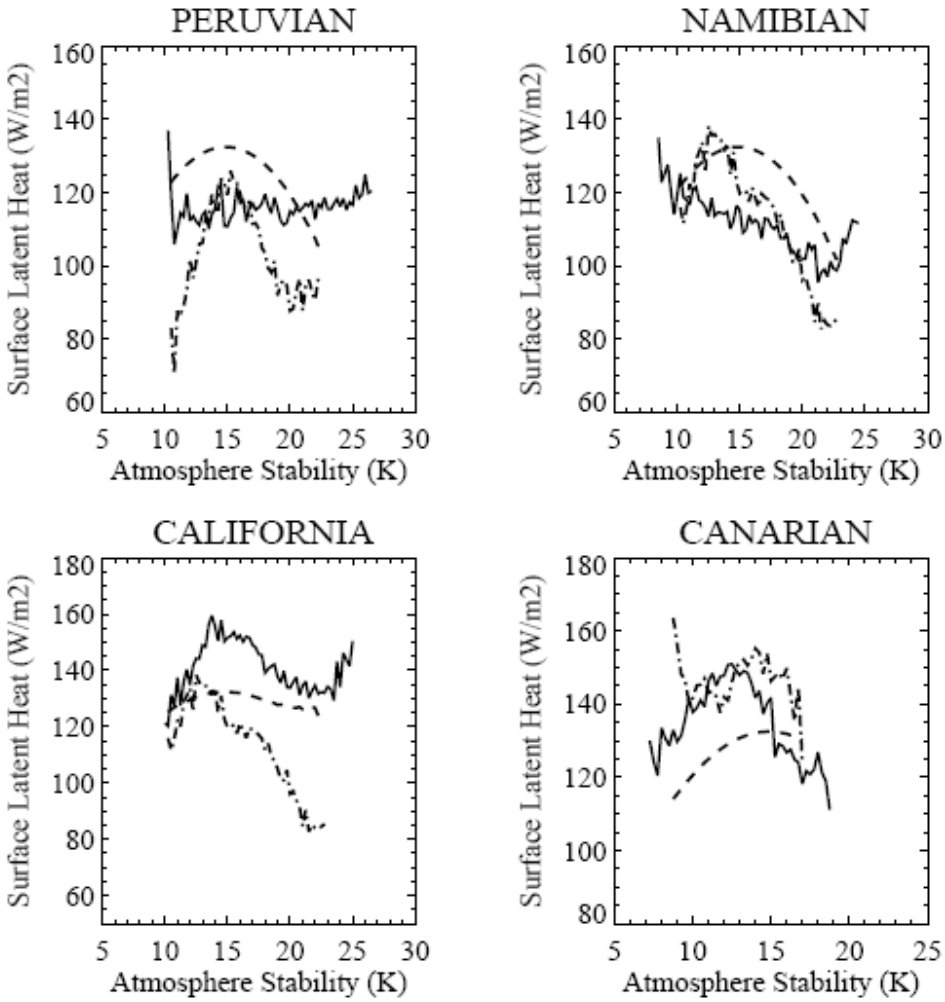


**Figure 2.8** Monthly surface evaporation (W $m^{-2}$) as a function of area-averaged monthly atmospheric stability (0.25 K bin width) using monthly ERA-40 reanalysis data (solid line) and monthly NCEP-NCAR reanalysis data (dot-dashed line), and empirical parameterization in equation 2.37 (thin dashed line) in four Subtropical MSC regions during the period from 1985 to 1997.

As shown in the equation (2.16), the convective heating is balanced by local precipitation rate, which is determined by local precipitation coefficient and effective surface evaporation. Convective heating released from cloud water condensation not only depends on how much water vapor transported from surface but also depends on the ratio of water vapor changed to cloud liquid water. The former depends on surface latent heat flux, and the later is assumed to be dependent on the effective maximum stability capacity $\Delta\theta_{eff}$. From equation (2.37), the maximum stability capacity $\Delta\theta_{\max}$ is a function of the constant $RH_0$. From previous marine cloud transition study (Bretherton et al. 1997), when ocean surface becomes warmer, cloud layer tends to be decoupled with ocean surface mixing layer, the water vapor transported from near surface to cloud layer is significantly decreased. Therefore it is reasonable to assume that $\Delta\theta_{eff}$ depends on the effective relative humidity $RH_{eff}$ which is parameterized as an empirical function of SST such that when ocean surface is warmer, the effective near relative humidity is higher, less surface evaporated water vapor is transported into cloud layer due to increased decoupling between surface mixing layer and cloud layer.

$$\Delta\theta_{eff} = (1 - RH_{eff}) / a_{RH} = 50(1 - q_s(T_s) / q_s^0) \tag{2.39}$$

Here $q_s^0$ is given a constant value such that when $\Delta\theta_{eff}(20^0 c) = 30\text{K}$. The convective heating is then formulated as the empirical functions of lower troposphere stability and ocean surface SST.

$$Q_c = \beta F_{LH}^{eff} = \beta\left( d\Delta\theta(1 - \frac{\Delta\theta}{\Delta\theta_{eff}(T_s)}) + e \right) \tag{2.40}$$

*2.3.5 Diagnostic low cloud cover equation and ADIN annual budget*

The unified cloud cover formula for all subtropical MSC regions is obtained by combining equation (2.33) and (2.39). We get the necessary coefficients which best fit the EERCA monthly low cloud amount ($\alpha = 0.7$, $\beta = 0.16$, $c = 66$).

$$A_c = -4.3 w_{850} \Delta\theta - 4.3 \int_0^{z_{800}} \vec{v} \cdot \nabla(\theta_{env} - \theta_{scl}) dz + 0.034 \Delta\theta \left(1 - \frac{\Delta\theta}{\Delta\theta_{eff}(T_s)}\right) + 0.103 \quad (2.40)$$

Calculated ADIN energy budget in four MSC regions for annual mean, DJF, and JJA from ERA-40 reanalysis and ISCCP FD radiation data are listed in Table 2.3.

**Table 2.3 Monthly averaged lower tropospheric dry static energy local change [ $\frac{\partial}{\partial t} \int_0^{z_{800}} c_p(\theta_{env} - \theta_{pal}) dz$ ], vertical transport $-0.3 c_p w_{850} \Delta\theta$, horizontal transport [ $-4.3 \int_0^{z_{800}} \vec{v} \cdot \nabla(\theta_{env} - \theta_{scl}) dz$ ], convective heating [ $Q_c = \beta (15 \Delta\theta \left(1 - \frac{\Delta\theta}{\Delta\theta_{eff}(T_s)}\right) + 20)$ ], and cloud radiative cooling $R_{crf}$ (positive means heating) during 1985 to 1997.**

| | $\frac{\partial}{\partial t} \int_0^{z_{800}} c_p(\theta_{env} - \theta_{pal}) dz$ | Vertical Transport | Horizontal Transport | Convective Heating | $R_{crf}$ |
|---|---|---|---|---|---|
| Peruvian | -0.01 | 19.6 | 3.0 | 16.8 | -25.0 |
| Namibian | -0.04 | 17.0 | 7.2 | 16.9 | -29.2 |
| California | -0.03 | 16.8 | 3.42 | 18.9 | -18.0 |
| Canarian | -0.005 | 9.9 | 1.8 | 16.4 | -11.4 |

## 2.4 Monthly Low Cloud Amounts from EERCA, ISCCP, and New Scheme Simulation Results

EECRA provides individual COADS ship data reports during the period from 1985 to 1997; ISCCP D1 and ISCCP FD data have 2.5°x 2.5°grid-averaged cloud data and ocean skin temperature for every 3 hours during the period from 1985 to 1997; the ERA-40 reanalysis has 2.5°x 2.5° grid-averaged wind and temperature at difference levels for every six hours during the period from 1985 to 1997. In order to compare the monthly mean low cloud amount among EECRA ship data, ISCCP D-series data, and the calculated cloud amount using the KH scheme and the new scheme, we use the following procedure. First, we map ISCCP D-series low cloud amounts, lower troposphere stability, large-scale subsidence, and calculated horizontal transported dry static energy onto each individual ship record. The lower troposphere stability is calculated using ISCCP FD 3-hour SST and ERA-40 6-hour temperature at 700mb; the large scale subsidence is from 6-hour ERA-40 data, the subsidence data is smoothed by 30-day averaged to remove the high frequency part; the dynamical transport is calculated using ERA-40 reanalysis data. First for each individual ship record, we also get the ISCCP D-series cloud amount and the calculated low cloud amount using the KH scheme and the new scheme. Then, we calculate the grid value of low cloud amount at 2.5°x 2.5° horizontal resolution then do monthly average. Because the day/night sample bias is reported in EECRA NDP-026C documentation (Hahn and Warren, online), to get monthly-averaged value, we first calculate the monthly averaged day-time value and night-time value separately; then get the mean value by adding monthly day-time value with night-time value then dividing it by two.

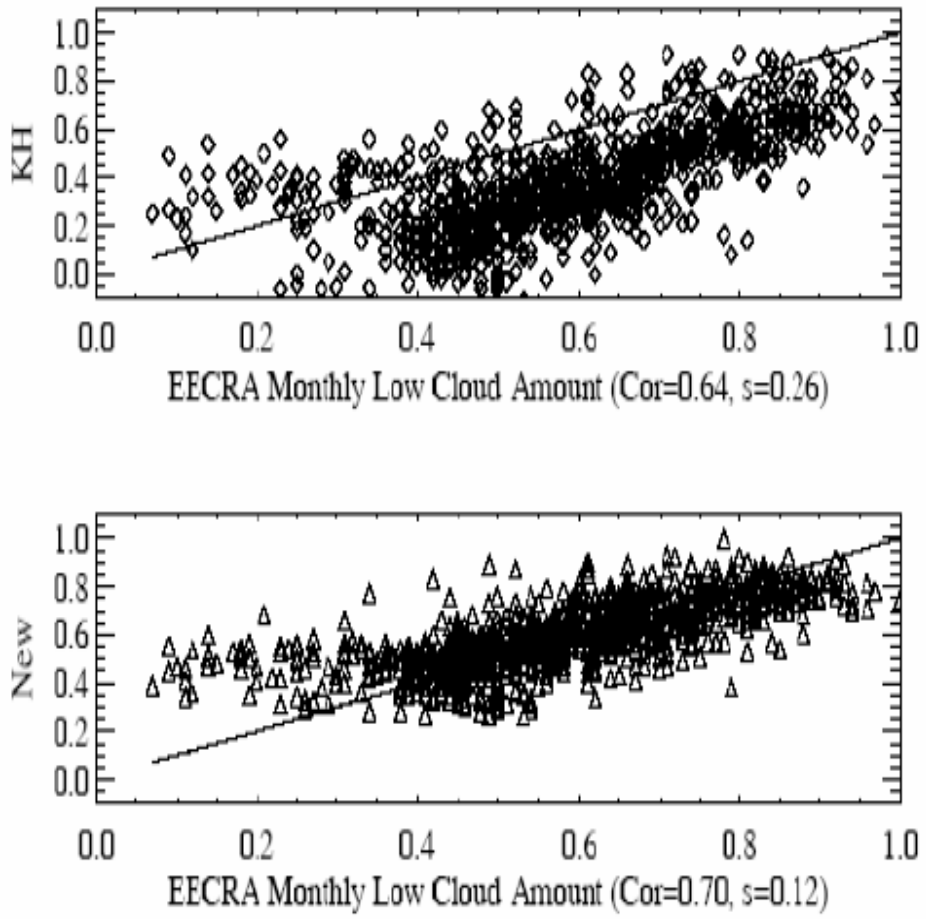


**Figure 2.9** Area-average monthly low cloud amount simulated using the KH scheme (upper panel) and the new scheme (lower panel) plotted against EECRA observed low cloud amount during the period from 1985 to1997.

Figure 2.9 is the scattering plot between the EECRA monthly low cloud amount and the KH scheme calculated cloud amount (upper panel), the new scheme calculated low cloud amount (middle panel), and the ISCCP D-series low cloud amount (bottom panel) in the four regions during the period of 1985 to 1997. The new scheme has higher correlation of 0.7 with the EECRA monthly low cloud amount, while the KH scheme has correlation of 0.64. Figure 2.9 is the scattering plot between ISCCP D-series monthly low cloud amount and KH scheme results (upper panel), the new scheme results (middle panel), and the EECRA ship data (lower panel). The new scheme also has higher correlations of 0.75 with ISCCP monthly low cloud amount; while KH scheme has a slightly low correlation of 0.72. The correlation between ISCCP D-series monthly value and EECRA monthly value is 0.77, and ISCCP D-series systematically underestimates the EERCA low cloud amount by a few percent.

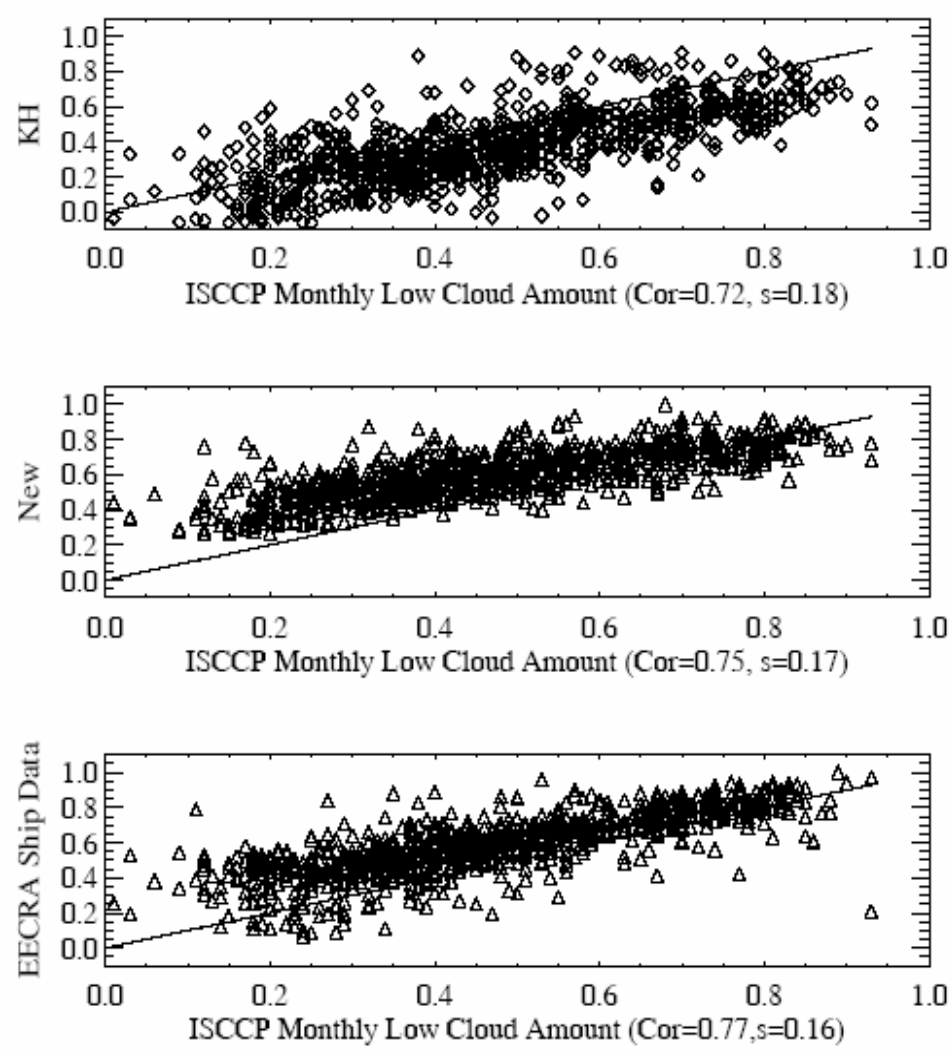


**Figure 2.10** The scattering plot between ISCCP D-series low cloud amount and the KH scheme results (upper panel), the new scheme results (middle panel), and EECRA ship data (lower panel) during the period from 1985 to1997.

## 2.5 Conclusions

A conceptual model is developed to link boundary layer clouds with large scale circulation and local thermal structures. The model is based on a modified concept named Lower Troposphere Available Dry Inhibition Energy (ADIN). The e-folding time for the local change of ADIN is found to be approximately 6 to 7 hours. In monthly and longer timescales, Local productions of ADIN are balanced by local destructions of ADIN within lower troposphere. Dynamical transport of environmental dry static energy and surface evaporation lead to the variations of cloud top radiative cooling, which is a linear function of low cloud cover. The convective heating is parameterized based on tropospheric stability and ocean surface SST. The variation of boundary layer cloudiness is formulated by a unified equation connected low cloud cover with lower tropospheric stability, large scale subsidence, and dynamical transport of ADIN below trade wind inversion. The new scheme simulated low cloud cover variation is better correlated with monthly EECRA ship data and ISCCP D-series low cloud amount than that of the Klein-Hartmann scheme.

# CHAPTER 3

# A SIMPLE LOW CLOUD COVER SCHEME BASED on LOWER TROPOSPHERIC STABILITY AND AVAILABLE DRY INHIBITION ENERGY TRANSPORT IN THE SUBTROPICAL MSC REGIONS Part II: SEASONAL and INTELANNUAL SIMULATIONS

## 3.1 Offline Simulation Results

### 3.1.1 Seasonal Variations of Low Cloud Amounts, Dynamical Transported Heating, and Convective Heating

The seasonal variations of low cloud amount have been linked to the various meteorological variables. Klein and Hartmann (1993) found a good linear relationship between the seasonal cycle of low stratiform cloud and lower tropospheric stability. Norris (1998) study the geographical and seasonal variations of different types of low cloud over the oceans, and found that the transition from MSC to cumulus occur progressively equator-ward over eastern subtropical oceans, and that the advection over colder SST on the southern side of an equatorial cold tongue sometimes produce less cloudiness. The relationship between low cloud anomaly and the ocean surface horizontal temperature advection was recently studied in Mansbach and Norris (2006). In this study, low cloud variations are determined by the seasonal variations of convective heating and dynamical transport of dry static energy between environment and air parcel.

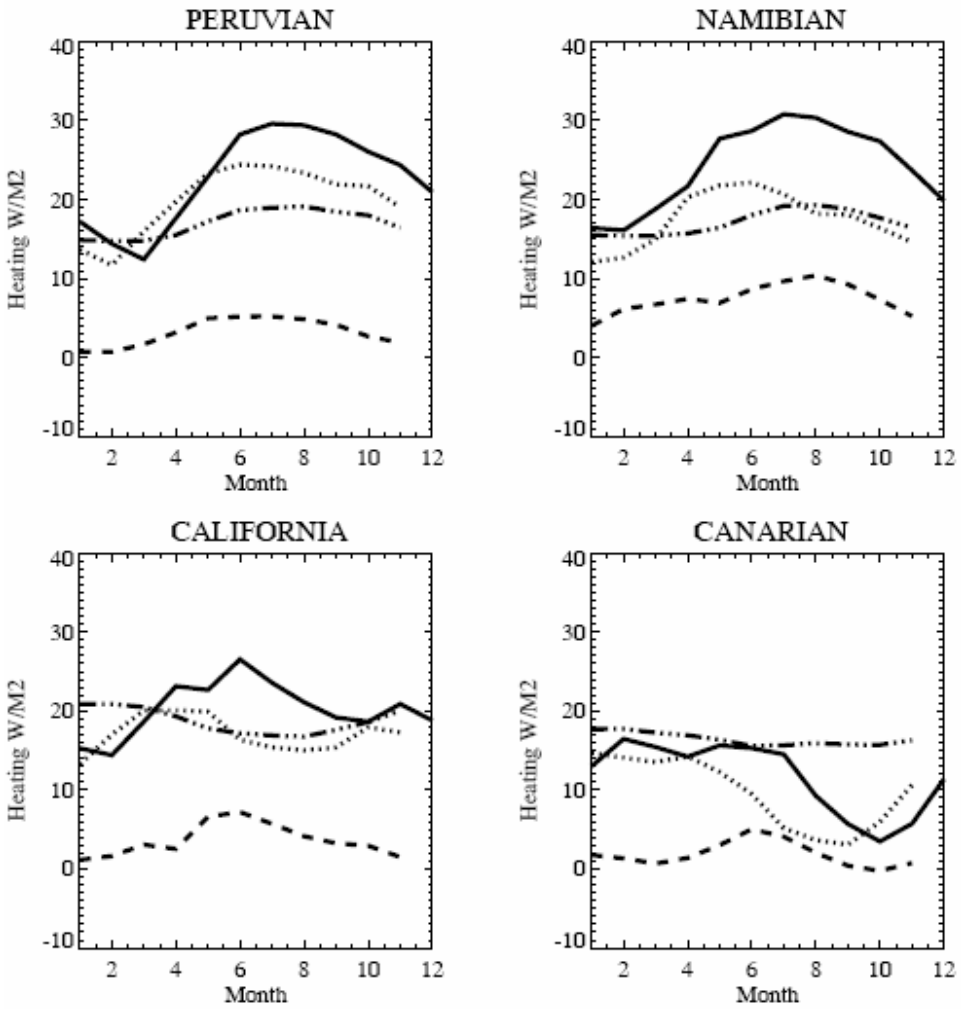


**Figure 3.1** Seasonal variations of area-averaged ADIN budget terms (W $m^{-2}$) in four MSC regions during the period from 1985 to1997. The solid line is the total dynamical transported heating, the thin dashed line is the vertical transported heating, the thick dashed line is the horizontal transported heating, and the dashed-three-dot line is the convective heating.

As shown in Figure 3.1, convective heating has small seasonal variations; the total dynamical transported heating has a much larger seasonal cycle and determines the low cloud variations. The vertically transport heating typically has a peak in late spring; while the horizontally transport heating reaches its peak in late summer. The resulting total transport heating peaks at boreal summer near the Peruvian, Namibian, and Californian regions. Low cloud amount from EERCA, the KH scheme, and the new scheme is shown in Figure3.2. The observed low cloud variations from EECRA data have the same seasonal pattern as that of total dynamical transported heating shown in Figure 3.1. The new scheme realistically simulates low cloud seasonal variations in all MSC regions. Compared with the new scheme, KH scheme underestimates the low cloud amount by 20% in the Namibian, 15% in the Peruvian, and 10% in the Californian and Canarian regions during the season of JJA.

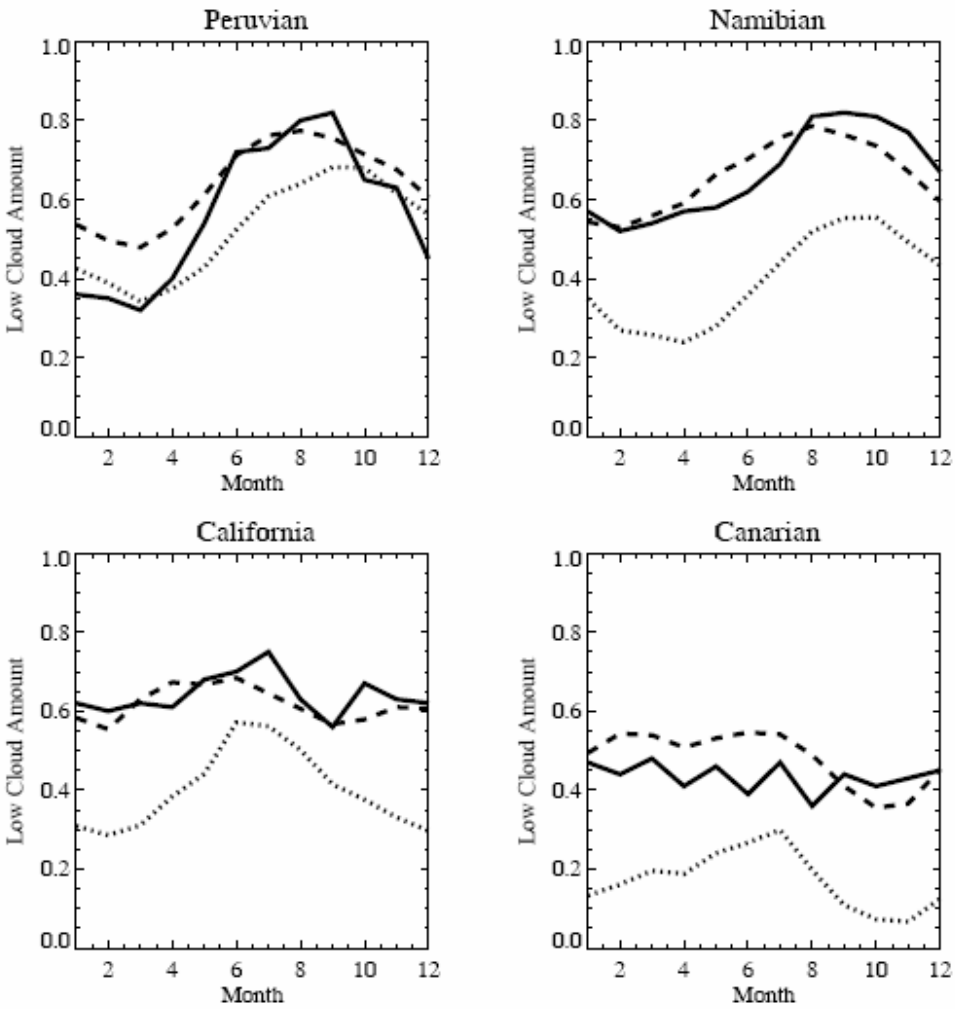


**Figure 3.2** Seasonal cycles of area-averaged monthly mean low cloud cover from EECRA ship observation (solid line), the new scheme results (thick dashed line), and the KH scheme results (thin dashed line) during the period from 1985 to 1997.

### 3.1.2. Monthly Low Cloud Amount Variations from 1985 to 1997

Klein, Hartmann, and Norris (1994) used the long-term record of observations from OWSN to study the inter-annual variations of low cloud amount and its relationship with various meteorological variables in the summer Northeast Pacific. Their study suggests that the Lagrangian histories of boundary layer air parcels must be considered for an accurate prediction of boundary layer cloudiness; and that the variations in atmospheric circulation associated with the surface wind patterns may play an important role in adjusting both the boundary layer cloudiness and the SST. Since Eulerian coordinates are widely used in most state-of-art GCMs, it is difficult to represent the Lagrangian history of a boundary layer cloud in them. Instead of calculating the Lagrangian history of a parcel, our conceptual model focuses on local energy balance to keep local ADIN unchanged. Low cloud amount variations are proportional to cloud top radiative cooling variations, which are determined by convective heating and dynamical transport of the dry static energy difference between environment and parcels. Using ERA-40 reanalysis and ISCCP FD SST as input, we simulate the monthly area-averaged low cloud amount during the period of 1985 to 1997 and compare it with the observed ISCCP D1 monthly low cloud amount as shown in Figure3.3. Compared with the KH scheme, the new scheme significantly improves the simulation performances near the Peruvian and Canarian regions. The new scheme explains 25% more total monthly covariance near the Peruvian and 22% more covariance near the Canarian region than that from the KH scheme in both regions.

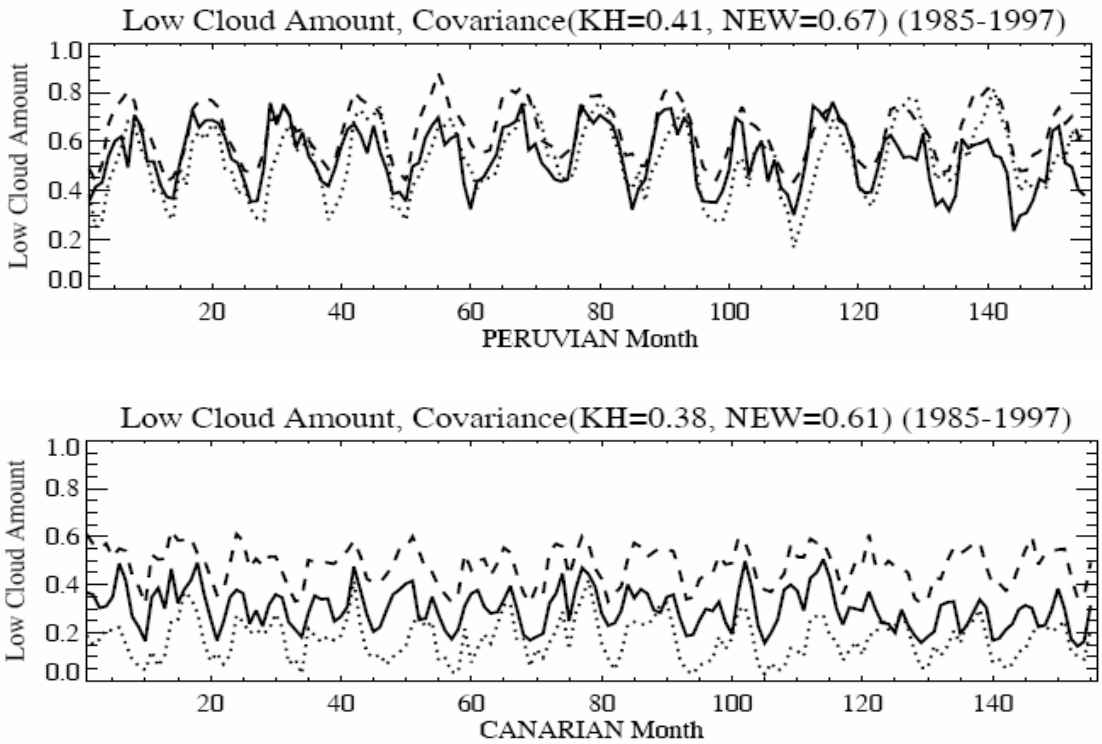


**Figure 3.3** Area-averaged monthly low cloud amounts during the period from 1985 to 1997 from the ISCCP D-series (SOLID), the new scheme results (thick dashed), and the KH scheme results (thin dashed) in the Peruvian and Namibian regions.

Table 3.1 calculates the explanatory covariance of each term in the new scheme for inter-annual variations of monthly ISCCP D-series data. The value “Zero” in Table 3.1 represents a correlation coefficient that does not pass the significance t-test.The vertical transport of ADIN is the most important term in explaining low cloud inter-annual variations near the Peruvian region; Convective heating associated with ocean surface SST anomalies is most important in both the Namibian and California regions; ocean surface cold temperature advection is most important in explaining inter-annual variations of low cloud in the Canarian region. Generally speaking, the inter-annual variation of low cloud amount is mostly determined by ocean surface SST anomalies,

which lead to near surface cold advection variations and convective heating variations in most MSC regions.

**Table 3.1** Covariance between area-averaged observed ISCCP low cloud amount and vertical transport, near surface advection, horizontal transport of environmental dry energy, and KH and new scheme simulated low cloud amount during 1985 to 1997.

| Covariance | Vertical transport | Surface transport | Envi. advection | Convective heating | KH Scheme | NEW scheme |
|---|---|---|---|---|---|---|
| Peruvian | 52% | 36% | Zero | 49% | 41% | **66%** |
| Namibian | 23% | 16% | 25% | **74%** | 72% | 66% |
| California | 12% | 18% | Zero | 22% | **56%** | 16% |
| Canarian | 24% | 46% | Zero | 5.3% | 37% | **59%** |

### 3.1.3 Global ENSO index and ISCCP Low Cloud Amount Variations

The Global SST ENSO index is defined as the average SST anomaly equatorward of 20-degrees latitude (north and south) minus the average SST poleward of 20-degrees, Anomalies are with respect to the period from 1950 to 1979 (http://jisao.washington.edu/data/globalsstenso). The G index is the leading principal component of global sea surface temperature anomaly deviations (Zhang, Wallace, and Battisti 1997). Figure4 plots the Global SST ENSO index against the ISCCP monthly

area-averaged low cloud amount near the Peruvian region during the period of 1985 to 1997. The original data series is in the upper panel; the annual mean has been removed from both the Global SST ENSO index and the low cloud amount in the lower panel. The Global SST ENSO index is strongest during 1986 to 1987 and in 1997; every year the Global SST ENSO index has clear seasonal variation with approximately 0.4K seasonal amplitude. The observed ISCCP low cloud amount is significantly correlated with the ENSO index when the annual mean is removed from both time series; the ISCCP low cloud reaches its seasonal peak approximately one month ahead of the Global SST ENSO index in the Northern summer. The correlation between the Global SST ENSO index and ISCCP low cloud amount one month ahead is 0.39, and the in phase correlation is 0.35. Park and Leovy's recent study (2004) also found no significant relationship between tropical ship low cloud cover anomaly and the Global SST ENSO index.

Wavelet analysis is a useful tool for analyzing localized variations of power within a geophysical time series. The practical guide and application examples can be found in the recent work (Torrence C. and G.P. Compo, 1998; Jevrejeva S., J.C. Moore, and A. Grinsted, 2003; Grinsted A., J.C. Moore, and S. Jevrejeva, 2004). Wavelet analysis of the coherence between Global ENSO index (the Global SST ENSO index and the G index) and monthly low cloud amount from ISCCP D-series, the KH scheme, and the new scheme is shown in Figure 3.5.

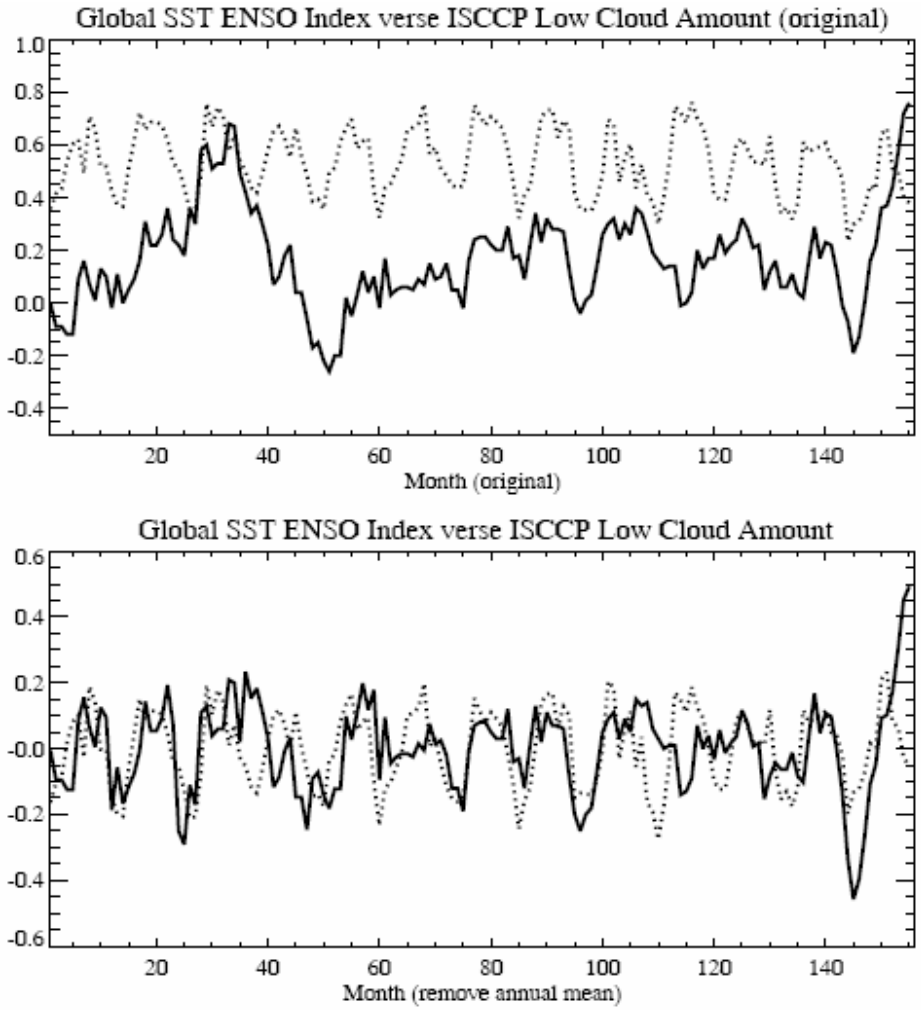


**Figure 3.4** Global SST ENSO index versus the ISCCP monthly area-averaged low cloud amount near the Peruvian region during the period of 1985 to 1997.

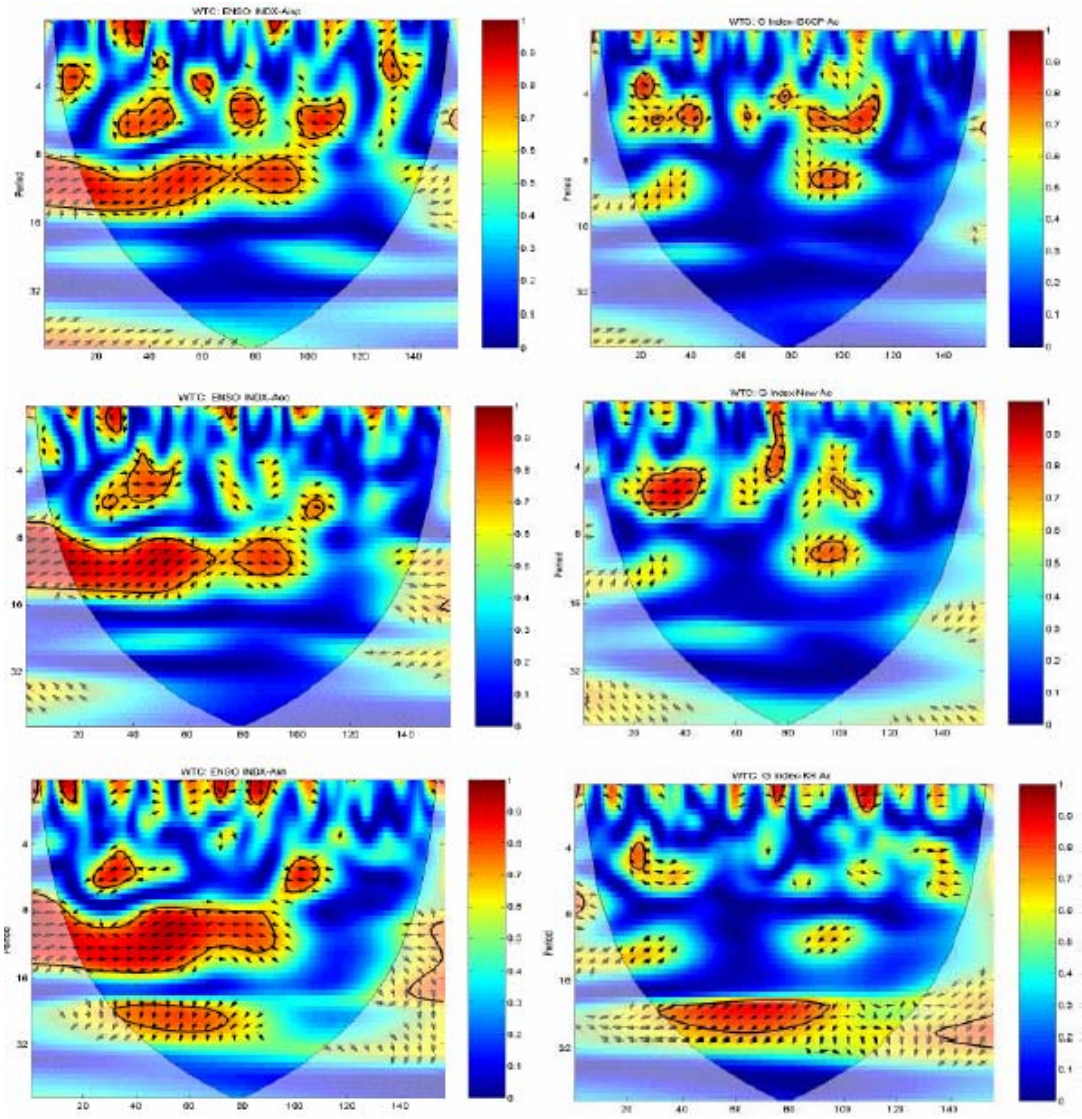

**Figure 3.5** Wavelet analysis between two monthly ENSO indexes and area-averaged low cloud fraction from ISCCP D-series (upper panel), the new scheme simulated results (middle panel), and the KH scheme simulated results (lower panel) during the period of 1985 to 1997near the Peruvian regions. The ENSO index used in the left panels is the Global SST ENSO index, the ENSO index used in the right panels is the G ENSO index.

It shows no significant relationship between Global ENSO indexes and ISCCP low cloud amount when the variation period is larger than 16 months. The new scheme has similar coherence with two ENSO indexes as that of ISCCP data. However, the KH scheme has significant coherence in both the seasonal cycle and the interannual variations.

From Figure3.6, a wavelet analysis of coherence between two ENSO indexes and SST shows a significant relationship in both seasonal variations and interannual variations. However, two ENSO indexes are correlated with vertical transport heating only on the seasonal cycle; no significant relationship is found on the inter-annual time scales. From Table 2, monthly ISCCP D-series low cloud amount variations have a better correlation with vertical transport of dry static energy than with lower tropospheric stability associated with SST. This explains why ISCCP low cloud and the new scheme simulated low cloud have no relationships with ENSO on interannual time scale but the stability based scheme has.

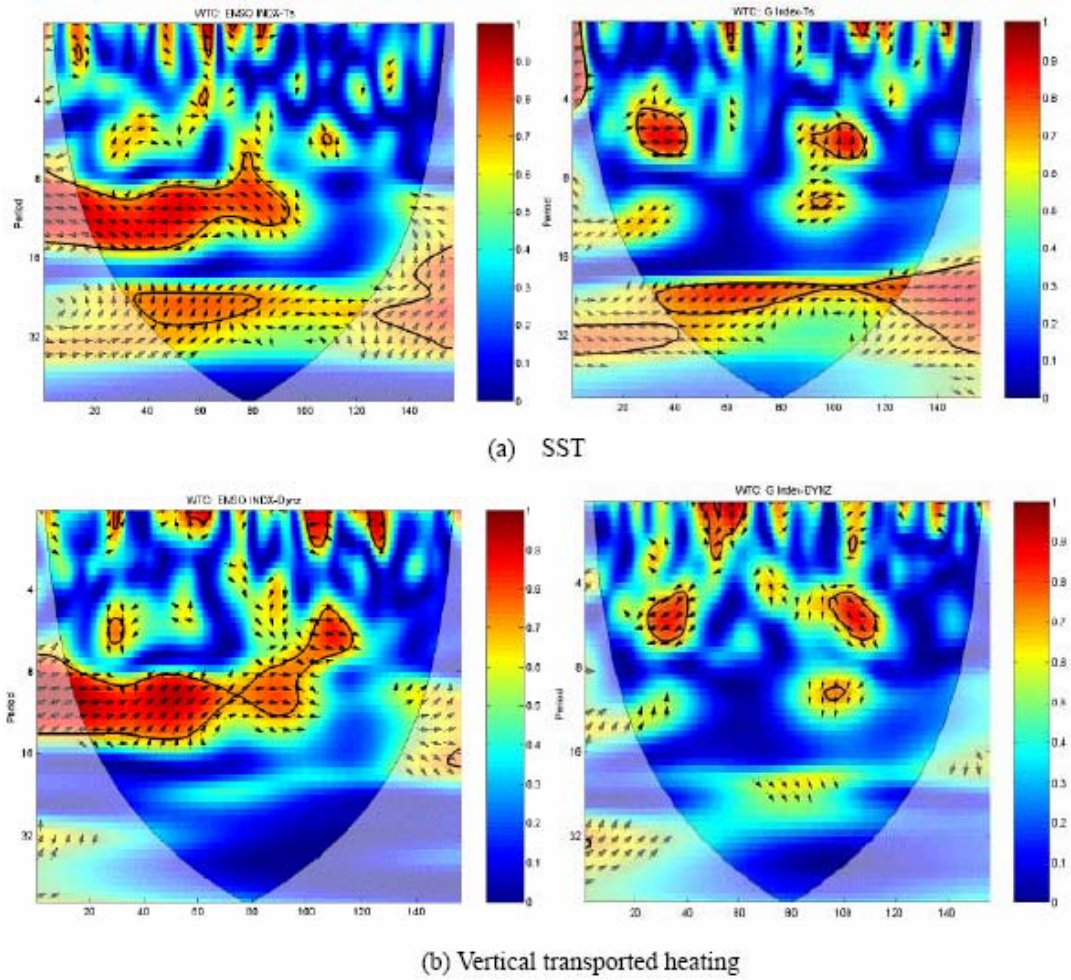


**Figure 3.6** Wavelet coherence between ENSO index and monthly area-averaged SST and vertical transport heating near the Peruvian region during the period of 1985 to 1997. The ENSO index used in the left panels is the Global SST ENSO index, the ENSO index used in the right panels is the G ENSO index.

### 3.1.4 Spatial Variation of Low Cloud Amounts, Dynamical Transport Heating and Convective Heating for the Season of JJA

Bajuk and Leovy (1998) found the similar spatial variations among SST, large scale divergence, OLR, and cloud type frequency over the Tropical Pacific and Indian Oceans from ship observations. Norris (1998a, 1998b) studied the spatial variation of low cloud, surface advection, surface divergence, and boundary layer structure. His study suggested that different low cloud types associated with different meteorological conditions. Figure3.7 shows the spatial distribution of monthly low cloud amount, total dynamical transport heating and convective heating in four MSC regions during the period of 1985 to 1997 in JJA season. The low cloud amount variation is from EERCA ship data, ISCCP D-series satellite data, the new scheme results, and the KH scheme results. EECRA maximum low cloud amount occurs both near the coast and away from the coast. The KH stability scheme simulates the maximum low cloud amount only near the coast regions; the new scheme simulates more realistic spatial variations due to the contribution of total dynamical transport heating.

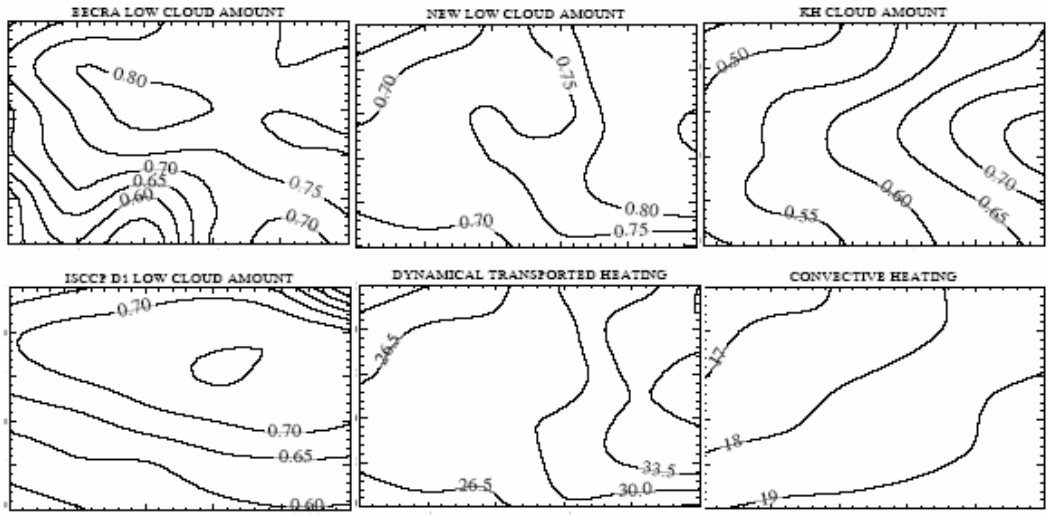


(A) PERUVIAN

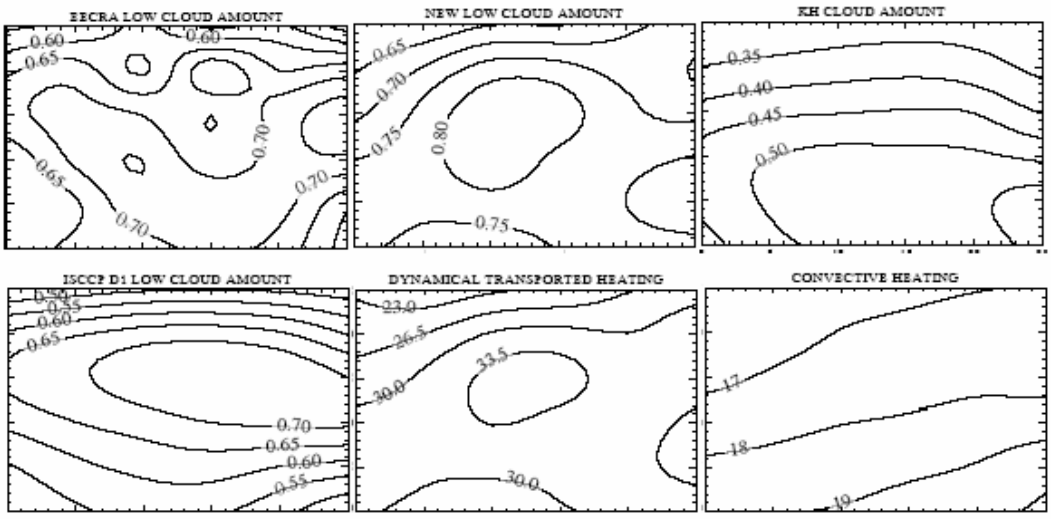


(B) NAMIBIAN

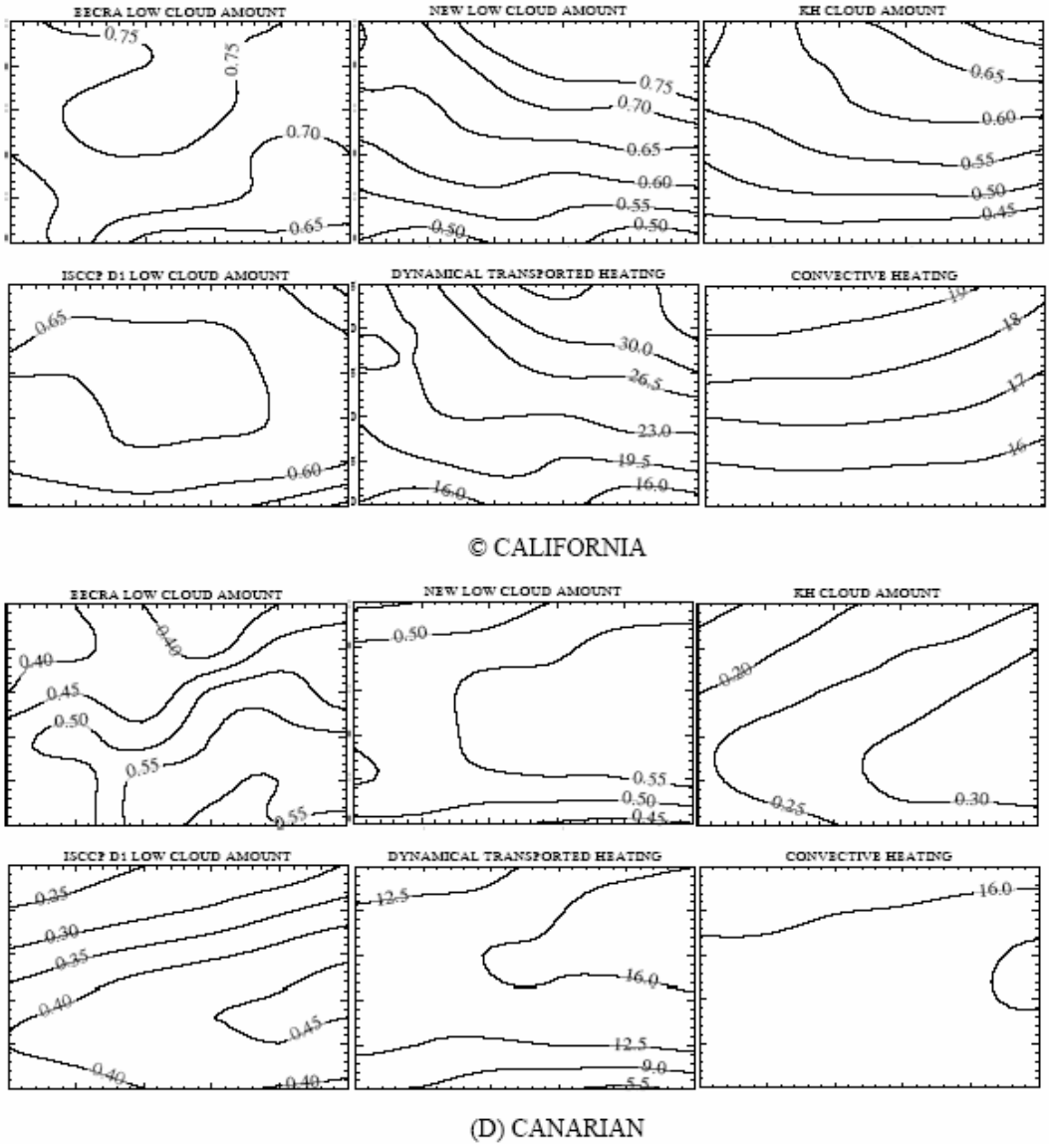


**Figure 3.7** Spatial distributions of 11-year averaged monthly mean low level cloud amount in the four MSC regions calculated from the EECRA ship data, the ISCCP D-series, the new cloud cover scheme, the KH scheme, the total dynamical transported heating, and the convective heating during the season of JJA in the Peruvian, Namibian, California, and Canarian regions.

## 3.2 NCAR CAM3.1 Simulation Results

### 3.2.1. Experimental Design

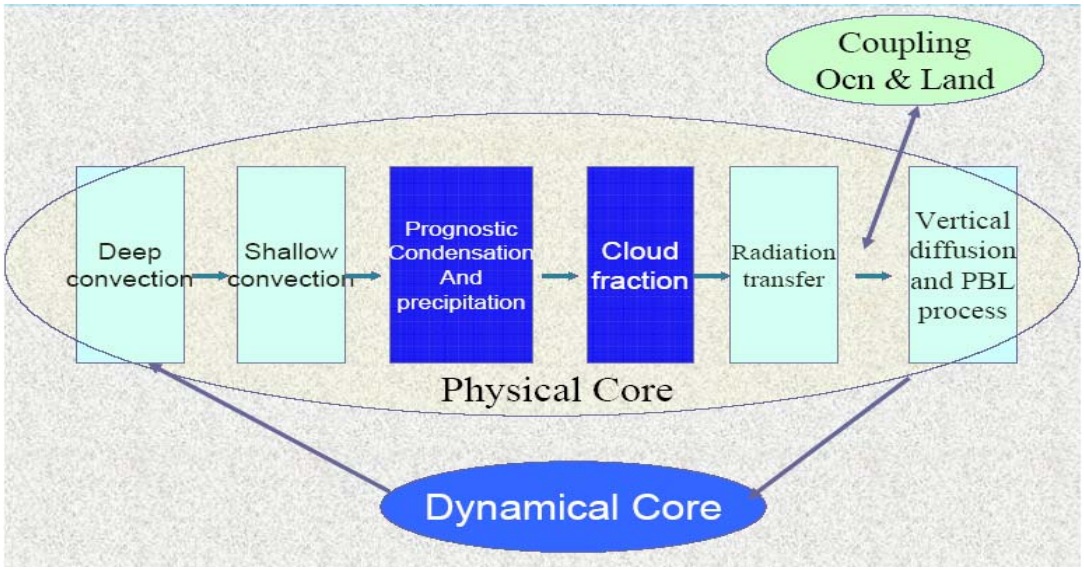


**Figure 3.8** CAM3.1 model physical and dynamical structures

One six-year experiments and one control run were performed at T42 resolution initialized on 1 Jan. 1984 using the NCAR Community Atmospheric Model version 3.1 (CAM3.1) coupled with the NCAR Community Land Model version 3 (CLM3) and forced by an AMIP SST dataset. CAM3.1 model physical and dynamical structures are shown in Figure3.8. In both runs, the model was spun up for one year. The NCAR CAM3.1 standard low cloud cover scheme was used in the control run (see NCAR CAM3.1 documentation). Three types of low clouds are diagnosed by CAM3.1 scheme: low level marine stratus, convective cloud, and layered cloud. Layered clouds form when the relative humidity exceeds 90% over the subtropical oceans. Low level marine stratus

forms below the maximum temperature inversion layer when the inversion strength exceeds a critical value of -0.125 $K\ pa^{-1}$. Its fraction is diagnosed based on an empirical linear relationship proposed by Klein and Hartmann (1993). The total cloud cover is determined using a maximum overlap assumption for cloud types within each grid box. The new scheme is a method to estimate the total low cloud fraction and is not limited for a specific cloud type. When MSC overlaps shallow cumulus, MSC cloud fraction diagnosed near the inversion layer represents the low cloudiness variations. In the model experiment, boundary layer cloud is assumed to occur just beneath the inversion layer and no cloud is present in other layers within the lower troposphere; the low cloud cover is diagnosed using the new scheme whenever the inversion strength exceeds zero; and the maximum vertical velocity in the lower troposphere is used to calculate the vertical transport term in the new scheme. Inputs for the new scheme include current grid values of vertical velocity, horizontal winds and air temperature at the bottom four levels, and the lower troposphere stability. The horizontal transport heating in the second term on the right side of equation (2.39) is calculated first in the dynamical core then transferred into the cloud fraction parameterization code. The first term (vertical transport heating) and the third term (convective heating) of equation (2.39) are calculated directly in cloud fraction parameterization code. In subtropical MSC regions, low marine stratus is the dominant cloud type. Therefore, low cloud fraction is determined mainly by the low marine stratus fraction diagnosed using the new scheme near the maximum temperature inversion layer.

### 3.2.2. Spatial Distributions of Summer Low Cloud Fractions and Surface Radiations

Marine boundary clouds have their seasonal maximum in summer in most MSC regions. Figure3.9 shows the spatial distributions of differences in summer low level cloud cover between the ISCCP observations, the model control run, and the experimental run during the season of JJA. ISCCP data varies in both space and time, its spatial distribution is more reliable, but ISCCP low cloud fraction is 5% to 10% less than that of EERCA ship observations as discussed in Chapter 2. Compared to ISCCP observations, the model tends to estimate 30% to 50% more low cloud near most coastal regions. These cloud amount differences decrease away from the coast in the California, Canarian, and Peruvian regions. The new scheme simulates better spatial patterns in all MSC regions as shown in Figure 3.9. Generally speaking, the new cloud cover scheme simulates less low clouds near the coastal regions and more clouds away from the coast.

Figure 3.10 is the difference in spatial distribution of net downward shortwave radiation flux difference at surface between ISCCP FD data, the model control run, and the model experimental run. Compared to observations, the shortwave radiation is underestimated by as large as $50 W\ m^{-2}$ near the coastal region, and is overestimated by the similar amounts away from the coast in all four regions. The new scheme corrects the biases in surface shortwave radiation flux by approximately 20 $W\ m^{-2}$ in all MSC regions.

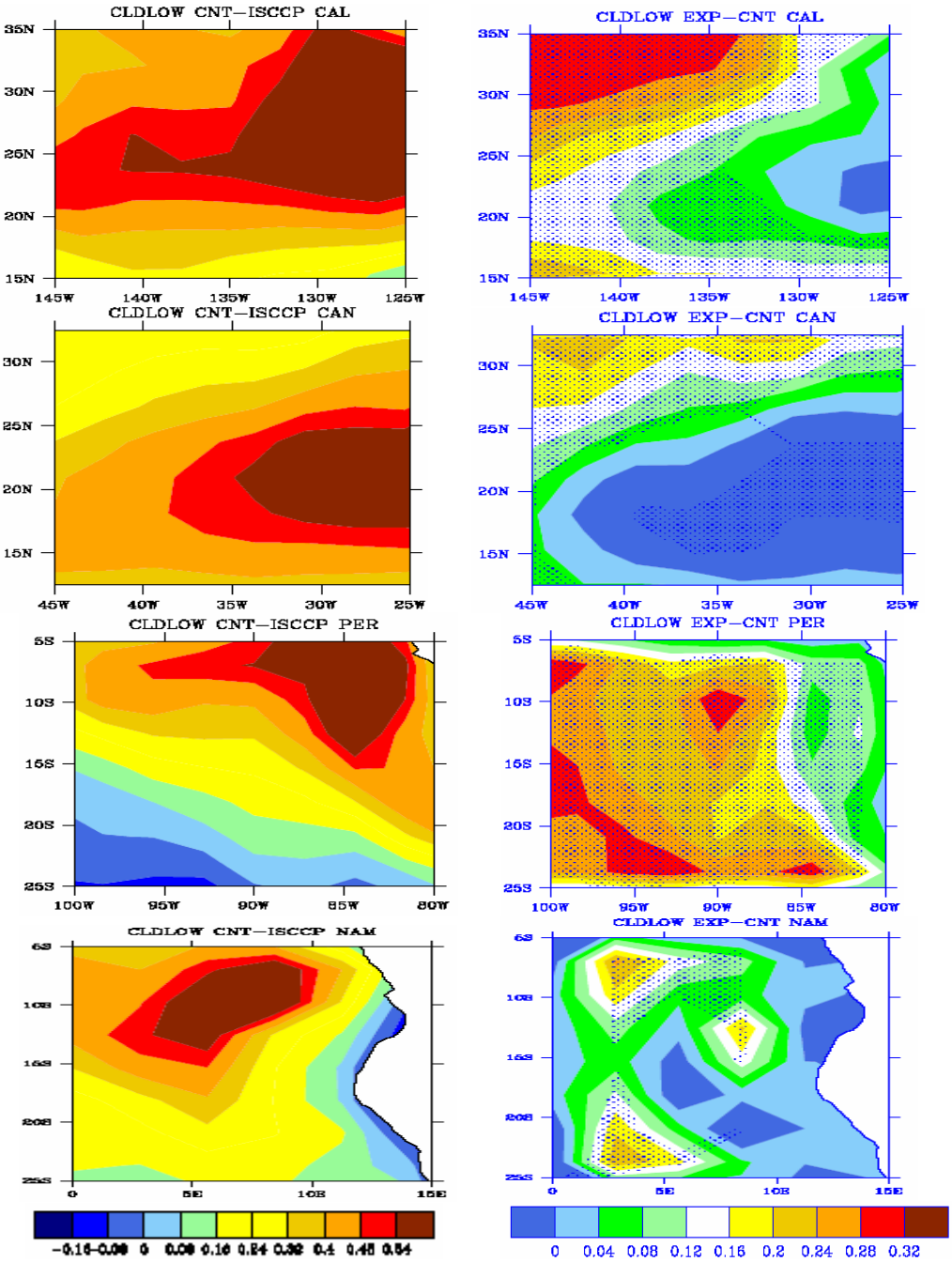


**Figure 3.9** Spatial distributions of differences in low level cloud amounts between observations and the model simulations from the control run and the CAM3.1 experiment during the period from 1985 to 1989; the differences are averaged in JJA near the Peruvian, Namibian, California, and Canarian: control-observation (left), CAM3.1 Exp.-control (right).The dotted areas in the middle and the right panel represent the grid cells with a significant difference at the 5% level.

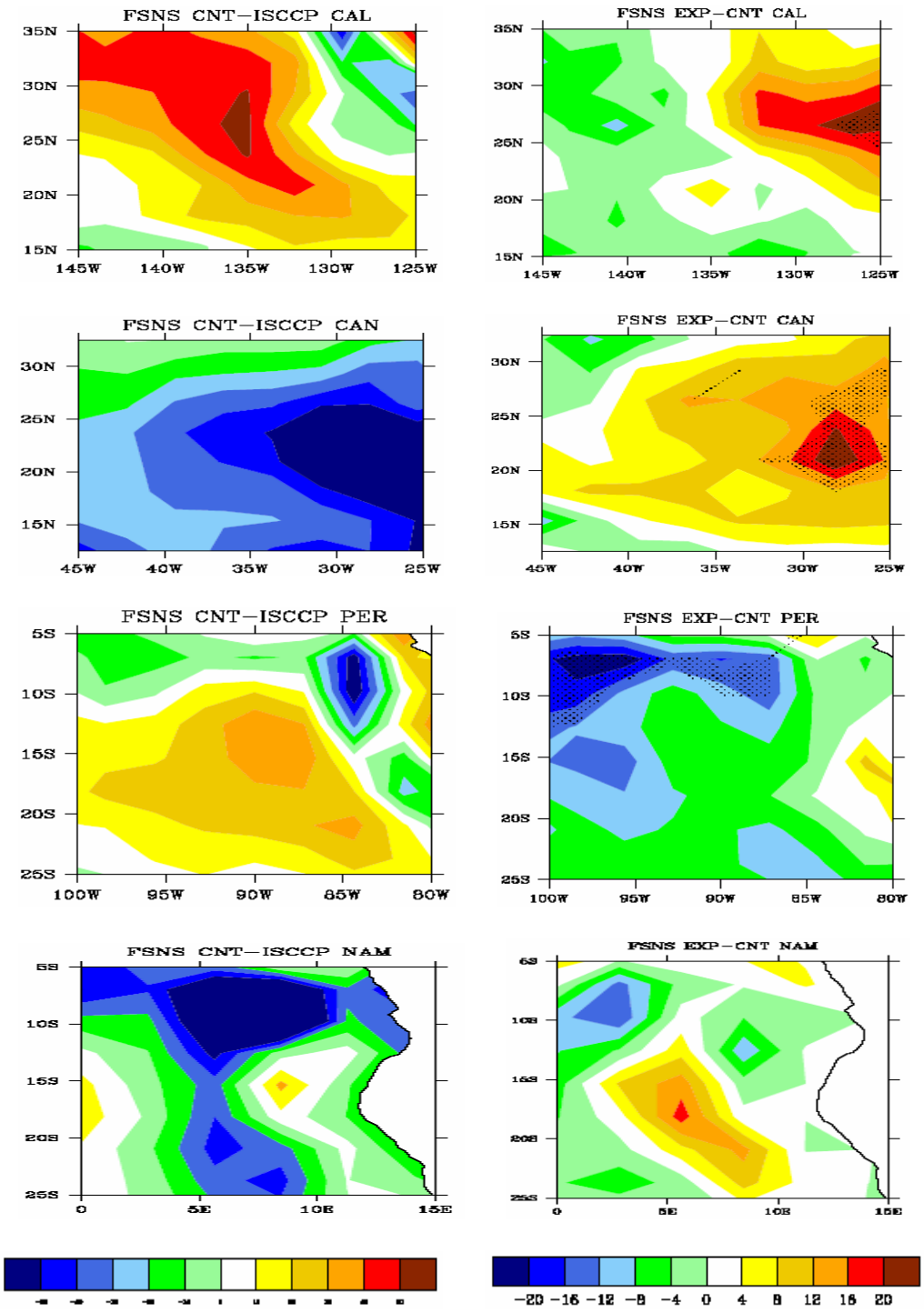


**Figure 3.10** Same as Figure 3.9 but for net downward shortwave radiation at surface ($W\ m^{-2}$).

Figure 3.11 is the spatial distribution of the net upward longwave radiation flux difference at surface between the ISCCP FD data, the model control run, and the model experimental run. The radiation flux is overestimated by 20 to 100 $W\ m^{-2}$ in all four regions. The largest positive biases occur away from the coast in the California, Canarian, and Peruvian regions. The new scheme reduces the positive biases by 10 to 15 $W\ m^{-2}$ in most regions. The biggest bias reductions are also found to be away from the coast in the California, Peruvian, and Namibian regions.

### 3.2.3. Spatial Distributions of Summer Cloud Liquid Water and Large Scale Precipitation

Figure 3.12 is the spatial distributions of differences between CAM3.1 experimental run and the control run in grid-averaged liquid water path and large scale precipitation in the season of JJA during the period from 1985 to 1989. Less large scale precipitation and grid-averaged liquid water (LWP) are simulated near the California coast, the Canarian coast, and away from Namibian coast. More large scale precipitation and LWP are simulated in the Peruvian regions. There is good agreement of spatial pattern between LWP and large scale precipitation.

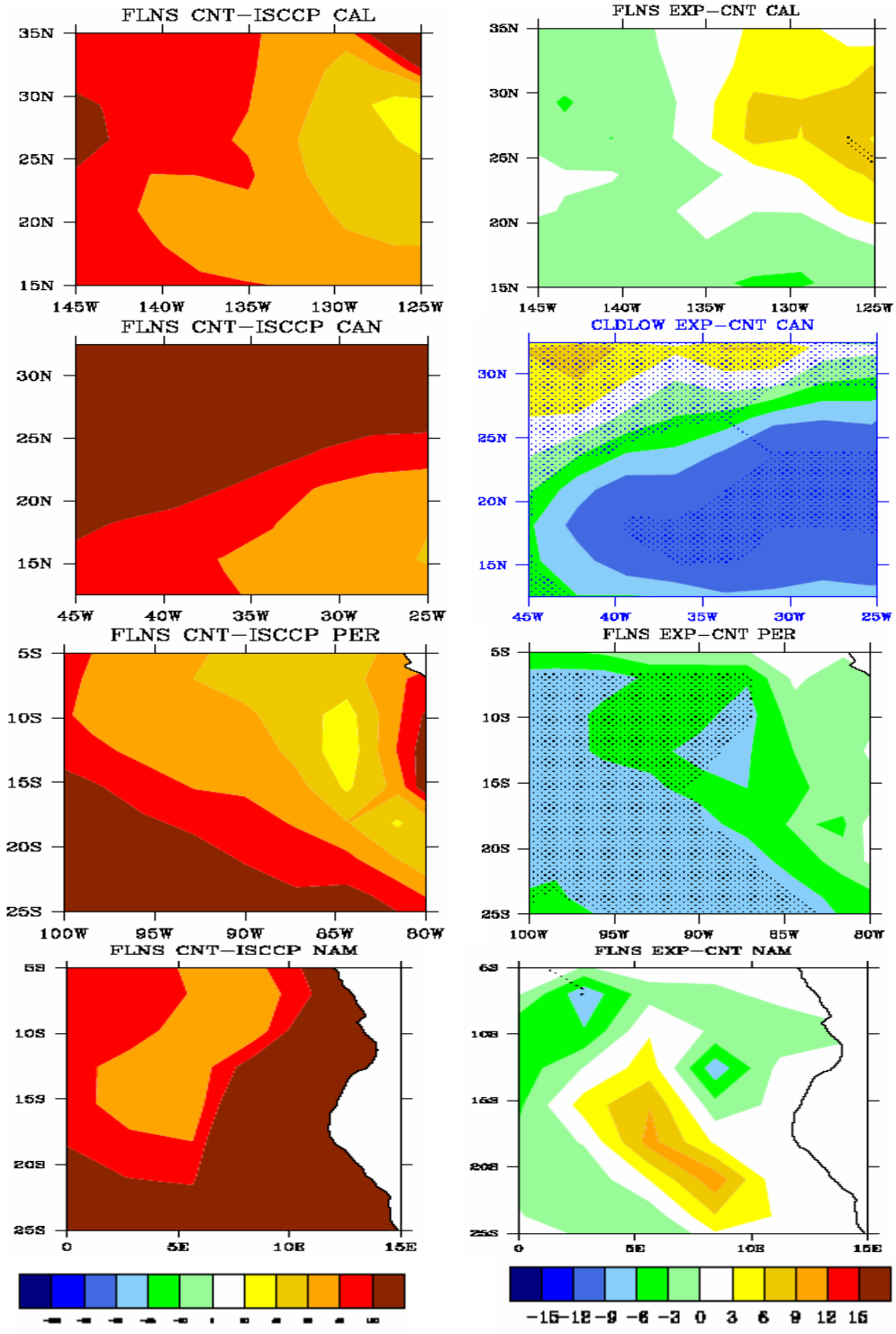


**Figure 3.11** Same as Figure 3.9 but for net upward longwave radiation at surface ($W\ m^{-2}$).

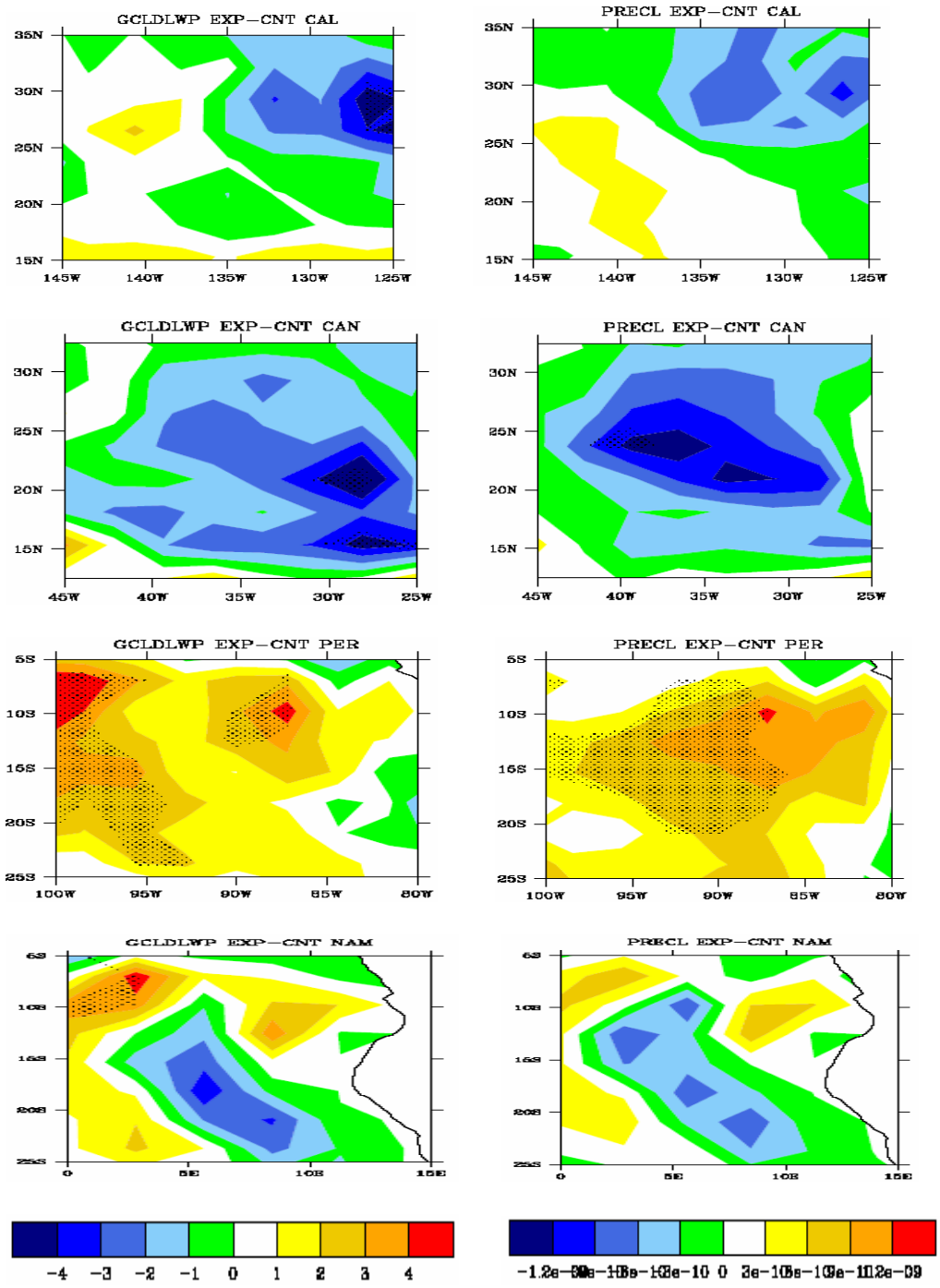


**Figure 3.12** Spatial distributions of differences (CAM3.1 Exp.-control) in grid-averaged liquid water path (left panel) and large scale precipitation (right panel) from 1985 to 1989; the differences are averaged in JJA near Peruvian, Namibian, California, and Canarian. The dotted areas in the middle and the right panel represent the grid cells with a significant difference at the 5% level.

### 3.2.4. Seasonal Regional Analysis of Low Cloud Fraction, Cloud Liquid Water, and Precipitations

Current GCMs underestimate low cloud fractions in subtropical MSC regions.. The seasonal cycle of low cloud fraction is better simulated in the model experimental run than the control run as shown in Figure 3.12. Compared to EECRA ship observations, the new scheme overestimates winter time marine boundary cloudiness in all subtropical MSC regions; because the total dynamical transport of convective dry energy is overestimated in CAM3.1 compared to ERA40 reanalysis results in three MSC regions as evidenced in Figure 3.13. The overestimation of low cloud fraction near the Canarian region is not due to overestimation of dynamical transport, but because more convective cloud and relative-humidity controlled clouds are simulated in the model.

There is no simple relationship between inversion-related low cloud fraction and cloud liquid water path. The new cloud cover scheme simulated more low cloud fraction near the inversion layer; however, Figure 3.14 shows that the lower troposphere grid-averaged cloud liquid water path (LWP) has been increased only in the summer Peruvian region. There are no significant changes in both the Namibian region and the California region; and there is a decrease of LWP in the summer Canarian region. The precipitation is formed during the sedimentation process in Zhang-McFarlane deep convection scheme and during the microphysical process in the prognostic cloud scheme. The model LWP depends directly on the large scale precipitation. Figure3.15 is the model simulated seasonal cycle of large scale precipitation. More stratiform precipitation is simulated in the experimental run in the summer Peruvian region and less precipitation

in the summer Canarian regions, which agree with the LWP changes in Figure 3.15. In the current CAM3.1, the new cloud cover scheme has not yet be fully coupled with cloud prognostic scheme and convection scheme; hence, improvement of the low cloud cover scheme has not yet led to increased LWP in most MSC regions, this deficiency should be improved in future development.

### 3.2.4 Seasonal Analysis of Energy Budget at TOA and Surface

The existence of marine stratus and stratocumulus greatly reduces the net downward shortwave radiation flux at TOA and the surface because of the large cloud albedo; it also reduces the net upward longwave radiation flux at TOA and surface because of lower cloud top temperature and large downward longwave cloud emission. The existence of marine boundary clouds can also affect surface flux through changing boundary layer turbulence mixing and surface wind-cloud feedback.

*a. Peruvian*

The seasonal cycle in TOA and surface latent heat flux in the Peruvian region is shown in Figure 3.17. Compared to ISCCP FD radiation flux at TOA and at surface, CAM3.1 overestimates net downward shortwave radiation flux at TOA and surface by 10 $W\ m^{-2}$ and 20 $W\ m^{-2}$ in the season of January to June; and overestimates net upward longwave radiation flux by 20 $W\ m^{-2}$ at TOA and by 10 $W\ m^{-2}$ during Jan. to May, and by 40 $W\ m^{-2}$ during June to Dec. because of underestimation of low cloud optical depth. As large as 20% more low cloud fraction has been simulated using the new cloud cover scheme; however because the model simulated LWP is only increased slightly in the summer Peruvian, there is little change in cloud optical depth in most season. As a

result, the regional average of shortwave radiation flux is only slightly improved by 10 $W\ m^{-2}$ during JJA in the Peruvian and little change of radiation flux in other seasons. Surface latent heat flux is significantly reduced by 10 $W\ m^{-2}$ in the experimental run during the season of May, June, and July due to reduced turbulent stress near the surface. Regional averaged sensible heat flux has little change in all seasons.

The seasonal energy fluxes at the TOA and surface near the Canarian region are shown in Figure 3.18. The shortwave radiation fluxes are underestimated in the Canarian region. The LWP is decreased in the model experimental run, which leads to reduced biases in the shortwave radiation flux at TOA and surface. The longwave radiation fluxes are overestimated at TOA in most seasons and at the surface in the summer season. The bias is slightly reduced for the summer surface. Surface latent heat flux is slightly increased when the downward shortwave radiation fluxes are increased in the summer season.

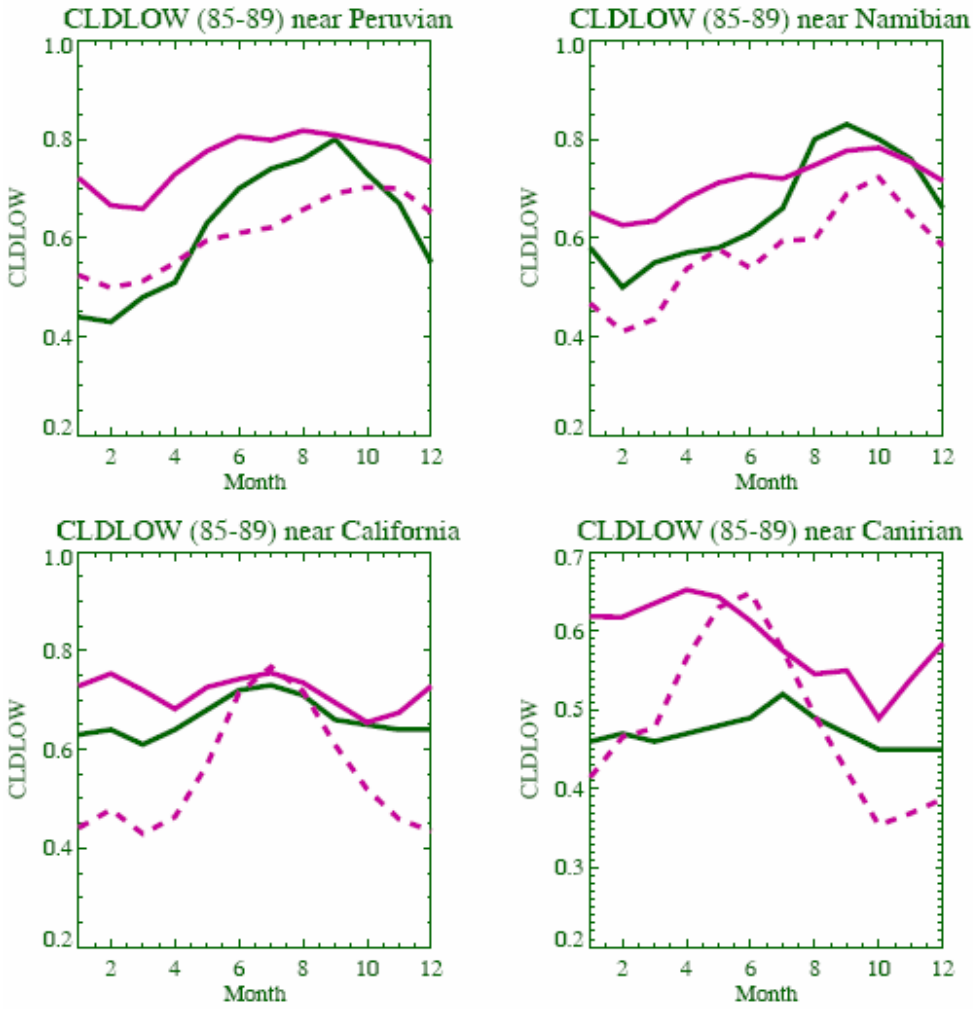


**Figure 3.13** Seasonal variations in low cloud cover between EECRA observation and the model simulation averaged over regions in Table 1 from 1985 to 1997. The green solid line is from EECRA observations; the red dotted line is from CAM3.1 control run; the solid red line is from CAM3.1 Experiment.

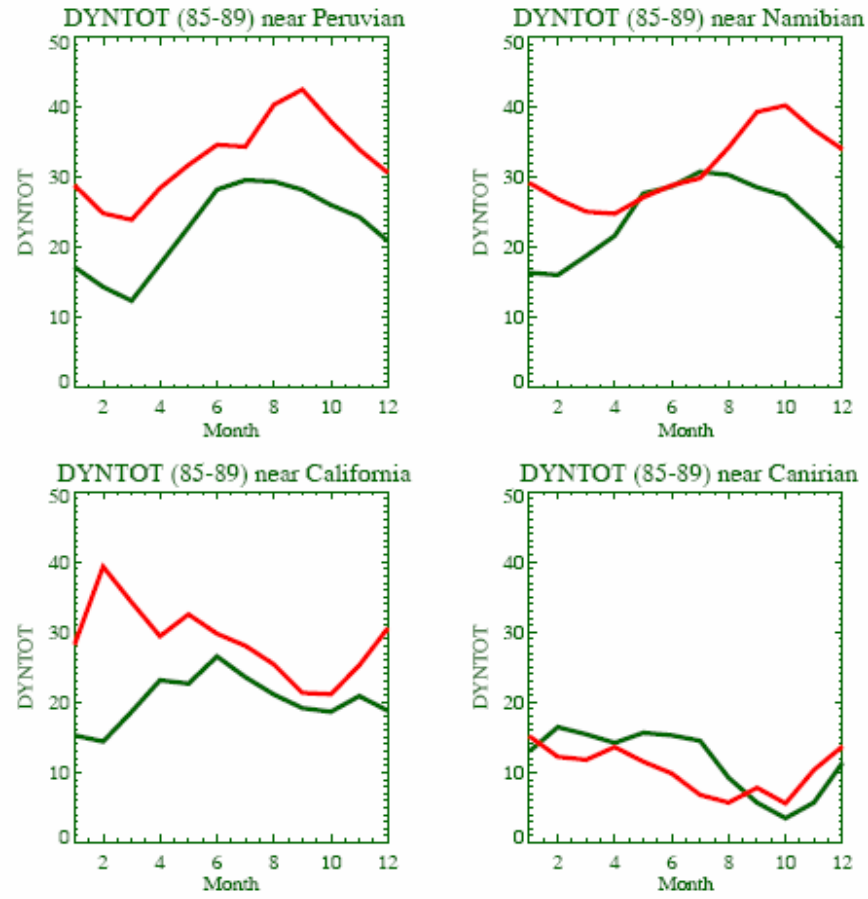


**Figure 3.14** Seasonal variations in total dynamical transport of heating between ERA40 reanalysis (green line) and the model experimental result (red line) averaged over regions in Table 1 from 1985 to 1989.

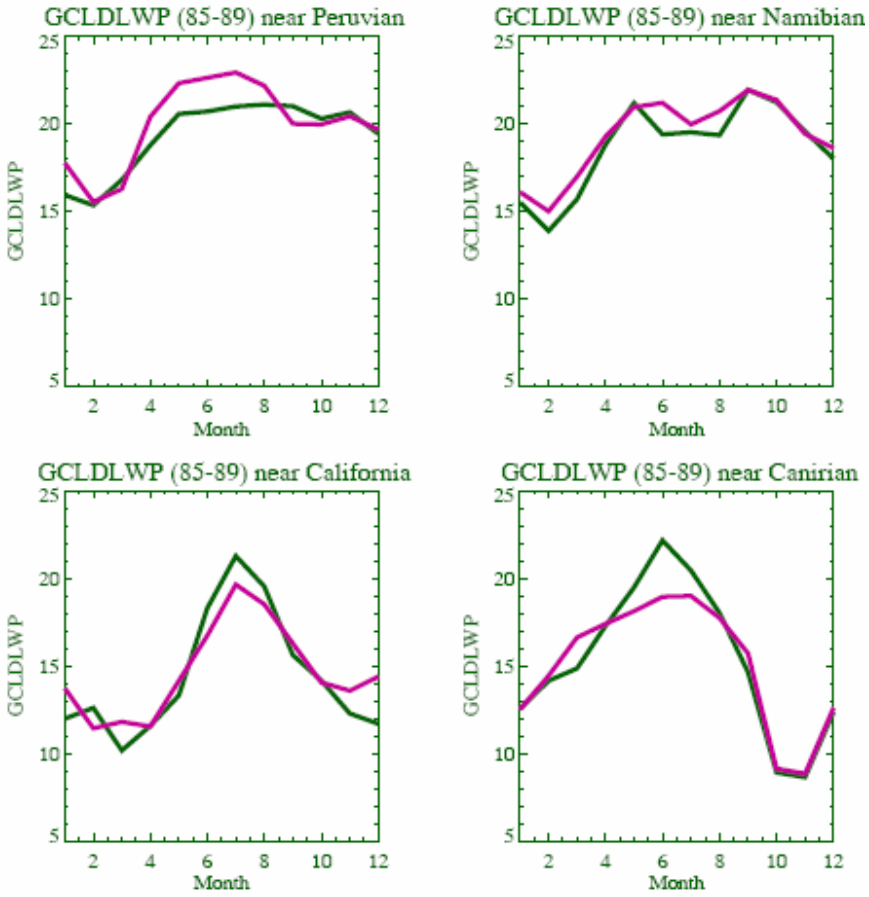


**Figure 3.15** Model simulated cloud liquid water path ( $g/m^2$ ) in the model's lowest four levels averaged over regions listed in Table 1 from 1985 to 1989. The green line represents the control run results and the blue line represents the experiment run results.

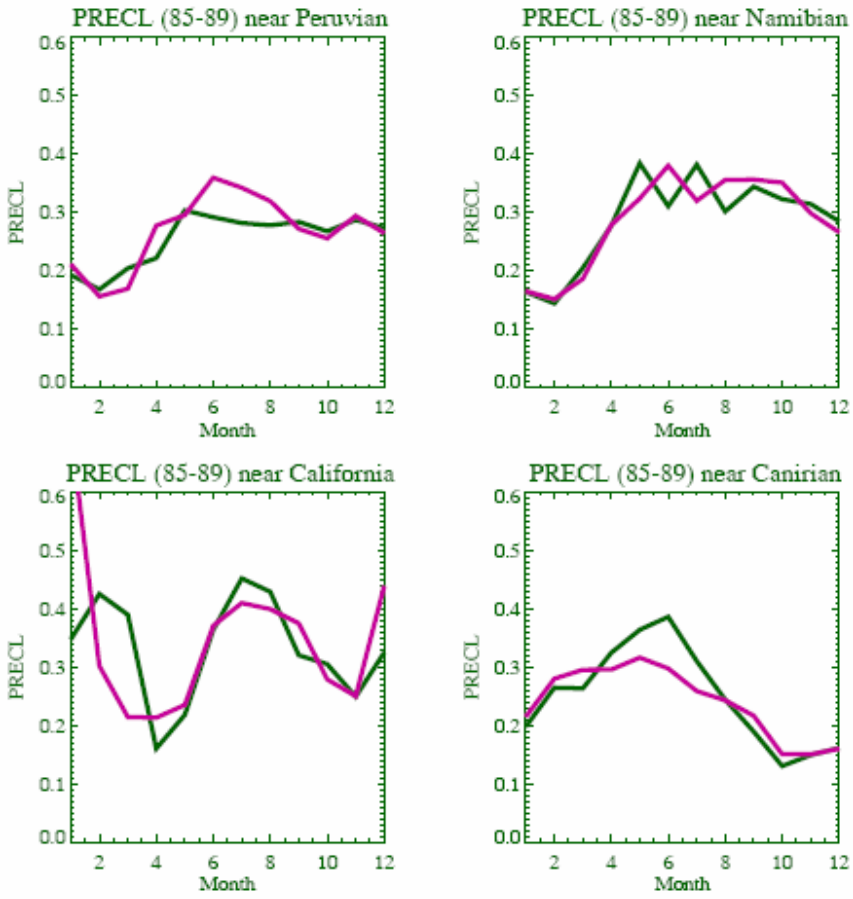


**Figure 3.16** Model simulated large scale stratiform precipitation ($m/day$) averaged over regions listed in Table 1 during the period from 1985 to 1989. The green line represents the control run results and the blue line represents the experiment run results.

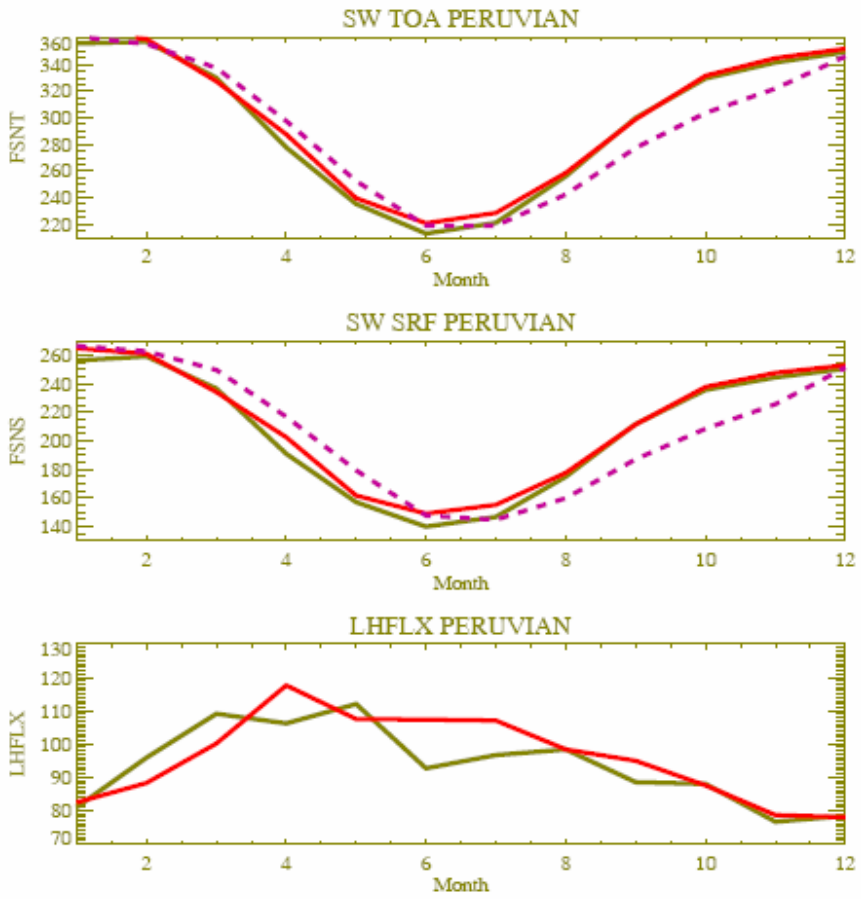


**Figure 3.17** Seasonal cycles of (a) the TOA net shortwave flux, (b) the surface net shortwave flux, and (c) the surface latent heat flux in the Peruvian region averaged during the period from 1985 to 1989. The solid red line represents the control run results, the solid green line represents the model experimental run results, and the dashed pink line represents the ISCCP FD radiation flux.

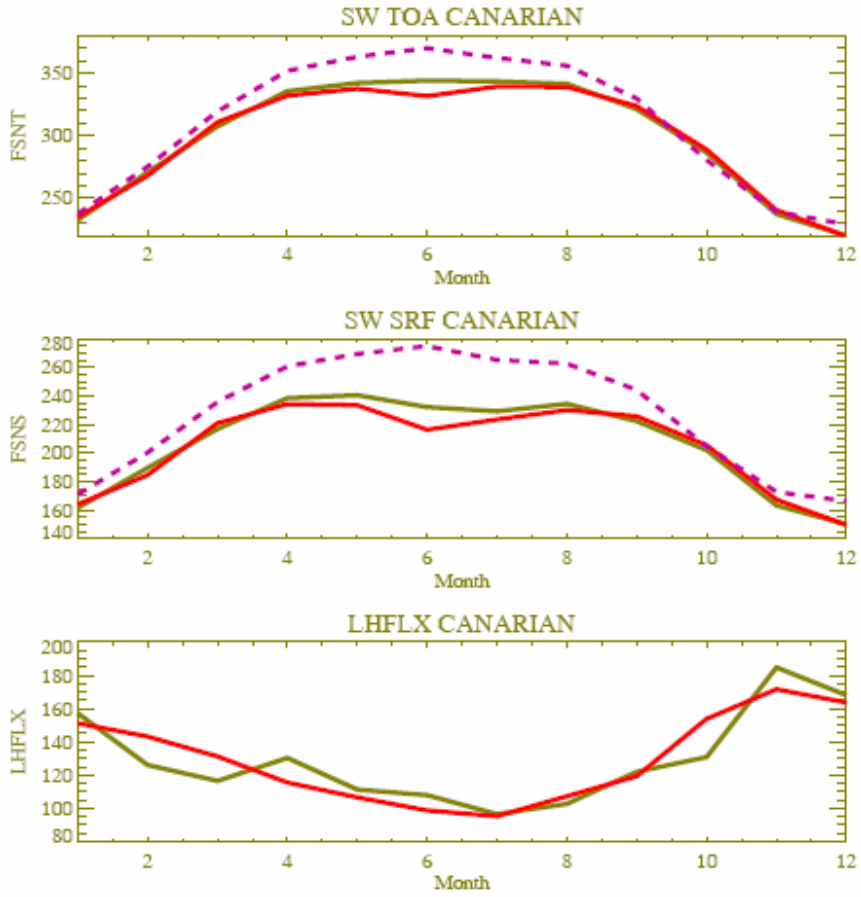


**Figure 3.18** Seasonal cycles of (a) the TOA net shortwave flux, (b) the surface net shortwave flux, and (c) surface latent heat flux in the Canarian region during the period from 1985 to 1989. The solid red line represents the control run results, the solid green line represents the experimental run results, and the dashed pink line represents the ISCCP FD radiation flux.

## 3.3 Conclusions

A simple low cloud cover scheme based on lower tropospheric stability and convective inhibition energy within the lower troposphere is developed in part I. In part II, seasonal variations and interannual variations of low cloud variations are examined in both offline experiments and NCAR CAM3.1 simulations. Offline experiments have found that total ADIN dynamical transport plays the most important role in determining seasonal variations and spatial variations of low cloud amount; while horizontal transport heating and convective heating associated with SST anomalies are crucial in determining the inter-annual variations of low cloud amount in most MSC regions.

The new scheme produces realistic seasonal variations of the observed EECRA low cloud amounts in all MSC regions; and explains 25% more covariance than that using KH scheme for monthly ISCCP D-series low cloud amount near the Peruvian and Canarian region during the period from 1985 to 1997. A wavelet analysis shows a strong positive relationship between Global SST ENSO index and EECRA and ISCCP low cloud amount in seasonal variations, but little coherence on time scales larger than 2 years near the Peruvian region. However, the KH scheme simulates an unrealistic relationship with ENSO index for the interannual variations due to its strong dependence on SST; the new scheme removes this bias due to its dependence on local vertical transport of dry static energy, which has weak coherence with ENSO at longer time scales. The new scheme also reproduces a much better low cloud spatial variation than KH scheme during JJA season in the four MSC regions.

Most current GCMs underestimate low cloud fraction in the MSC regions. When implemented into NCAR CAM3.1, 15% to 20% more low cloud has been simulated in

the four MSC regions. The new scheme systematically reduces the model biases in the spatial distributions of low cloud fraction and the net shortwave and longwave radiation fluxes at surface in all MSC regions. However, the better simulated seasonal variations of low cloud fractions do not result in large improvements in the seasonal variations of surface radiation fluxes and heat fluxes, because the model simulated cloud liquid water path did not significantly change although the cloud fractions are greatly increased in most seasons.

# CHAPTER 4

# ON THE RELATIONSHIPS BETWEEN LOWER TROPOSPHERE AVAILABLE THERMAL INHIBITION ENERGY AND LOW STRATIFICATION CLOUD AMOUNT

## 4.1 Introduction

The objective of this chapter is to seek a single predictor for low stratiform cloud amount based on the gross dry stability discussed in Chapter 2. Using a single predictor for cloud cover parameterization in climate models is appealing because it is computational efficient and easy to capture key feedbacks in a changed climate. Observations show good relationships between lower troposphere stability $\Delta\theta_{700}$ and low stratiform cloud amounts on daily to inter-annual timescales (Slingo 1987; Klein and Hartmann 1993; Wood and Hartmann 2005). It suggests a positive feedback between boundary layer clouds and ocean surface SST. The empirical relationship between $\Delta\theta_{700}$ and cloud fractions has been used in the low cloud cover parameterization in global climate model simulations (Slingo 1987, CCM3 and CAM3.1 documents), the climate sensitivity study (Larson et al. 1999) and the thermostat hypothesis of Miller (1997). The most recent study of Wood and Bretherton (2006) has shown that a more refined measure of cloud top inversion strength is even more skillful.

A physical based cloud cover scheme is developed and tested in Chapter 2 and Chapter 3 which depends on both large scale circulations and local thermal structures. The key assumption is that low clouds are developed to adjust the local thermal structure toward a preferred mean state such that convection is restricted within the lower

troposphere. It simulates more realistic seasonal and inter-annual variations of marine boundary cloud cover. In this chapter, a single predictor based on lower troposphere available dry inhibition energy ADIN is inferred from this physically based cloud cover scheme, which is found to be more skillful in predicting monthly and seasonal low stratiform cloud amount variations than is lower troposphere stability. However, on synoptic time scales, it is found that the dynamical transport variation is more closely related to ISCCP low cloud variations. As a result, the new cloud cover scheme based on both large scale circulation and local stability performs much better than single predictors such as ADIN and $\Delta\theta_{700}$.

## 4.2 A Simple Gross Dry Thermal Stability Index for Low Stratifrom Cloud Amount

As shown in Chapter 3, lower troposphere available dry inhibition energy ADIN is defined as

$$\text{ADIN} = \int_0^{z_T} \rho c_p (\theta - \theta_{1000}) dz = \int_0^{z_T} \rho c_p (T - T_{1000}) dz + \rho c_p g Z_T (0.5 Z_T - Z_{1000}) \quad (4.1)$$

In equation (4.1), $Z_T$ represents the trade wind inversion height. We define lower troposphere available thermal inhibition energy as

$$\text{ATIN} = \int_0^{z_T} \rho c_p (T - T_{1000}) dz \quad (4.2)$$

In the case when the trade wind inversion height $Z_T$ and $Z_{1000}$ is relatively constant, then ADIN is mainly determined by ATIN. From chapter 3, the marine boundary cloud fraction is determined by the total dynamical transport of ADIN and convective heating in subtropical MSC regions.

$$A_c = S_c / R^0_{crf} = (0.3A_{dyn}(ADIN) + Q_c)/ R^0_{crf} \quad (4.3)$$

Figure 4.1 is the area-averaged monthly total dynamical transport of ADIN plotted against ATIN during the period from 1985 to 1997 in four subtropical MSC regions. ERA40 reanalysis data is used to calculate ADIN and ATIN. The dynamical transport of ADIN and ATIN are calculated using the method described in Chapter 2. In nature, trade wind inversion height is typically between 800 hpa and 700hpa, which has geographical dependence. A series of experiments which is not shown here found that ATIN is a better empirical predictor for low cloud amounts in most subtropical and middle latitude regions when $Z_T$ is set to the value at 700ha; but ADIN can better predict low clouds in four subtropical MSC regions when it is defined from surface to 800 hpa. When both ATIN and ADIN are defined from surface to 700hpa, simulation performance of the new cloud cover scheme developed in Chapter 2 is slightly affected. To achieve the best performance, ATIN is calculated from surface to 700 hpa and ADIN is calculated from surface to 800hpa in this dissertation.

There is a nearly linear relationship between ATIN and the total dynamical transport of ADIN. When considering only the contribution from local thermal structure, then marine boundary cloud cover can be formulated using an empirical linear relationship as following:

$$A_c = c_1 ATIN + c_2 \quad (4.4)$$

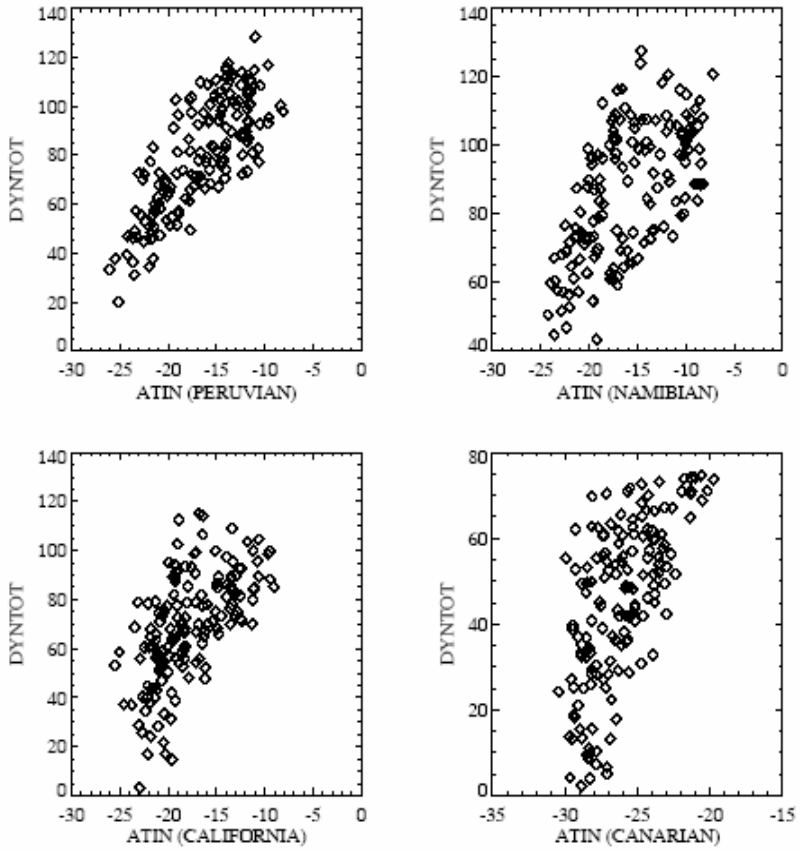


**Figure 4.1** Total dynamical transport of ADIN plotted against ATIN index in four subtropical MSC regions

The empirical relationship is found for eight low stratiform cloud regions in subtropical regions and middle latitude regions which are listed in Table 4.1. Low stratiform cloud cover increases 2% for every $1\ J/m^2$ increase of ATIN.

**Table 4.1 Low stratiform cloud study regions**。

| Peruvian | Namibian | California | Canarian |
|---|---|---|---|
| $(20S-5S)$ $(95W-80W)$ | $(20S-5S)$ $(5W-10E)$ | $(17.5N-32.5N)$ $(135W-120W)$ | $(12.5N-27.5N)$ $(37.5W-22.5W)$ |
| China | Australian | North Pacific | North Atlanta |
| $(17.5N-32.5N)$ $(105E-120E)$ | $(22.5S-37.5S)$ $(92.5E-107.5E)$ | $(37.5N-52.5N)$ $(167.5E-182.5)$ | $(47.5N-62.5N)$ $(312.5-317.5)$ |

$$A_{CIN} = 0.02 * ATIN + 0.935 \tag{4.5}$$

The best fitted coefficients in the equation (4.5) are obtained using grid-averaged monthly mean EECRA low cloud amount and ERA40 data at $2.5^\circ \times 2.5^\circ$ horizontal resolutions from 1985 to 1997. The number of EECRA cloud record in each region is listed in Table 4.2. The EECRA data has the most complete cloud records in China region, which is more than 10 times as many as that of other regions.

**Table 4.2 Total number of EECRA cloud records in each region from 1985 to 1997**

| Peruvian | Namibian | California | Canarian |
|---|---|---|---|
| 26806 | 64142 | 60697 | 46169 |
| Australian | China | North Pacific | North Atlanta |
| 16692 | 3505879 | 161797 | 91496 |

## 4.3 Monthly and Seasonal Low Cloud Variations

Gross dry thermal stability ATIN better predicts low stratiform cloud than most other single large scale environmental predictors on monthly and seasonal timescales. Figure4.2 is monthly averaged low cloud cover from EECRA and scheme simulated cloud cover using $\Delta\theta_{700}$ and ATIN in eight study regions at $2.5^{\circ} \times 2.5^{\circ}$ resolution. The correlation between monthly averaged EECRA low cloud cover and $\Delta\theta_{700}$ predicted values is 0.28; the correlation for ATIN predictor is 0.39. The observed seasonal averaged low stratiform cloud is also much better predicted using ATIN than that using $\Delta\theta_{700}$ as shown in Figure4.3. The correlation between EECRA low cloud and $\Delta\theta_{700}$ prediction is 0.28 using all data in eight regions; the correlation between EECRA data and ATIN prediction is 0.56. The correlation between ISCCP low cloud and $\Delta\theta_{700}$ is 0.21, and the correlation between ISCCP low cloud and ATIN prediction is 0.58. The explained covariance of grid-averaged seasonal variations of low stratiform cloud is improved from 5% to 34% using the ATIN index.

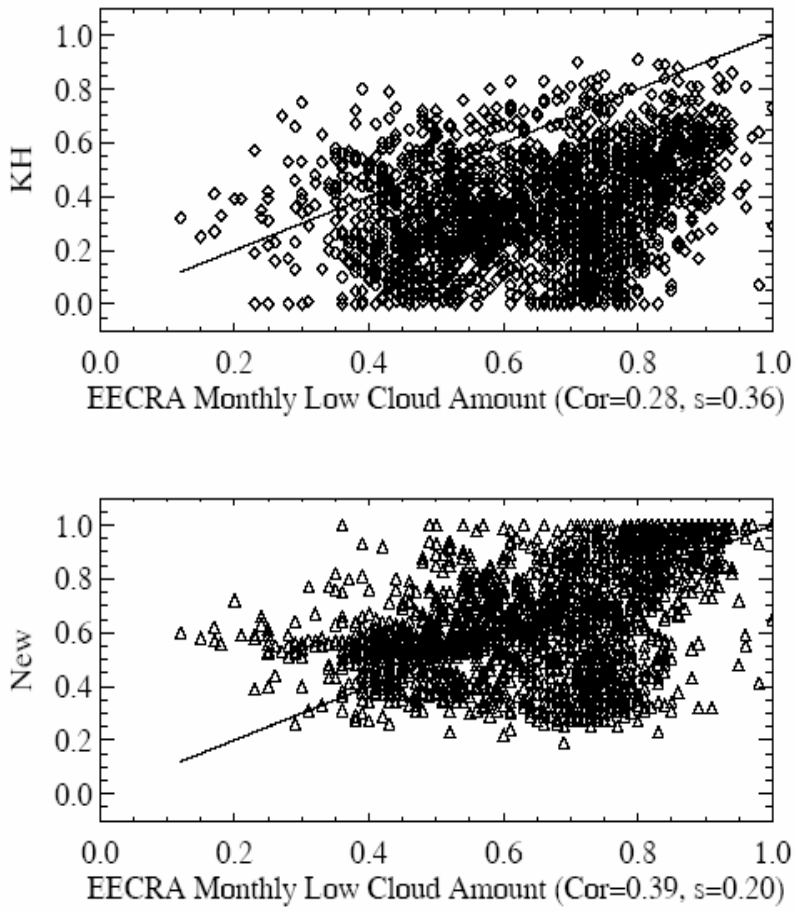


**Figure 4.2**: Monthly averaged low cloud amount from the EECRA observations and the scheme simulated cloud amounts using $\Delta\theta_{700}$ and ATIN in eight study regions at the $2.5^{\circ} \times 2.5^{\circ}$ resolution.

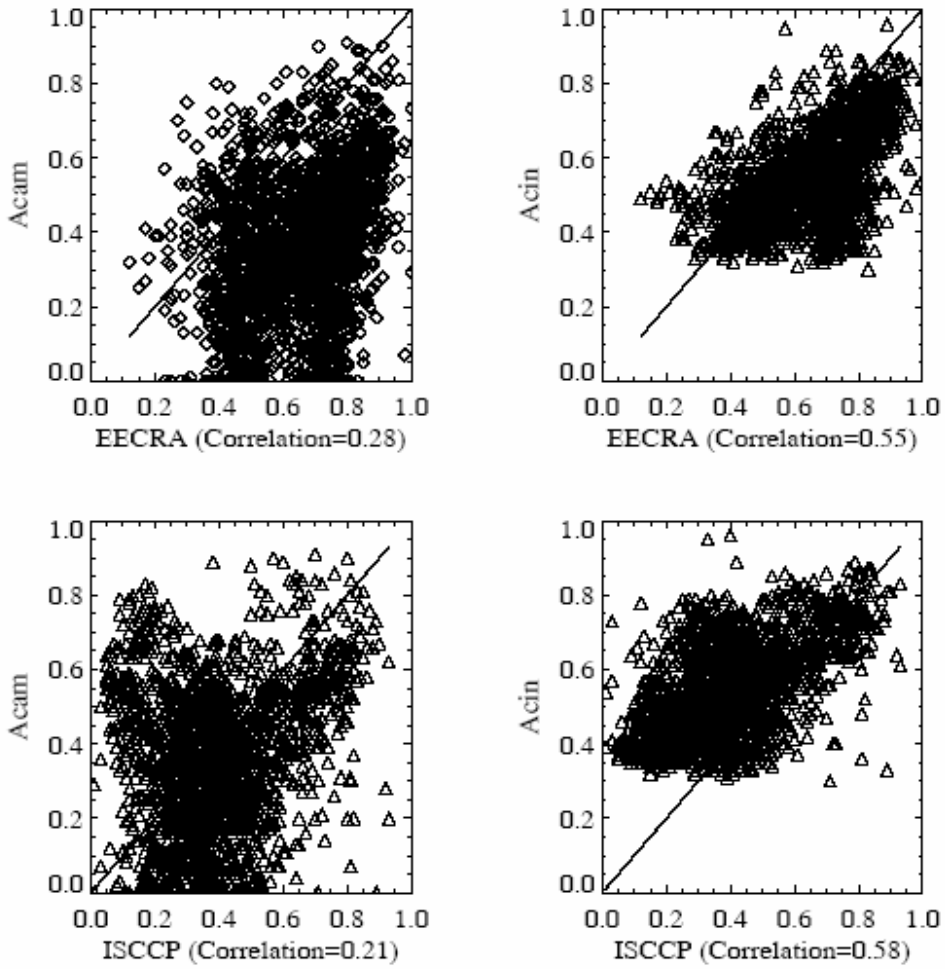


**Figure 4.3**: The seasonal averaged low cloud amounts from the EECRA, the ISCCP D-series, and the simulation results using the KH scheme $A_{CAM}$ and the ATIN index $A_{CIN}$ in the eight study regions at the $2.5^{\circ} \times 2.5^{\circ}$ horizontal resolution. The upper left panel is $A_{CAM}$ against EECRA low cloud cover, the upper right panel is $A_{CIN}$ plotted against the EECRA low cloud amount; the lower left panel is $A_{CAM}$ plotted against the ISCCP low cloud amount, and the lower right panel is $A_{CIN}$ plotted against the ISCCP low cloud cover.

The most significant improvement is in China as evidenced in Table 4.3. Table 4.3 is the calculated correlations between observed and simulated seasonal low cloud fractions using $\Delta\theta_{700}$ and ATIN predictors in the eight regions during the period from 1985 to 1997. The EECRA dataset has the most complete cloud records in China for low stratiform region. Lower troposphere stability $\Delta\theta_{700}$ is positively correlated with grid-averaged EECRA low stratiform cloud amount, but it is negatively correlated with grid-averaged ISCCP low stratiform cloud amount. Compared with $\Delta\theta_{700}$, ATIN has large positive correlations with both EECRA and ISCCP grid-averaged low stratiform cloud amounts. It also simulates better seasonal low stratiform cloud amounts near the Peruvian, North Pacific, and North Atlantic regions, and has similar prediction skills in the other four regions. Based on the experiments not shown here, the cloud cover scheme developed in Chapter 2 simulates better spatial distribution of marine low cloud amount than both ATIN index and lower troposphere stability.

**Table4.3** Correlations between observed and scheme simulated seasonal low cloud fraction in eight regions at d $2.5^\circ \times 2.5^\circ$ horizontal resolutions during the period from 1985 to 1997.

| | EECRA-KH | EECRA-ATIN | ISCCP-KH | ISCCP-ATIN | EECRA-ISCCP |
|---|---|---|---|---|---|
| Peruvian | 0.69 | 0.78 | 0.67 | 0.78 | 0.77 |
| Namibian | 0.89 | 0.86 | 0.84 | 0.81 | 0.91 |
| California | 0.62 | 0.55 | 0.56 | 0.50 | 0.60 |
| Canarian | 0.07 | 0.06 | 0.40 | 0.33 | 0.31 |
| China | 0.44 | 0.69 | -0.12 | 0.56 | 0.54 |
| Australian | 0.28 | 0.21 | 0.25 | 0.22 | 0.56 |
| North Pacific | 0.76 | 0.81 | -0.20 | -0.17 | -0.14 |
| North Atlanta | 0.43 | 0.49 | 0.15 | 0.34 | 0.08 |

## 4.4 Correlations between Low Cloud Synoptic Variations and Various Large Scale Environment Predictors

Table 4.4 lists correlations between observed grid-averaged ISCCP low cloud cover and various daily parameters on synoptic time scales in four regions at $2.5^\circ \times 2.5^\circ$ horizontal resolutions during the period from 1985 to 1997. Monthly means are removed from the original ISCCP low cloud cover data. Large scale predictors include the lower troposphere stability $\Delta\theta_{700}$, the gross dry thermal stability ATIN, the vertical transport of ADIN ($Dynz$), the horizontal transport of environmental temperature ($Dyn\_env$), the horizontal transport of parcel temperature ($Dyn\_pal$), the total dynamical transport of ADIN ($Dyn\_tot = Dynz + Dyn\_env - Dyn\_pal$), THE ERA40

surface evaporation $F_{LH}$, the ISCCP D-series ocean surface $T_S$, the ERA40 vertical subsidence rate $W_{850}$, and the new cloud cover scheme developed in Chapter 3 ($A_{oc}$).The new cloud cover scheme is slightly modified as following to better represent synoptic variations of low stratiform cloud.

$$A_c = [0.3Dyn\_tot + 30) / R_{crf}^0 \quad \text{(Peruvian)} \tag{4.6}$$

$$A_c = [0.3Dyn\_tot + 0.3F_{LH}) / R_{crf}^0 \text{ (Namibian and Canarian)} \tag{4.7}$$

$$A_c = [0.3(Dynz - Dyn\_pal) + 0.3F_{LH}) / R_{crf}^0 \text{ (Californian)} \tag{4.8}$$

The modified new cloud cover scheme $A_{oc}$ based ADIN dynamical transport and surface evaporation better explains synoptic variations of ISCCP marine low clouds than $\Delta\theta_{700}$ and ATIN in all four MSC regions. Among various predictors listed in Table 4.3, the total dynamical transport of ADIN ($Dynz$) is the best predictor for Peruvian region and the horizontal transport of parcel temperature ($Dyn\_pal$) is the best predictor near the Namibian region, the California region, and the Canarian region. Surface latent heat flux is a good predictor in all MSC regions except the Peruvian region. Surface latent heat is determined by ocean SST and surface wind speed. As shown in Table 4.3, SST is not a good predictor in all MSC regions. The good correlation between surface evaporation and low cloud amount variations is due to surface wind speed perturbations on synoptic timescales. As evidenced in Table 4.4, no single predictor has a correlation more than 0.25 with observed grid-averaged synoptic variations of ISCCP low cloud amount.

**Table 4.4**: Correlations between observed ISCCP low cloud cover and various daily parameters on synoptic time scale in four MSC regions at $2.5^\circ \times 2.5^\circ$ horizontal resolutions during the period from 1985 to 1997.

| | Peruvian | Namibian | California | Canarian |
|---|---|---|---|---|
| $\Delta\theta_{700}$ | 0.07 | 0.07 | 0.09 | 0.09 |
| $A_{oc}$ | 0.21 | 0.11 | 0.12 | 0.17 |
| *ATIN* | 0.03 | 0.06 | 0.04 | 0.04 |
| *Dynz* | -0.08 | -0.05 | 0.12 | 0.01 |
| *Dyn_env* | 0.12 | -0.00 | -0.13 | -0.05 |
| *Dyn_pal* | -0.06 | -0.12 | -0.23 | -0.20 |
| *Dyn_tot* | 0.18 | 0.08 | 0.10 | 0.15 |
| $F_{LH}$ | 0.01 | 0.10 | 0.20 | 0.18 |
| $T_s$ | -0.02 | 0.00 | -0.03 | -0.02 |
| $W_{850}$ | -0.11 | -0.06 | 0.12 | 0.01 |

## 4.5 Conclusions

A single predictor based on lower troposphere thermal inhibition energy ATIN is shown to be more skillful than lower troposphere stability in simulating monthly and seasonal grid averaged low stratiform clouds from both EECRA ship observations and ISCCP satellite observations. It greatly improved the low stratiform cloud amount simulations in the China region where EECRA has the most complete cloud record. ATIN is also found to have a better relationship with low stratiform clouds near the Peruvian region, North Atlantic region, and North Pacific region. Correlation analysis between low cloud cover and various environmental predictors suggests that the dynamical transport of gross dry static stability is more closely related to synoptic

variations of grid ISCCP low cloud amount than ocean surface SST, ATIN, $\Delta\theta_{700}$, and vertical velocity in four subtropical MSC regions. Surface evaporation related to surface wind speed variation is also a good indicator in three MSC regions. Therefore, the new cloud cover scheme based on both large scale circulation and local stability performs much better than single predictors such as ATIN and $\Delta\theta_{700}$ in simulating synoptic variations. Prediction skills of various low cloud cover schemes will be compared and discussed from daily to inter-annual timescales in all low stratiform cloud regions in a future study.

Dynamical transport of available dry inhibition energy is found to be important on monthly, seasonal, and interannual timescales as shown in Chapter 2 and Chapter 3. It is also better correlated with low cloud amount than most other predictors on synoptical timescale as shown in this chapter. In Chapter 5, dynamical transport of ADIN is used to diagnose marine boundary cloudiness and coupled with simple ocean wind model to investigate the influence of ocean SST, large scale divergence, and marine clouds on both mean states and the probability distribution of surface winds in the southeast Pacific.

# CHAPTER 5

# INFLUENCES OF BOUNDARY LAYER CLOUDS, OCEAN SURFACE TEMPERTAURE, AND LARGE SCALE DIVERGENCE ON LOCAL SURFACE WINDS IN THE SOUTHEAST PACIFIC

## 5.1 Introduction

The beauty of marine stratus and stratocumulus lies in their amazingly complicated spatial structure and rich internal variability which links the slowly varying planetary scale processes with randomly fluctuating turbulence. To study and understand marine boundary clouds is to appreciate their complexity and to synthesize many diverse components into a unified whole. Previous chapters provide various lines of evidence to demonstrate that both large scale circulations and local thermal structures control the seasonal and interannual variations of boundary layer cloudiness in subtropical marine stratus and stratocumulus regions. The key issue to be addressed in this chapter is to understand the influences of marine boundary clouds, ocean SST, and large scale divergence on the stochastic dynamics of local ocean surface winds.

Let’s first try to understand the significance of studying a stochastic dynamical system in climate modeling. Theoretical study of climate systems up to a half century ago can be viewed as the study of differential equations and the modeling of natural phenomena by deterministic solutions of these differential equations. It was commonly thought that given an initial set of conditions, one could be able to predict the future in

certainty. The famous “butterfly” problem studied by Lorenz (1963) revolutionarily changed our views about weather prediction and brought the concept of “chaos” into study of dynamical systems. Any error in initial conditions is magnified so rapidly that the system will quickly become unpredictable. Thus the climate system is chaotic with limited predictability. Our intuitions also tell us that random processes bring uncertainty into everyday weather and continue to change our climate in past, present, and future. Forecast of extreme weather and their nonlinear dynamics become the central tasks facing the current weather forecast and climate modeling community. In such a stochastic system, the probability density function (PDF) is necessary to measure the likelihood of observing a particular value. It can improve the estimation of nonlinear variables such as surface evaporation and surface sensible heat flux when only grid-averaged mean values are provided in climate models. Quantification of the PDF of any variable requires typically its mean value and its higher moments such as standard deviation and skewness.

Satellite observations have revolutionized our ability to gather high resolution ocean surface winds and cloud cover information globally. The SeaWinds instrument abroad the Quik Scatterometer (NSCAT) satellite was launched in 1999 and has generated daily ocean surface winds at $0.25^\circ \times 0.25^\circ$ resolution since then. The Atmospheric InfraRed Sounder (AIRS) satellite was launched in 2002 and has generated cloud cover, cloud liquid water path, and 3-D temperature profiles at $1^\circ \times 1^\circ$ horizontal resolutions for three years. These high resolution continuous satellite datasets provide remarkable opportunities to study the relationship of ocean surface wind probability distributions with ocean surface SST, large scale circulation, and marine boundary clouds.

The ocean surface wind PDF is crucial for simulating realistic ocean surface evaporation, boundary layer turbulence, local wind power, and chemical transports. A number of studies have been made about the parameterization of wind PDFs using surface wind speed (Thompson et al., 1983; Isemer and Hasse, 1991; Petersen et al., 1998; Wanninkhof et al., 2002; Monahan, 2005, 2006). No previous work has addressed how interactions of ocean surface SST, large scale divergence, and marine boundary clouds affect the ocean surface wind probability distributions.

Surface wind anomalies are determined by surface pressure gradient anomalies. Previous work suggested that a diabatic heating anomaly determines the surface pressure anomaly (Gill, 1980; Lindzen and Nigam, 1987). Diabatic heating by solar heating in convective regions leads to lower troposphere temperature anomaly. However, in the non-convective regions, the surface pressure anomaly is determined by both surface temperature perturbations and boundary layer height perturbation. Both ocean surface SST and large scale divergence affect surface pressure gradient and marine cloud formation. Influences of large scale circulation and the underlying ocean surface have been studied to explain the existences of MSC in the subtropical regions (see Chapter 2 and 3; Rozendall and Rossow 2003; Xu, Xie and Wang 2005). A previous diagnostic study of Nigam et al. (1997) suggested a positive feedback between surface wind, marine boundary clouds, and surface flux in the southeast Pacific regions. However, no theory has been proposed to explain this local positive feedback.

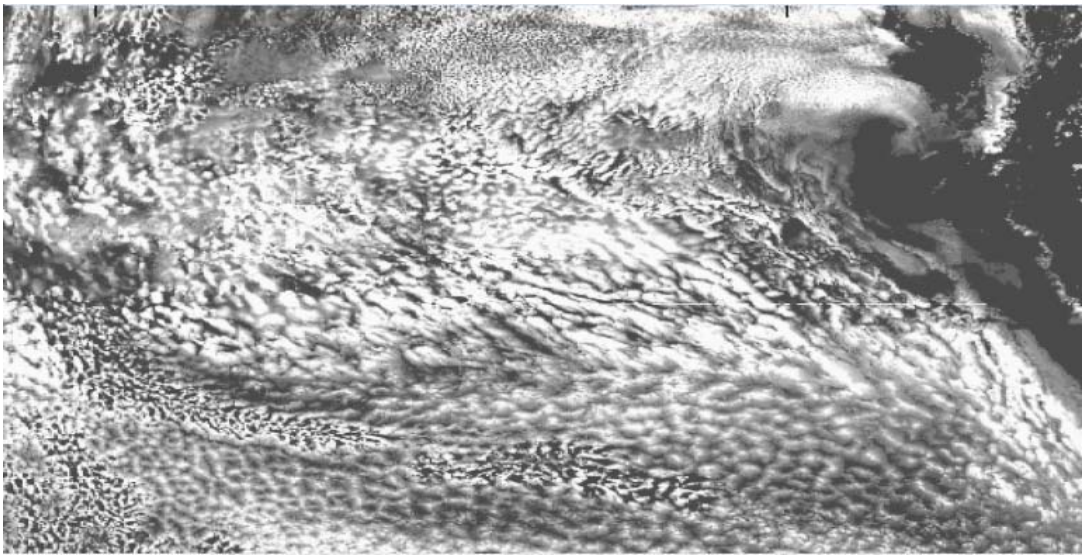

**Figure 5.1** MODIS cloud liquid water path at 1km horizontal resolution near the Peruvian regions at the 246$^{th}$ day 16:20PM in 2000.

Marine boundary clouds display rich variability in various space and time scales. Figure1 is a snapshot of MODIS cloud liquid water path at 1 km horizontal resolution near the Peruvian regions at the 246$^{th}$ day, 2000. It is shown in Fig.1 that boundary layer clouds have different mesoscale structures and cover extensively the south east Pacific. The importance of mesoscale cellular convection on the spatial variability of liquid water paths has been studied in the south east Pacific (Wood and Hartmann 2006b). They found that LWP spatial variance is sensitive to horizontal scales of 10-50 km, not the large scale meteorological conditions, suggesting internal boundary layer processes are important for determining the mesoscale cellular type clouds. The most recent study of Stevens, Zhang, and Ghil (2006) found that the climate bias in representing MSC in the ERA40 can be improved when random processes are included in the system.

The main objective of this chapter is to study the influence of ocean surface SST, large scale divergence, and marine boundary cloud variations on local ocean surface wind probability distributions. In the southeast Pacific, both ocean surface SST and marine boundary layer height have large horizontal gradients which determine the ocean surface pressure gradients in the marine stratus and stratocumulus regions. Marine boundary layer are strongly influenced by boundary layer cloud internal variations, and horizontal momentum transport due to tropics wave and middle latitude synoptic systems, which are simplified as slowly varying random forces working on marine boundary layer. The near surface wind is quickly adjusted to its equilibrium solution through turbulence mixing. A simple deterministic model and a stochastic perturbed model are developed to understand and explain the influence of SST, large scale divergence, and boundary layer clouds on the mean states and the probability distribution of local surface wind speed. When ocean surface SST is cold, stronger dynamical transport of available dry inhibition energy and larger surface evaporation enhance cloud top entrainment, deepen the marine boundary layer, increased the low cloud amount, and strengthen surface wind speeds. ERA40 monthly mean surface wind speeds are found to be increased when SST is colder and more marine low clouds are developed in the subtropical southeast Pacific. Non-seasonal QuikSCAT surface wind standard deviation has a positive relationship with non-seasonal local surface wind speed. Multiple equilibriums exist in the relationship between the surface wind standard deviation and ocean surface SST. Multiple equilibriums of boundary layer thermal structures were studied in the theoretical work of Stevens, Zhang, and Ghil (2006). This study is the first work to show the existence of multiple equilibriums in moments of surface wind based on both observations and simple model

simulations. The surface wind skewness, a measure of extreme wind, decreases with wind speed due to surface friction in a large wind regime. However, increases with wind speed in buoyancy controlled small wind regimes. Results from both observations and model studies indicate that both large scale conditions and boundary layer internal process are necessary to simulate the ocean surface wind probability distributions.

The approach in this chapter is to investigate local relationships between boundary layer cloudiness and surface wind variability by combining both satellite observations with a conceptual model study. The satellite data used are described in section 5.2; a highly simple deterministic model is developed to explain the QUIKSCAT and ERA40 observed mean state relationship in section 5.3. Implications of marine boundary layer clouds for basic tropical dynamics are briefly discussed based on the linearized 2D version of the deterministic model; Random perturbations are added to surface wind momentum equations and the boundary layer height equation to simulate and explain the satellite observed surface wind probability distribution and its relationship with mean wind speed and ocean surface SST in section 5.4; the influence of various factors on the relationship between moments and local mean surface wind speed is addressed in section 5.5; the influence of various factors on local surface wind moments and SST relationship are studied in section 5.6; the physical pictures are summarized and future improvements are discussed in the final section.

## 5.2 Satellite Data Descriptions

The mean state and probability distributions of surface winds and their relationships with ocean surface SST and surface wind speed are studied using the AIRS ocean surface

SST dataset and the QuikSCAT surface wind dataset. The sea surface wind dataset consists of Level 3.0 gridded daily SeaWinds scatterometer 10m zonal and meridional wind observations from the NASA QuikSCAT satellite (Jet Propulsion Laboratory, 2001), available on a $0.25^\circ$ x $0.25^\circ$ grid from March, 2003 to February, 2006. The dataset is first averaged into $1^\circ$ x $1^\circ$ grid resolution for the same time period. Because rainfall can lead to errors in estimating sea surface winds, the data points with observed rainfall are excluded from the present analysis. The cloud cover dataset consists of the Level 3.0 Gridded Retrieval Product from the NASA AIRS satellite (http://disc.gsfc.nasa.gov/AIRS), available on an $1^\circ$ x $1^\circ$ horizontal resolution from March 2003 to February 2006, the same period as that of the QUIKSCAT surface wind dataset.

In section 5.3, the time series of QuikSCAT surface wind dataset and AIR's cloud cover and SST dataset are studied during the period from March 2003 to February 2006 in the southeast Pacific $(100W-80W, 30S-10S)$. The three-year averaged mean surface wind and its relationship with three-year averaged SST and are studied using a simple 1D deterministic model. In section 5.4, the three-year averaged seasonal cycle is removed from the original QuikSCAT data. The resulting surface wind time series is further processed to get its mean value, standard deviation, and skewness of non-seasonal surface wind speed at $1^\circ \times 1^\circ$ horizontal resolution.

## 5.3 A Simple Deterministic Model for Mean States

### 5.3.1 The Model Development

The eddy-averaged horizontal momentum equations and Lilly's simple mixing layer model are combined to represent ocean surface wind and marine boundary layer.

$$\partial_t U - fV = -\rho^{-1}\partial_x P_s - \partial_z\left(\overline{w'u'}\right) \tag{5.1}$$

$$\partial_t V + fU = -\rho^{-1}\partial_y P_s - \partial_z\left(\overline{w'v'}\right) \tag{5.2}$$

$$\partial_t h = w_e - D_{zi} h \tag{5.3}$$

In equation (5.1) to (5.3), $U$ represents the near surface zonal wind, $V$ represents the near surface meridional wind, $\overline{w'u'}$ and $\overline{w'v'}$ are surface wind stress for zonal wind and meridional wind, $D_{zi}$ represents divergence at the boundary layer top, $f$ is the Coriolis parameter, $h$ is the boundary layer height, $w_e$ is the entrainment rate, $\rho$ is the air density, $P_s$ is the surface air pressure, $\theta$ is the boundary layer potential temperature, $q$ is the boundary layer specific humidity, $q_s$ is the saturated specific humidity, $T_s$ is the ocean surface temperature, $C_h$ and $C_e$ are surface heat and moisture transfer coefficient respectively, $P$ is precipitation, $\beta$ is local efficient of precipitation. Horizontal and vertical advection terms are not considered in the model.

*5.3.1.1 Formulating the near surface pressure perturbations*

The lower troposphere is characterized by a two layer structure shown in Figure5.2 with a cold moist boundary layer topped by a warm and dry free atmosphere below the trade wind inversion at $Z_T$. The boundary layer cloud occurs near the boundary layer top beneath a strong temperature inversion. The air density in the boundary layer is $\rho_{Bl}$ and

the air density in the free atmosphere is $\rho_{free}$. The surface pressure $P_s$ is determined by the air pressure at the trade wind inversion $P_T$ and the air density in the lower troposphere.

$$P_s = P_T + \int_0^{Z_T} \rho g dz = P_T + g\int_0^{h} \rho_{BL} dz + g\int_h^{Z_T} \rho_{free} dz \tag{5.4}$$

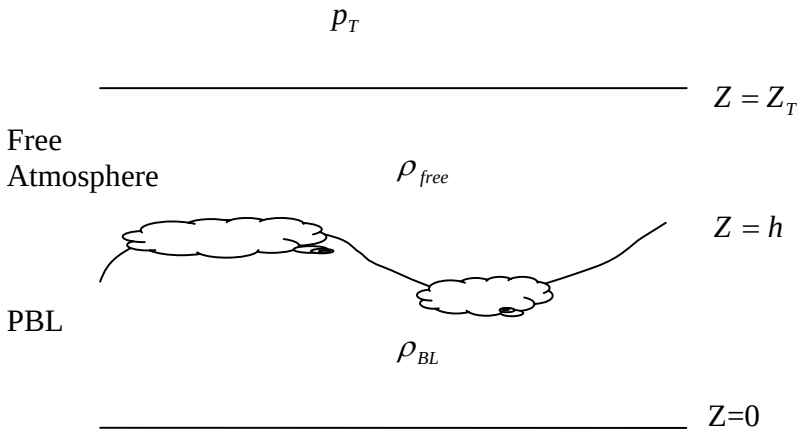


**Fig.5.2 Carton of a two-layer structure within lower troposphere**

In equation (5.8), $\rho_{BL}$ and $\rho_{free}$ represent air density within boundary layer and free atmosphere respectively, and $P_T$ is air pressure at trade wind inversion. The air density perturbation is proportional to potential temperature perturbation. The surface air pressure can be formulated as function of boundary layer height and potential temperature difference between free atmosphere and ocean surface.

$$P_S = P_T + g\overline{\rho}_{free} Z_T + g\rho_0 \frac{\Delta\theta}{\theta_0} h \tag{5.5}$$

In equation (5.9), $\Delta\theta = \overline{\theta}_{free} - \overline{\theta}_{BL} \approx \theta_{Z_t} - \theta_{srf}$ is the potential temperature difference between trade wind inversion and ocean surface. The pressure and height gradients at the

trade wind inversion are assumed to vanish; therefore the surface pressure gradient is determined by both the boundary layer height variation and lower troposphere stability gradient.

$$\nabla P_s \approx g\frac{\overline{\Delta\theta}}{\theta_0}\nabla h + \frac{gh}{\overline{\theta}_2}\nabla(\Delta\theta) \tag{5.6}$$

In the highly simplified case, it is assumed the amplitude of horizontal gradient of boundary layer height is proportional to the boundary layer height. From ERA40 reanalysis, $\Delta\theta$ increases toward the coastal region, and decreases from south toward equator due to the distribution of SSTs. The boundary layer height decreases toward coastal region and toward the equator. The west-east gradient of $\Delta\theta$ weakens $\nabla_x P_s$; while the boundary layer height variation enhances $\nabla_x P_s$ and dominates the west-east surface pressure term. South-north gradients of both $\Delta\theta$ and boundary layer height contribute to negative $\nabla_y P_s$. Based on ERA40 results near the Peruvian region, in this simple model, the mean surface pressure gradient is determined primarily by boundary layer height, the gradient of the temperature inversion strength is given a constant value.

$$\nabla_x P_s \approx g(\Delta\theta / L_x)h/\theta_0 \approx g(-1.35K/100KM)h/\theta_0 = a_u\,\Delta\theta\,h \tag{5.7}$$

$$\nabla_y P_s \approx g(\Delta\theta / L_y)h/\theta_0 \approx g(-1.01K/100KM)h/\theta_0 = a_v\,\Delta\theta\,h \tag{5.8}$$

*5.3.1.2 Surface wind stress*

Traditionally, surface wind stress is parameterized based on surface wind speed $V_s$ and the drag coefficient $C_d$ based on following formulas:

$$\overline{w'u'}^0 \approx C_d V_s U \tag{5.9}$$

$$\overline{w'v'}^{0} \approx C_d V_s V \tag{5.10}$$

A typical value for $C_d$ is $1.18\times10^{-3}$ for wind speed less than $10 m/s$ over the tropical ocean. The vertical shear of ocean wind stress is obtained by vertically integrated from the surface $z=0$ to the mixed layer top $z=H_0$.

$$\partial_z \overline{w'x'} = \int_0^{H_0} (\partial_z \overline{w'x'}) dz = (\overline{w'x'}^{0}) / H_0 \tag{5.11}$$

In equation (5.11), $H_0$ is the mixing layer depth which is taken to be 500 m in this highly simple study.

*5.3.1.3 Parameterization of entrainment rate due to buoyant driven*

Following Lilly's entrainment idea (1968), the entrainment heating is partially balanced by cloud top radiative cooling near the inversion layer.

$$c_p \rho\ w_e \Delta^{+}\theta = \ \gamma\ C_f F_{crf}^{0} \tag{5.12}$$

In equation (5.12), $\gamma \in [0,1]$ is the ratio of cloud top radiative cooling to balance entrainment heating and $C_f$ is the low cloud fraction. From ISCCP FD observation presented in Chapter 3, unit area cloud top radiative cooling is $F_{crf}^{0} = 70\ Wm^{-2}$. As in Lilly's model, the temperature inversion strength near the boundary top is linearly determined by lower troposphere stability $\theta_{Z_T} - T_s$ and boundary layer height.

$$\Delta^{+}\theta = (\theta_{Z_T} - T_s) h / Z_T \tag{5.13}$$

*5.3.1.4 Formulating Boundary Layer Cloudiness*

From the equation (2.30) in Chapter 2, cloud top radiative cooling is balanced by dynamical transport of lower troposphere available dry inhibition energy ADIN.

$$\varepsilon A_{dyn}(ADIN) + \beta F_{LH} - C_f F_{crf}^0 \approx 0 \tag{5.14}$$

$$A_{dyn}(ADIN) = \rho c_p [-W_h(\theta_{Z_T} - T_s) + \int_0^{Z_T} (U\partial_x + V\partial_y)(\theta_{env} - \theta_{pal})dz] \tag{5.15}$$

Surface latent heat flux $F_{LH}$ is determined by surface wind speed, ocean surface SST, and near surface relative humidity. Based on bulk formula and equation (2.36) in the chapter 2, surface evaporation is formulated as

$$F_{LH} = L_v C_e V_s (q_s - q_a) = L_v C_e V_s \Delta q_0 (1 - \Delta\theta / \Delta\theta_{\max}) \tag{5.16}$$

It is reasonable to set the maximum inversion strength $\Delta\theta_{\max}$ as a constant of 35K based on the fact that the observed relationship between lower troposphere stability and near surface relative humidity as evidenced in Figure2.6 is close to linear in the southeast Pacific. The empirical coefficient of humidity difference is $\Delta q_0 = 8 \times 10^{-3} Kg/Kg$, the heat transfer coefficient is $C_e = 3 \times 10^{-3}$. From ERA40 reanalysis, large scale divergence is relatively unchanged near the surface. Therefore, large scale vertical velocity at boundary layer top is a function of large scale divergence and boundary layer height.

$$W_{Z_i} = -D_{Zi} h \tag{5.17}$$

Horizontal transport of ADIN is assumed to depend mainly on near surface winds.

$$\int_0^{Z_T} (U\partial_x + V\partial_y)(\theta_{env} - \theta_{pal})dz] \approx t_u U + t_v V \tag{5.18}$$

$$t_u = \int_0^{Z_T} \partial_x (\theta_{env} - \theta_{pal})dz, \quad t_v = \int_0^{Z_T} \partial_y (\theta_{env} - \theta_{pal})dz \tag{5.19}$$

In the model simulations, $t_u$ and $t_v$ are given values of $2.5\times10^{-3} Km/s$ and $-2.5\times10^{-3} Km/s$ respectively based on climatology of south east Pacific. Combining equations (5.14)-(5.19), low cloud fraction $C_f$ is formulated as the function of large scale divergence, ocean surface SST, boundary layer height, and near surface winds.

$$0.3c_p[-D_{zi}h(\theta_{700}-T_s)-t_uU-t_vV]+a_cV_s\Delta q[1-(\theta_{Z_T}-T_s)/\Delta\theta_{\max}]=C_fF_{crf}^0 \quad (5.20)$$

$$a_c=\beta L_vC_e \quad (5.21)$$

The 1D model after parameterizations is written as

$$\partial_tU = a_u(\theta_{Z_T}-T_s)h + fV - C_dV_sU/h_0 \quad (5.22)$$

$$\partial_tV = a_v(\theta_{Z_T}-T_s)h - fU - C_dV_sV/h_0 \quad (5.23)$$

$$\partial_th = \gamma C_fF_{crf}^0Z_T/(h(\theta_{Z_T}-T_s)) - D_{zi}h \quad (5.24)$$

$$C_fF_{crf}^0=0.3c_p[D_{zi}h(\theta_{Z_T}-T_s)-t_uU-t_vV]+a_cV_s\Delta q_0[1-(\theta_{Z_T}-T_s)/\Delta\theta_{\max}] \quad (5.25)$$

Prescribed model forcings are large scale divergence at cloud top $D_{Z_i}$ and ocean surface SST. Potential temperature at trade wind inversion $\theta_{Z_T}$ is given its climatology value of 312 K near the Peruvian region.

### 5.3.2 Observed and Model Simulated Local Relationships

*5.3.2.1. Relationship between mean surface winds and marine low cloud fractions*

In Figure5.3, equilibrium solutions of surface easterly wind, southerly wind, surface wind speed, and boundary layer height are shown as functions of marine low cloud fraction. In the model simulation run, ocean surface SST is linearly changed from 16K to 26 K, large scale divergence varies independently from zero to $6\times10^{-6}/s$, and the

entrainment ratio $\gamma = 0.5$. Figure 5.3 illustrates the fact that, in the subsiding branch of the tropical large scale circulation, strong large scale subsidence and cold ocean surface SST lead to great amount of dry static energy transported from free atmosphere into boundary layer. More marine low clouds are developed to adjust local thermal structure toward a preferred mean state such that the lower troposphere available potential temperature is well kept. When marine cloud fraction is increased, strong cloud top radiative cooling deepens the cloud-topped boundary layer and enhances ocean surface pressure gradients. As a result, the surface southerly winds become stronger. The increased surface wind speed further deepens the mixing layer depth through larger surface flux and increases the horizontal transport of ADIN, resulting in even more marine low clouds.

This highly simplified physical picture is supported by previous simple model studies (Larson and Hartmann, 1999) and a diagnostic climate modeling study (Nigam et al, 1997). The model simulated relationship between mean surface wind and mean cloud fraction agrees well with both satellite observations and ERA40 reanalysis data in the south east Pacific. Figure5.4 shows three-year mean values of QuikSCAT surface wind speed plotted against mean AIRS cloud cover for each $1^\circ \times 1^\circ$ region in south east Pacific (25S-10S, 100W-80W). The three year mean value is averaged from Mar. 2003 to Feb. 2006. Cloud fraction increase is related to three-year mean surface southerly wind increase. The surface wind speed is moderately increased with cloud fraction in the south east Pacific.

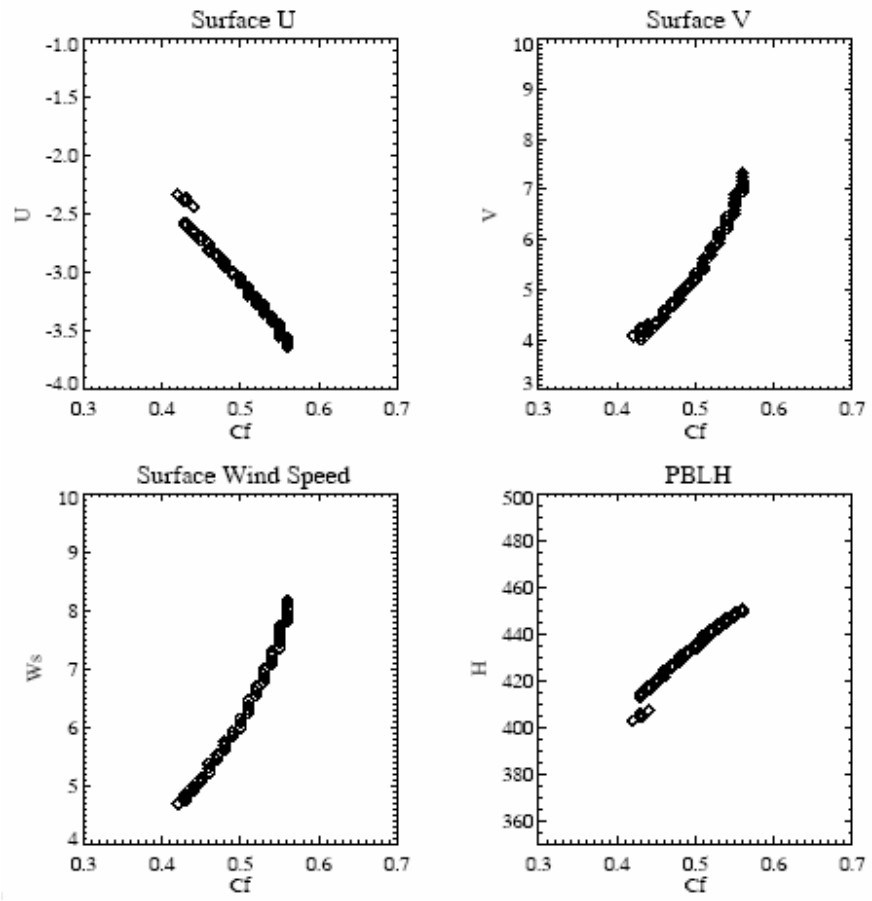


**Figure 5.3** Model simulated equilibrium surface wind and boundary layer height as function of marine cloud amount. Large scale divergence is set to $5\times10^{-6}/s$.

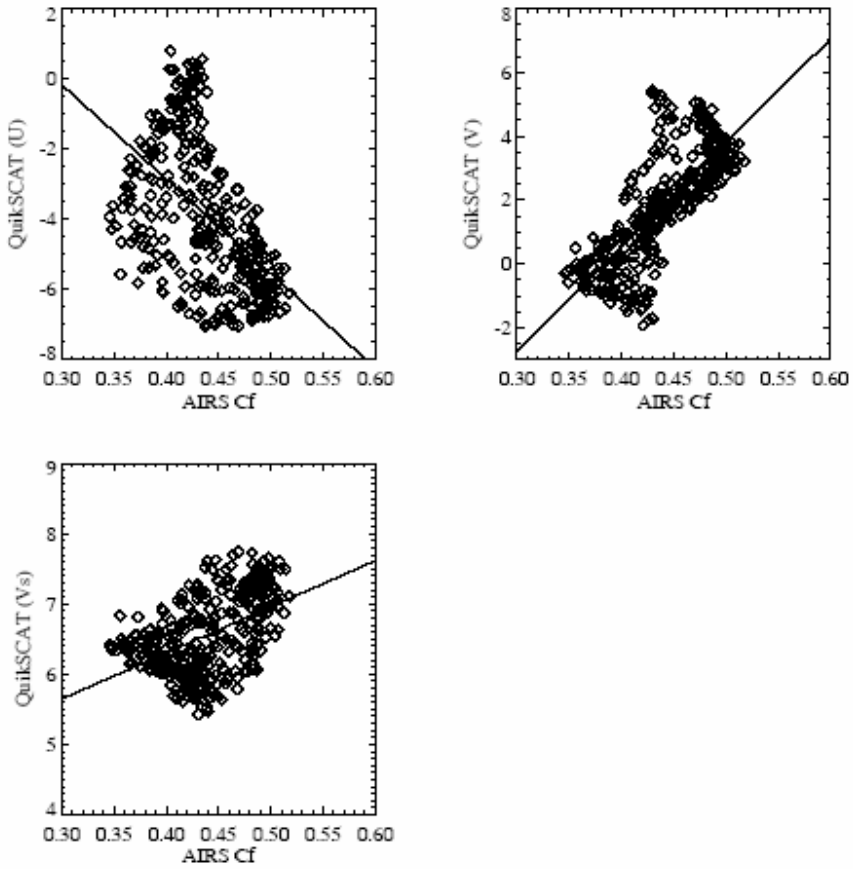


**Figure 5.4** Three-year averaged QUIKSCAT surface wind speed plotted against mean AIRS cloud cover using $1^{\circ} \times 1^{\circ}$ grid value in the south east Pacific $(30S - 10S, 100W - 80W)$. The three year mean value is averaged from Mar. 2003 to Feb. 2006.

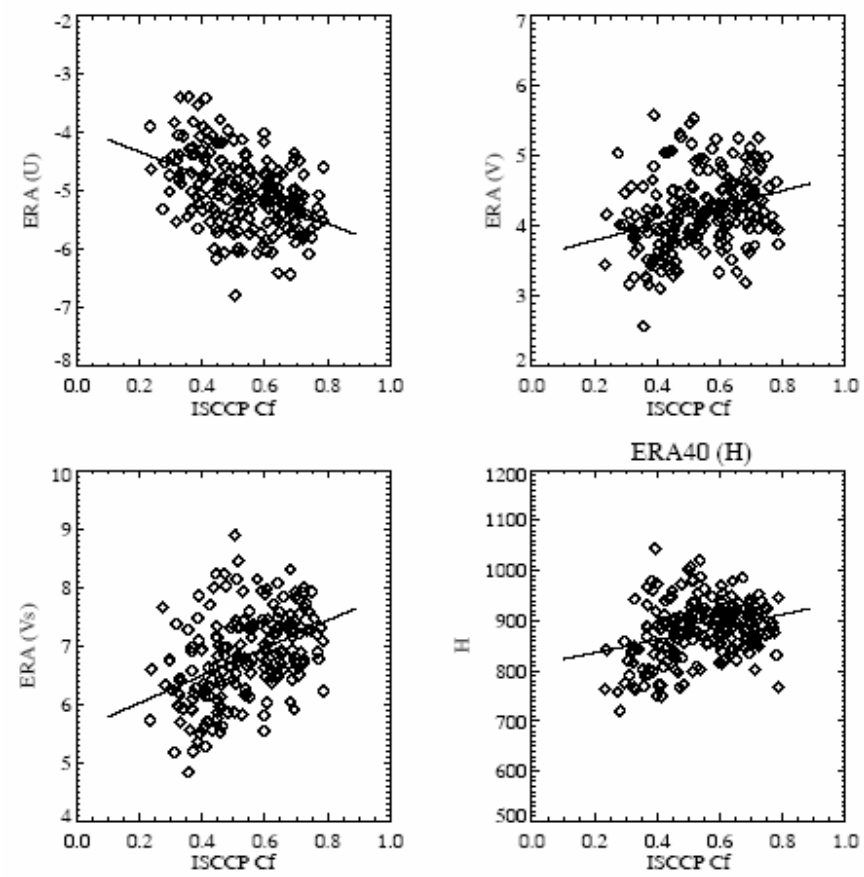


**Figure 5.5** Area-averaged (a) ERA40 monthly mean zonal wind (upper left), (b) ERA40 monthly mean meridional wind (upper right), (c) ERA40 monthly mean surface wind speed (lower left), and (d) ERA40 monthly mean boundary layer height (lower right) plotted against ISCCP D-series monthly mean low cloud amount near the Peruvian region during the period from 1985 to 2000.

This positive relationship is also found between area-averaged ISCCP D-series monthly low cloud fraction and area-averaged monthly mean ERA40 ocean surface wind and boundary layer height near the Peruvian region during the period from 1985 to 2000 as shown in Figure5.5.

*5.3.2.2 Relationships among mean surface wind, mixing layer depth, and ocean surface SST*

Fig.5.6 is the model simulated equilibrium surface winds and boundary layer height as function of ocean surface SST. When ocean surface SST becomes colder, cloud top temperature inversion is strengthened and larger amounts of available dry inhibition energy are transported into boundary layer, resulting in more boundary layer clouds and deepened marine mixing layer. Both stronger temperature inversion and greater boundary layer height enhance ocean surface pressure gradient in marine cloud regions; as a result, the ocean surface winds are also increased. The model describes a negative relationship between ocean surface SST and ocean surface winds, which is supported by the observed relationship between ERA40 monthly mean ocean surface wind and monthly mean ISCCP D-series ocean surface SST at $2.5^{\circ} \times 2.5^{\circ}$ horizontal resolutions in the south east Pacific as shown in Figure5.7.

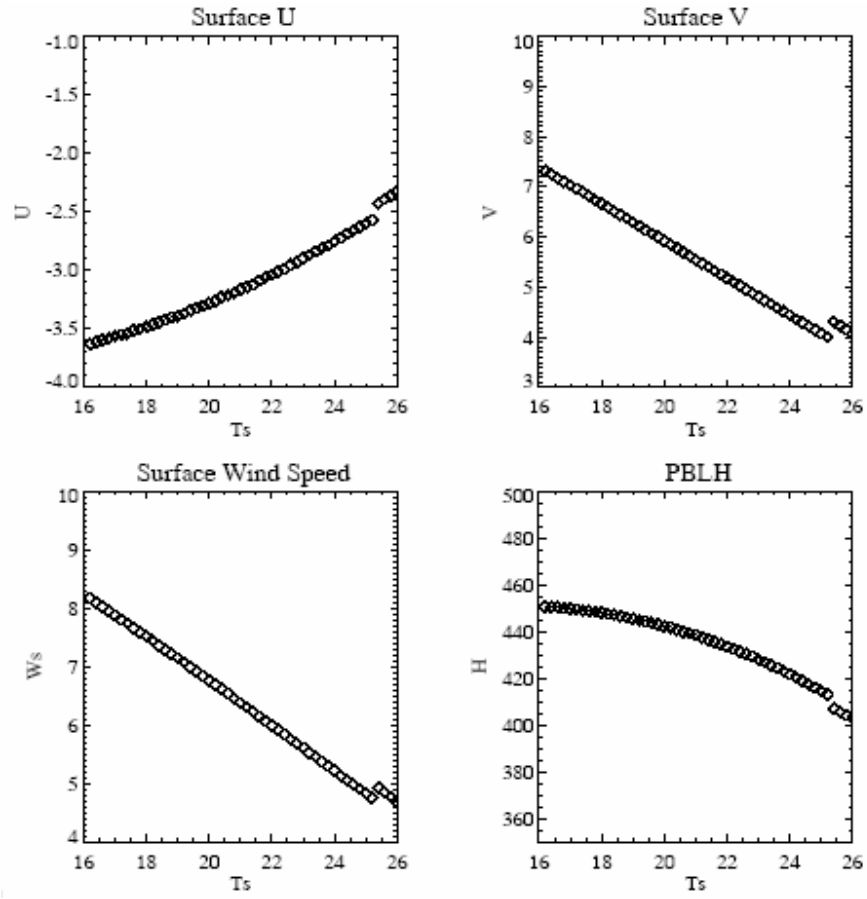


**Figure 5.6** Model simulated equilibrium surface wind and boundary layer height as function of ocean surface SST. Large scale divergence is set to $5\times10^{-6}/s$.

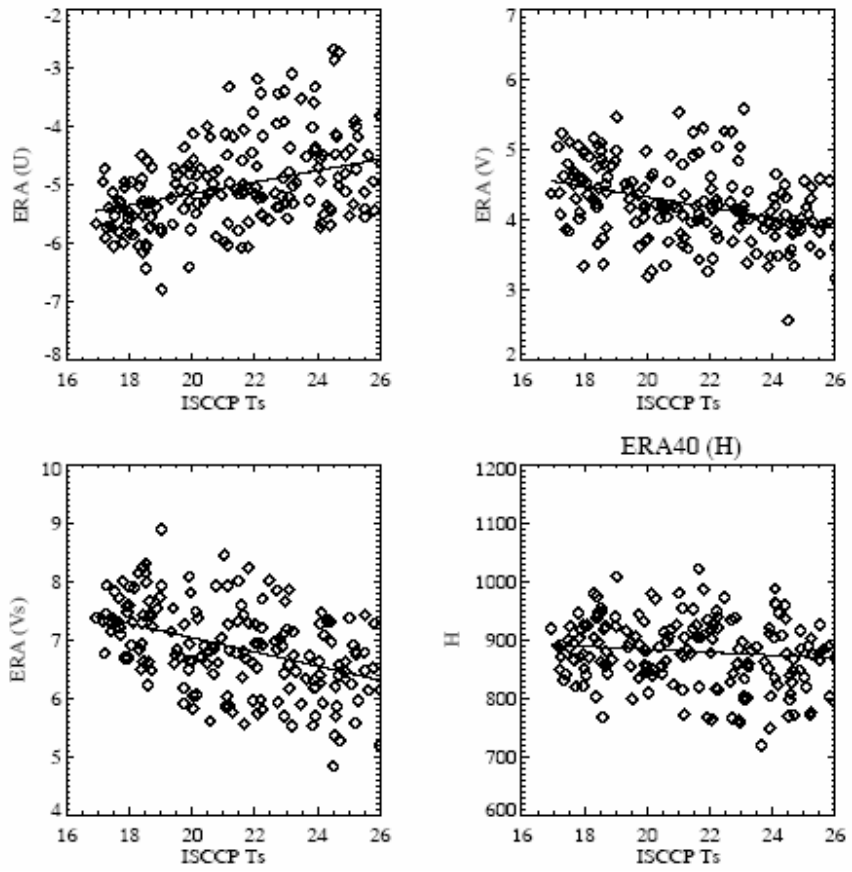


**Figure 5.7** Area-averaged (a) ERA40 monthly mean zonal wind (upper left), (b) ERA40 monthly mean meridional wind (upper right), (c) ERA40 monthly mean surface wind speed (lower left), and (d) ERA40 monthly mean boundary layer height (lower right) plotted against ISCCP D-series monthly ocean surface SST near the Peruvian region during the period from 1985 to 2000.

### 5.3.3 Implications for Basic Tropical Dynamics from the Linearized 2D Model Compared with Gill's Model

Previous studies have linked surface pressure gradient to temperature gradient, which can exist only in boundary layer due to friction. In the lower troposphere, the temperature gradient is quite small, but the boundary layer height gradient is large in the subsiding branch of Walker/Hadley circulation. Mixing layer depth variations are determined by local SST, large scale divergence, and marine boundary layer clouds. The boundary layer model developed in Section 5.3.1 can be re-written in a 2D format following Gill's model.

$$\partial_t U = A_1 \partial_x ((\theta_{Z_T} - T_s)H) + fV - C_d V_s U / H_0 \tag{5.26}$$

$$\partial_t V = A_2 \partial_x ((\theta_{Z_T} - T_s)H) - fU - C_d V_s V / H_0 \tag{5.27}$$

$$\partial_t h + (h - B_1 Z_T)(\partial_x U + \partial_y V) = (E - B_3 U - B_4 V)(Z_T / h) \tag{5.28}$$

In equation (5.28), E represents surface evaporation contributions to boundary height variations, which is mainly determined by surface wind speed and surface temperature. Variations of any variable X can be represented by the sum of slowly varying seasonal variations $\overline{X}$ and fast perturbation $X'$.

$$X = \overline{X} + X' \tag{5.29}$$

*5.3.3.1 Stable solutions for the linearized 2D model on the $\beta$ plane*

The steady-state version of the linearized 2D perturbation model is written as

$$\varepsilon U' - \beta y V' = -(g / \theta_0)(\overline{\Delta\theta}\partial_x h' - \bar{h}\partial_x T_s') \tag{5.30}$$

$$\varepsilon V' + \beta y U' = -(g / \theta_0)(\overline{\Delta\theta}\partial_y h' - \bar{h}\partial_y T_s') \tag{5.31}$$

$$(\partial_x \overline{U} + \partial_y \overline{V})h' + (\overline{h} - B_1 Z_T)(\partial_x u' + \partial_y v') = (Z_T / \overline{h})[E' - B_3 U' - B_4 V'] \quad (5.32)$$

$$w' = \overline{h}(\partial_x U' + \partial_y V') + (\partial_x \overline{U} + \partial_y \overline{V})h' \quad (5.33)$$

$$p' = (\rho g \overline{\Delta\theta} / \theta_0)h' \quad (5.34)$$

In equations (5.30)-(5.32) the symbol $\varepsilon = C_d \overline{V_s} / H_0$ and $E'$ represents surface wind anomaly due to surface evaporation anomaly. Influence of ocean surface SST anomaly on ocean surface pressure and near surface circulation has been studied by Lindzen and Nigam (1987) over tropical oceans. In marine stratus and stratocumulus regions, boundary layer height perturbations due to subsidence and surface flux variations play important roles in determining surface pressure perturbations. In Gill's model (1980), diabatic heating effect and surface pressure dissipation due to Rayleigh friction and Newtonian cooling are balanced by surface wind convergence; dissipation coefficient is set to constant. Heat anomaly in the convective west Pacific enhances surface wind convergence anomaly and negative pressure perturbations. As shown in the equation (5.32) of the new model, when SST is warmer in the east Pacific, cloud top radiative cooling become stronger due to enhanced surface evaporation. The resulting enhanced cloud top entrainment as shown on the right side of equation (5.32) is balanced by surface wind divergence anomaly which is shown as the second term on the left side. The first term on the left side in the equation (5.32) represent boundary layer height variations due to mean subsidence. It enhances surface wind divergence anomaly in the ascending branch of the tropical circulation, and weakens surface wind divergence anomaly in the descending branch of the tropical circulation, which may results in the shift of convective center from west Pacific toward east Pacific. Dissipation due to Rayleigh friction and Newtonian cooling become less important in the marine boundary cloud regions. Due to

time limitation, implications of model physics for Walker circulation and ENSO events will be investigated in more details in a future study.

*5.3.3.2 Kelvin wave on the $\beta$* plane

When the zonal wind and the horizontal gradient of ocean SST vanish, the linearized version of the model on the $\beta$ plane becomes

$$\partial_t U' = -(g/\theta_0)\overline{\Delta\theta}\partial_x h' + \beta y V' - \varepsilon U' \tag{5.35}$$

$$(g/\theta_0)\overline{\Delta\theta}\partial_y h' - \beta y U' = 0 \tag{5.36}$$

$$\partial_t h' + (\bar{h} - B_1 Z_T)\partial_x U' = -(\partial_x \bar{U} + \partial_y \bar{V})h' + [E' - B_3 U'](Z_T/\bar{h}) \tag{5.37}$$

The key feature for tropical Kelvin wave in the new model which is different from classical Gill's models comes from the first term on the right side of equation (5.37). It represents cloud radiative cooling related entrainment variations due to large scale divergence. It greatly dampens boundary layer height variations in strong large scale divergence regions but amplifies boundary layer height variations in large scale convergence regions. This implies that tropical Kelvin wave will be amplified in the west Pacific convergence regions and will be quickly dampened out when it is propagated eastward into marine boundary cloud covered east Pacific. The phase speed of Kelvin wave will also be modified by mean boundary layer height and trade wind inversion height as demonstrated in the second term on the left side of equation (5.37).

*5.3.3.3 The Rossby adjustment without friction*

In the following linearized non-friction perturbation model, marine boundary cloud top radiative cooling is determined by vertical transport of available dry inhibition energy and surface evaporation.

$$\partial_t U' = -g(\overline{\Delta\theta}/\theta_0)\partial_x h' + fV' \tag{5.38}$$

$$\partial_t V' = -g(\overline{\Delta\theta}/\theta_0)\partial_y h' - fU' \tag{5.39}$$

$$\partial_t h' + (\bar{h} - B_1 Z_T)(\partial_x U' + \partial_y V') = -(\partial_x \overline{U} + \partial_y \overline{V})h' + E'(Z_T/\bar{h}) \tag{5.40}$$

The method to get the wave equation in the rotating case is to take the divergence of the momentum equations [$\partial/\partial_x$ of equation (5.38) plus $\partial/\partial_y$ of equation (5.39)] and substitute from (5.40) for the horizontal divergence $\partial_x U' + \partial_y V'$. The resulting wave equation is

$$\partial_t^2 h' - c^2 \nabla^2 h' + (\bar{h} - B_1 Z_T) f\varsigma' + (\partial_x \overline{U} + \partial_y \overline{V})\partial_t h' = 0 \tag{5.41}$$

The relative vorticity is defined as $\varsigma' = \partial_x V' - \partial_y U'$. Based on equation (5.41), the phase speed in a non-rotational plane is $c^2 = (\bar{h} - B_1 Z_T) g(\Delta\theta/\theta_0)$. Wave's phase speed is large when marine boundary layer is deep and lower troposphere stability is strong. In a rotational plane, the Rossby radius of deformation is the horizontal scale at which rotation effects become as important as buoyancy effects. From equation (5.41), the Rossby radius is also affected by mixing layer depth. In the new model, large scale divergence has damping effects on waves in both non-rotational fluid and rotational fluid. As a result, potential energy is hard to extract and converted into kinetic energy in the descending branch of tropical circulations. Detailed analysis will be done in a future study.

In summary, previous studies suggested that temperature gradients anomaly due to solar heating and friction generate surface pressure gradient. Convection is quickly developed to adjust tropical atmosphere back into preferred stratify atmosphere. Large scale circulation and gravity waves in the stratify layer prorogate released convective available energy to remote subtropical regions, where marine boundary clouds are developed, energy propagated by tropical waves downscales to turbulence. Turbulence deepens boundary layer and generates large perturbations of mixing layer depth, resulting in large return flow from subtropics to tropics. The good agreements between model simulation and observations on local relationships among ocean SST, marine cloud amounts, and ocean surface winds suggest that this simple model captures the key factors relating marine boundary clouds, ocean surface SST, and large scale divergence to local ocean surface winds, which is used as a foundation to study local surface wind probability distributions in the following sections. Implications of marine boundary clouds for Walker circulation and tropical waves will be studied in details in a future study.

## 5.4 A Stochastically Perturbed Model for Local Surface Wind Probability Distributions

The seasonal variations of ocean surface wind and marine boundary clouds are determined primarily by the seasonal marching of solar heating and underlying ocean surface properties. They can be well described by deterministic climate systems. However, the non-seasonal variations of ocean surface wind and boundary clouds have rich internal fluctuations in both spatial and temporal dimensions. A stochastic dynamical model is more appropriate to describe their non-seasonal fluctuations. In this study,

horizontal momentum transport due to synoptic disturbs and cloud top entrainment perturbation due to cloud internal variations are treated as slowly varying random forces working on a quick adjusted dynamical system.

### 5.4.1 Model descriptions

The model to describe the surface wind anomaly, boundary layer height, and marine cloud anomaly from seasonal variations can be obtained from the deterministic model in equation (5.22)-(5.25). Horizontal transport of eddy and fluctuations of unit area cloud radiative cooling are added as random perturbations in the model.

$$\partial_t U' = a_u(\theta_{700} - T_s)h'/\Delta\theta_0 + fV' + D_{z_i}U' - C_d(\overline{V_s} + V_s')U'/h_0 - \partial_x(\overline{u'u'}) - \partial_y(\overline{u'v'}) \quad (5.41)$$

$$\partial_t V' = a_v(\theta_{700} - T_s)h'/\Delta\theta_0 - fU' + D_{z_i}V' - C_d(\overline{V_s} + V_s')V'/h_0 - \partial_x(\overline{u'v'}) - \partial_y(\overline{v'v'}) \quad (5.42)$$

$$\partial_t h' = \frac{(\gamma F_{crf}^0 C_f' Z_T)}{(\overline{h} + h')(\theta_{Z_T} - T_s)} - D_{zi}h' + c_1 C_f F_{crf}'/h \quad (5.43)$$

$$0.3c_p(D_{z_i}h'(\theta_{700} - T_s) - (t_u U' + t_v V')) + a_c V_s' \Delta q_0[1 - (\theta_{Z_T} - T_s)/\Delta\theta_{\max}] = C_f' F_{crf}^0 \quad (5.44)$$

The surface pressure gradient is determined by a mixing layer depth perturbation and ocean surface SST.

#### *5.4.1.1 Random fluctuations parameterization for surface wind moments*

Horizontal turbulent fluctuations of surface zonal wind and meridional wind are neglected in the deterministic model for mean states. However, in small time scales and space scale variations, horizontal eddy transports become important and complicated, which can be parameterized as

$$\partial_x(\overline{u'u'}) - \partial_y(\overline{u'v'}) = V_s[C_u(\partial_x u' + \partial_y v')] = V_s'[S_u \dot{W_u}] \quad (5.45)$$

$$\partial_x(\overline{u'v'}) - \partial_y(\overline{v'v'}) = V_s[C_v(\partial_x v' + \partial_y v')] = V_s'[S_v \dot{W}_v] \qquad (5.46)$$

The horizontal gradient of surface wind perturbation is affected by ocean surface wave and eddies of small scale and mesoscale. The total effects resemble a random process with fluctuation strength proportional to the surface wind speed. In equation (5.45) and (5.46), $\dot{W}$ is a random number between -1 and 1, $S_u$ and $S_v$ are defined as strengths of momentum random force per unit wind speed for zonal wind and meridional wind respectively.

*5.4.1.2 Random fluctuations parameterization for boundary layer height*

Cloud top radiative cooling and surface flux are affected not only by ocean surface and atmosphere mean properties, but also strongly affected by random process due to water droplet perturbations and evaporation fluctuations. This study separates the unit area cloud top radiative cooling $F_{crf}^0$ into its mean part $\overline{F_{crf}^0}$ and random part $\left(F_{crf}^0\right)'$, and assuming other random process independent of marine cloud fractions, the boundary layer height equation becomes

$$\partial_t h = \frac{\left(\gamma F_{crf}^0 C_f' Z_T\right)}{(\bar{h} + h')(\theta_{Z_T} - T_s)} - D_{zi} h + S_{crf} \dot{W}_h \qquad (5.47)$$

$$S_{crf} \dot{W} = c_1 \overline{C_f} (F_{crf}^0)' / h \qquad (5.48)$$

In equation (5.47), $S_{crf}$ represents the strength of entrainment rate fluctuations due to variations of unit area cloud top radiative cooling. It is still a big challenge to accurately estimate the amplitude of the entrainment random perturbations. However, one major finding in the 2001 EPIC field study (Bretherton et al, 2005) is that boundary layer

height variation is surprising high at around $100 \sim 300m/3hr$ in the south east Pacific region during the MSC maximum season. Based on this observation, it is reasonable to assume that the boundary layer height random perturbation rate could have similar amplitudes as that due to large scale divergence. In section 5.4, random perturbation coefficients are allowed to change in order to study how they affect the surface wind standard deviation and skewness.

In summary, the stochastic model for surface wind, boundary layer height and marine low clouds are obtained from equations (5.41)-(5.48).

$$\partial_t U' = a_u(\theta_{700} - T_s)h'/\Delta\theta_0 + fV' - C_d(\overline{V_s}U' + V_s'\overline{U})/h_0 + V_s' S_u \dot{W}_U \qquad (5.49)$$

$$\partial_t V' = a_v(\theta_{700} - T_s)h'/\Delta\theta_0 - fU' - C_d(\overline{V_s}V' + V_s'\overline{V})/h_0 + V_s' S_v \dot{W}_v \qquad (5.50)$$

$$\partial_t h' = \frac{\left(\gamma F_{crf}^0 C_f' Z_T\right)}{(\overline{h} + h')(\theta_{Z_T} - T_s)} - D_{zi}h' + S_{crf}\dot{W}_h \qquad (5.51)$$

$$C_f' = [0.3c_p(D_{z_i}h'(\theta_{700} - T_s) - (t_u U' + t_v V')) + a_c V_s' \Delta q_0 [1 - (\theta_{Z_T} - T_s)/\Delta\theta_{\max}]/F_{crf}^0 \qquad (5.52)$$

In the following model simulations, surface wind speed $V_s$ is calculated using both the model simulated surface wind anomaly and QuikSCAT three-year averaged seasonal winds.

### 5.4.2 Stochastic Methods

The method to obtain model solutions forced by random perturbations is as follows. For any given initial conditions, it is assumed that the time interval for an external random forcing is much longer than the time needed for convective boundary layer wind

reaches its equilibrium solution, which is typically between 20minutes to 1 hour. Considering now a given set of initial condition $(U_0(i), V_0(i), H_0(i))$ and a random perturbation $\Sigma\dot{W}(i)$, we could obtain a set of stable state solutions $(U_*(i), V_*(i), H_*(i))$ based on equations (5.49)-(5.52) and Euler forward time iterations until a variable satisfies $X(t) - X(t-1) \le \varepsilon\Delta t$ . For any given set of initial conditions $(U_0(m), V_0(m), H_0(m))$, we obtain the mean value, the standard deviation, and the skewness of surface wind $(mean(X), std(X), skw(X))$, $X \in (U, V, H)$ using the following procedure. Given a series of random perturbation $\dot{W}(i), i = 1,2,..., N$ , we could obtain a series of stable solutions $(U_*(i), V_*(i), H_*(i)), i = 1,2,..., N$, then calculate their statistical values based on the following definitions:

$$MEAN(X) = \frac{1}{N}\sum_{i=1}^{N} X(i) \tag{5.53}$$

$$STD(X) = \sqrt{\frac{1}{N-1}\sum_{i=1}^{N}(X(i) - \overline{X})^2} \tag{5.54}$$

$$SKEW(X) = \left(\frac{1}{N}\sum_{i=1}^{N}(X(i) - \overline{X})^3\right) / (STD(X))^3 \tag{5.55}$$

Here $MEAN(X)$ is the mean value of a given random variable $X(n)(n = 1,2,..., N)$; $STD(X)$ is called the standard deviation of $X$ which is a measure of the degree to which the values of $X$ deviate from the mean value; $SKEW(X)$ is called the skewness of $X$ , the normalized third-order moment, is a measure of the lopsideness of the PDFs.

### 5.4.2 Observed and Model Simulated Surface Wind Speed PDF as Functions of Local Wind Speed and Ocean Surface SST

As shown in the stochastic model of equation (5.49)-(5.52), the departure of surface winds from their seasonal cycles is determined by surface pressure gradient perturbations, the coriolis force, surface friction, and momentum random forces. The surface pressure gradient depends on ocean surface SST and boundary layer height anomaly. The time derivation of boundary layer height anomaly is controlled by marine cloud fraction anomaly, large scale divergence, and random entrainment fluctuations. Previous studies observed a positive relationship between the standard deviations of surface wind speed with strengths of random fluctuations and a negative relationship between the skewness and its mean value of surface wind due to surface friction in global scales (Monahan 2005, 2006). In subtropical marine clouds regions, both marine cloud top radiation cooling and surface friction affect the surface wind probability distribution. Then what are the observed relationships among the mean surface wind speed, its higher order moments, and ocean surface SST in the subtropical MSC regions? How do ocean surface SST, large scale divergence, cloud internal fluctuations, and eddy transport fluctuations affect these relationships?

#### *5.4.2.1 Relationship between surface wind PDF and surface wind speed*

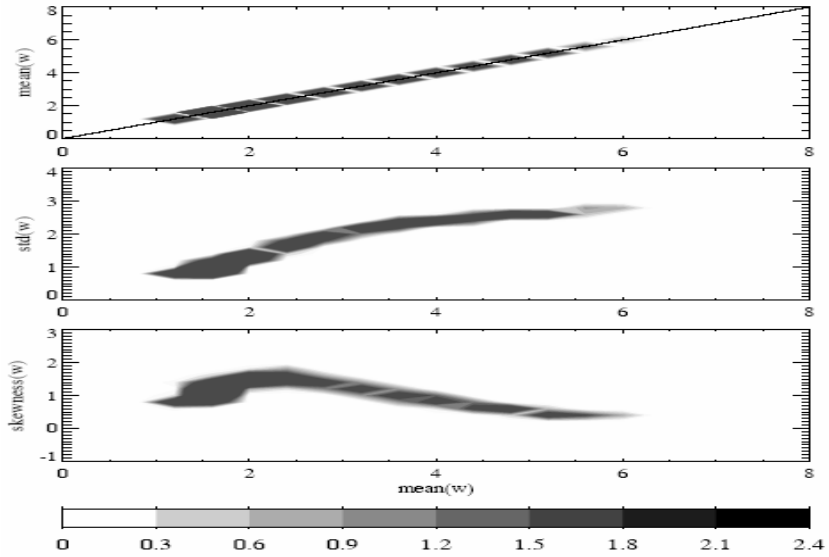


(a) statistics for three-year period

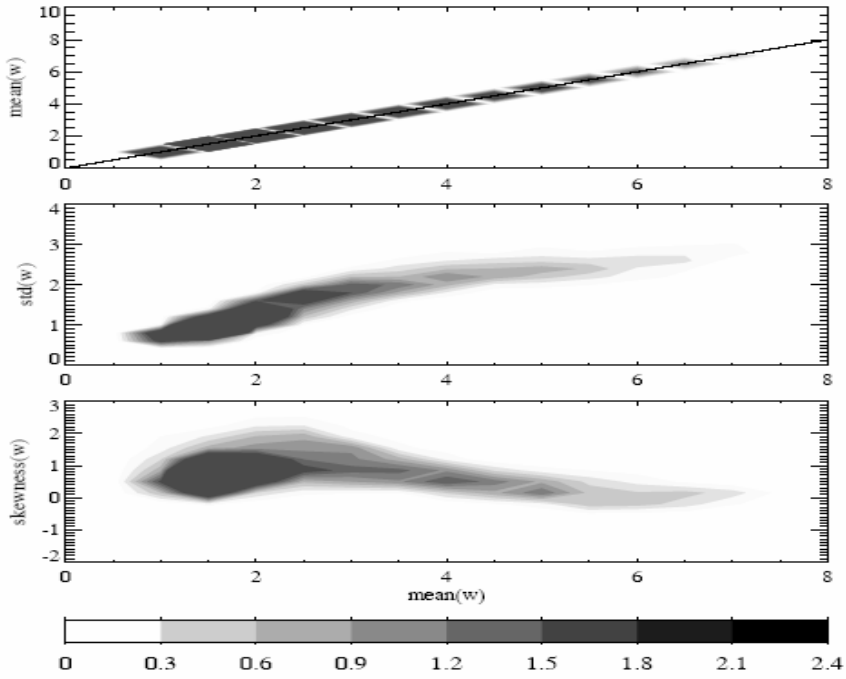


(b) statistics for seasonal period

**Figure 5.8** QuikSCAT ocean surface winds probability distribution plotted against the QuikSCAT mean surface wind speed in the southeast Pacific $(30S-10S,100W-80W)$ during the period from Mar 2003 to Feb 2006. The upper panel represents $MEAN(V_s)$, the middle panel represents $STD(V_s)$, and the lower panel represents $SKEW(V_s)$. The seasonal variations have been removed from the original data.

The three-year averaged seasonal cycle is removed from the original QuikSCAT data. The resulting surface wind time series is further processed to get the mean value, and the standard deviation, and the skewness at $1^{\circ} \times 1^{\circ}$ horizontal resolution. The mean value (upper panel), the standard deviation (middle panel), and the skewness (lower panel) are calculated for a three-year period in Figure 5.8.a and for every season period in Figure 5.8.b as functions of QuikSCAT non-seasonal surface wind speed. A positive relationship between the standard deviation and its mean value of surface wind speed is evident in Figure 5.8. A negative relationship between the skewness and mean surface wind speed as suggested in previous theoretical study (Monahan 2005) is observed when the wind speed is not small. In small wind regimes, the skewness increases with increasing surface wind speed because the buoyancy effect is greater than surface fraction effects. The observed relationship between moments and the mean value of surface wind speed is simulated using the stochastic model.

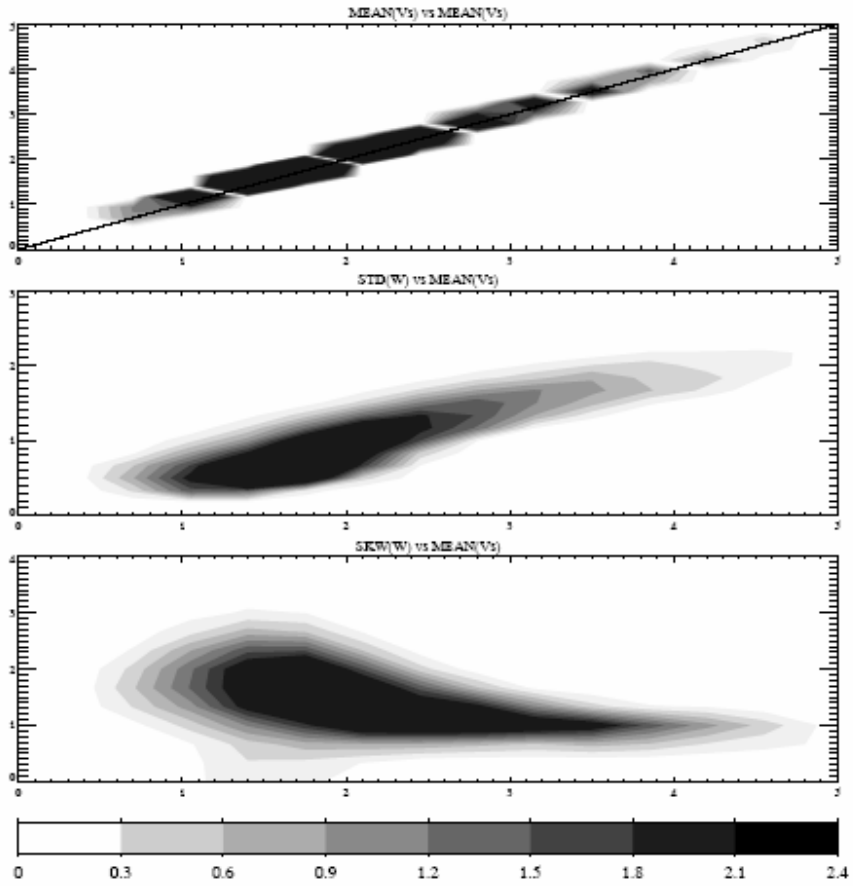


**Figure 5.9** Model simulated surface wind mean value (upper panel), the standard deviation (middle panel), and the skewness (lower panel) as functions of surface mean wind speed. The seasonal variation is removed from the original surface winds.

Figure 5.9 is the model simulated mean surface wind mean value (upper panel), the standard deviation (middle panel), and the skewness (lower panel) as functions of surface mean wind speed. In the simulation, the large scale divergence is set to $3\times10^{-6}/s$, the entrainment ratio is set to 0.2, the strength of momentum random forcing is given $S_u = S_v = 4.5\times10^{-5}/s$, and the strength of entrainment fluctuation is given $S_{crf} = 1\times10^{-3} m/s$, ocean surface SST is linearly changed from $16^{\circ}C$ to $26^{\circ}C$. The surface wind standard deviation is primarily determined by the strength of momentum random forcing and the strength of cloud internal fluctuations. It is also influenced by large scale divergence. Influences of various factors on standard deviations are discussed further in section 5.5 and 5.6. Both QuikSCAT observed and the model simulated surface wind skewness has a nonlinear relationship with its mean value. In large wind regimes, the stronger the wind speed is, the larger the surface friction becomes, and the more tendency of wind probability distribution towards extremely small wind. However, in small wind regimes, increasing mean value of surface wind speed leads to stronger cloud top radiative cooling, and the resulting mixing layer deepening further enhances the strength of momentum fluctuations, pushing the surface wind probability distribution towards an extremely large value. Cloud top radiative cooling, boundary layer deepening, and surface wind fluctuations are tightly coupled in determining the surface wind PDF, particularly for small wind conditions.

#### *5.4.2.2 Surface wind PDF and ocean surface SST*

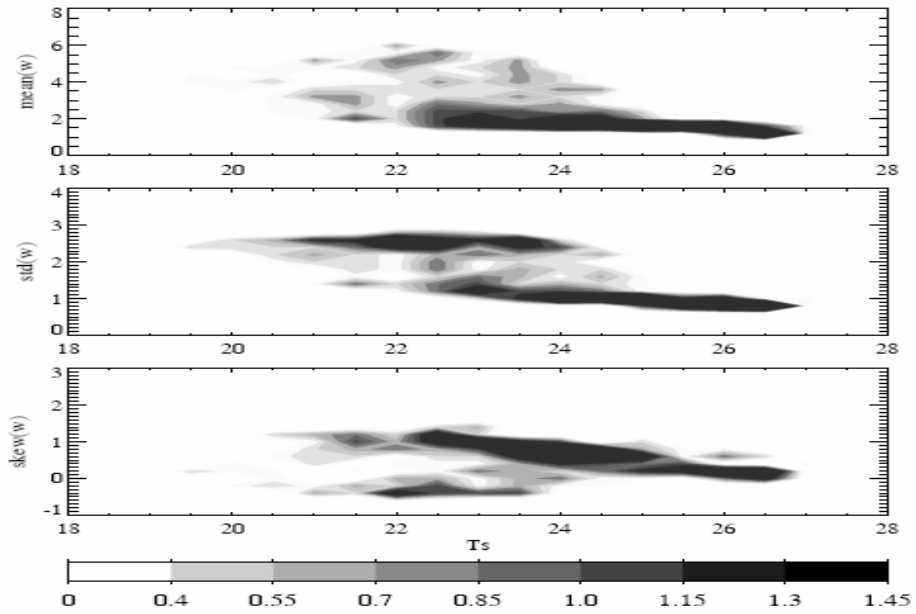


(a) statistic on three-year period

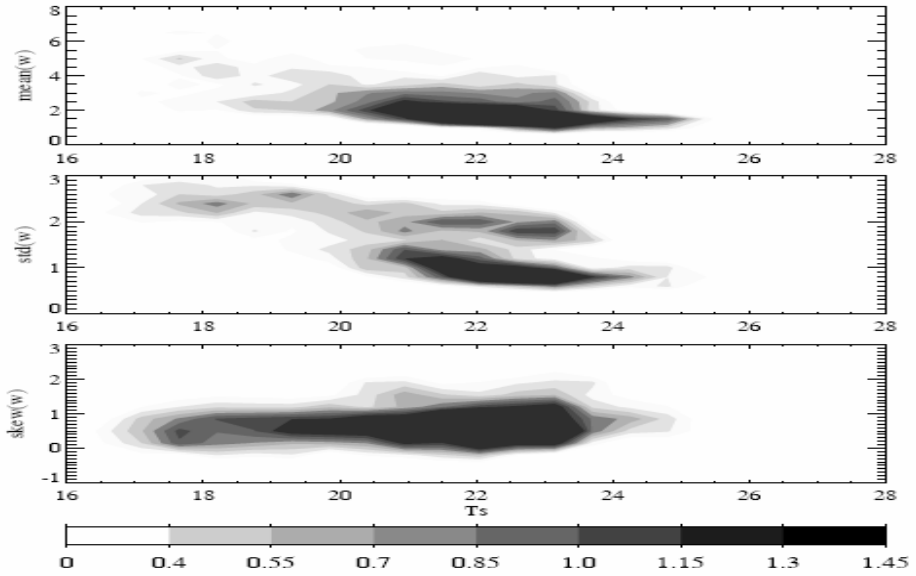


(b) Statistic on seasonal period

**Figure 5.10** QuikSCAT ocean surface wind probability distribution plotted against the AIRS mean ocean surface SST in the southeast Pacific $(30S-10S,100W-80W)$ during the period from Mar 2003 to Feb 2006. The upper panel represents $MEAN(V_s)$, the middle panel represents $STD(V_s)$, and the lower panel represents $SKEW(V_s)$. The seasonal variations have been removed from the original data.

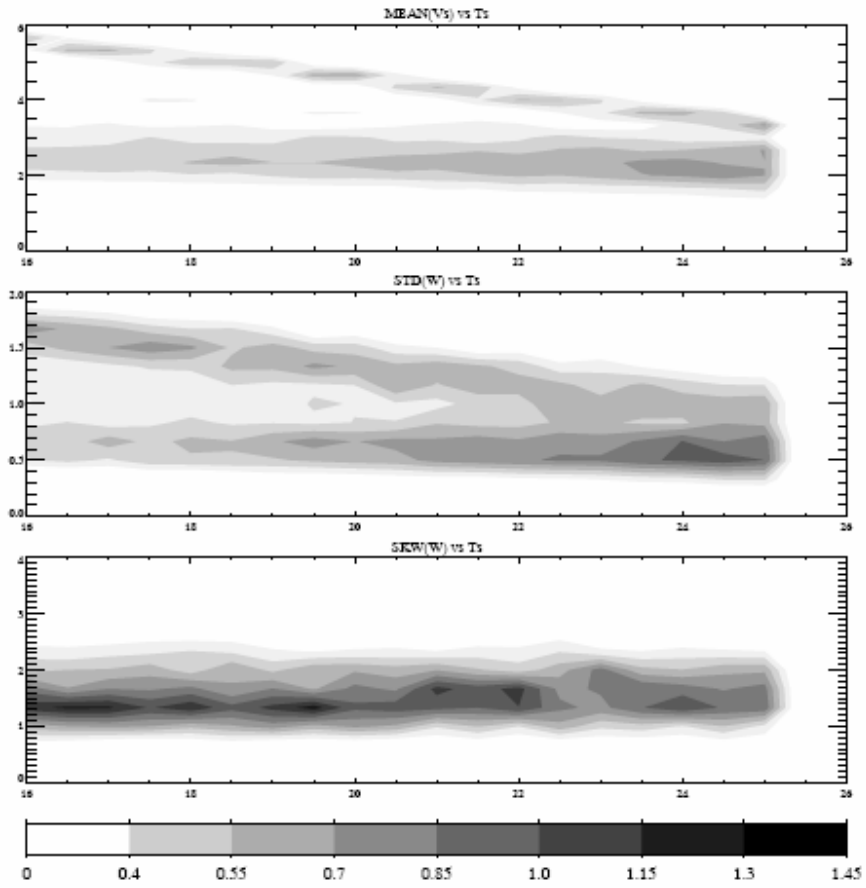


**Figure 5.11** Model simulated surface wind mean value (upper panel), the standard deviation (middle panel), and the skewness (lower panel) as functions of ocean surface mean SST. The seasonal variation is removed from the original surface winds.

Figure 5.10 is the QuikSCAT observed mean value (upper panel), the standard deviation (middle panel), and the skewness (lower panel) of surface wind speeds as functions of AIRS ocean surface SST in the south east Pacific. QuikSCAT non-seasonal mean value, standard deviation, and skewness are calculated for the three-year period in Figure 5.10.a, and for every season period in Figure 5.10.b. Figure 5.11 is the model simulated surface wind moments as functions of ocean SST, which agrees well with satellite observations shown in Figure 5.10. The mean non-seasonal surface wind speed is decreased with ocean surface SST because ocean surface pressure gradients depend on temperature inversion strength and marine boundary clouds. When ocean surface is warmer, the temperature inversion is weaker and less marine boundary clouds are formed in the subsidence regions, resulting in smaller surface winds. Multiple equilibriums exist in the observed standard deviation of surface wind speed in different SST regimes. The observed standard deviation has one high value of approximately $2.5 m/s$ when SST is colder than $20^{\circ}C$; it has two equilibrium values when SST is between $20^{\circ}C$ and $22^{\circ}C$; and it has one low value of approximately $1 m/s$ when SST is warmer than $22^{\circ}C$. The standard deviation of surface wind speed is directly related to mean surface wind speed, the strength of random fluctuations, and surface frictions, which are directly and indirectly determined by ocean surface SST. The skewness of surface wind speed is observed to be slightly decreased with ocean surface SST. Influences of various factors on standard deviations and skewness of wind speed are briefly discussed based on model experimental results in section 5.5 and section 5.6.

## 5.5 Influences of Various Factors on Local Relationships between Surface Wind PDF and Surface Wind Speed

Figure 5.12 is the model simulated standard deviations of surface wind speed plotted against surface wind speed with varying (a) large scale divergence ($\times 10^{-6}/s$), (b) entrainment ratio, (c) Strength of momentum random force ($4.5\times 10^{-5}/s$), and (d) Strength of entrainment fluctuations ($1\times 10^{-3} m/s$). The model simulated relationships between standard deviation and its mean value of surface wind speed are significantly different when large scale divergence is different. The model simulated standard deviation is increased with mean surface wind speed when large scale divergence is small. However, it has two peak values with mean wind speed when large scale divergence is large. The standard deviation also has two peak values when the entrainment fluctuation strength is small, and is linearly increased with mean surface wind speed when the entrainment fluctuation strength is large. Increasing the strength of momentum fluctuations and entrainment ratio will increase the value of standard deviations. Theoretical explanation is a future study.

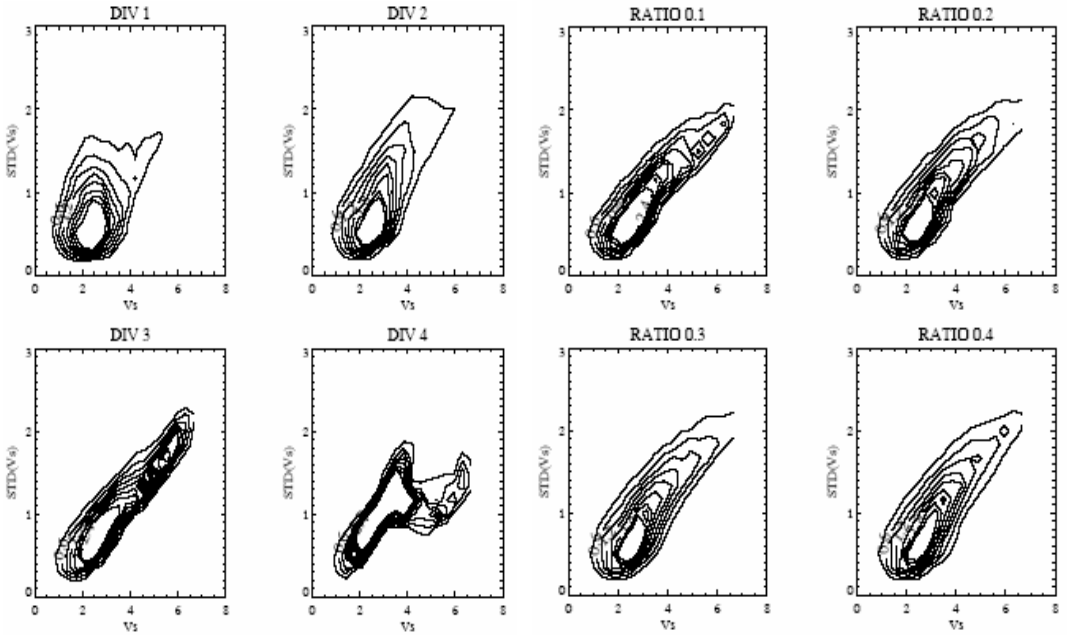


(a) Large scale divergence ($\times 10^{-6}/s$) (b) Entrainment ratio

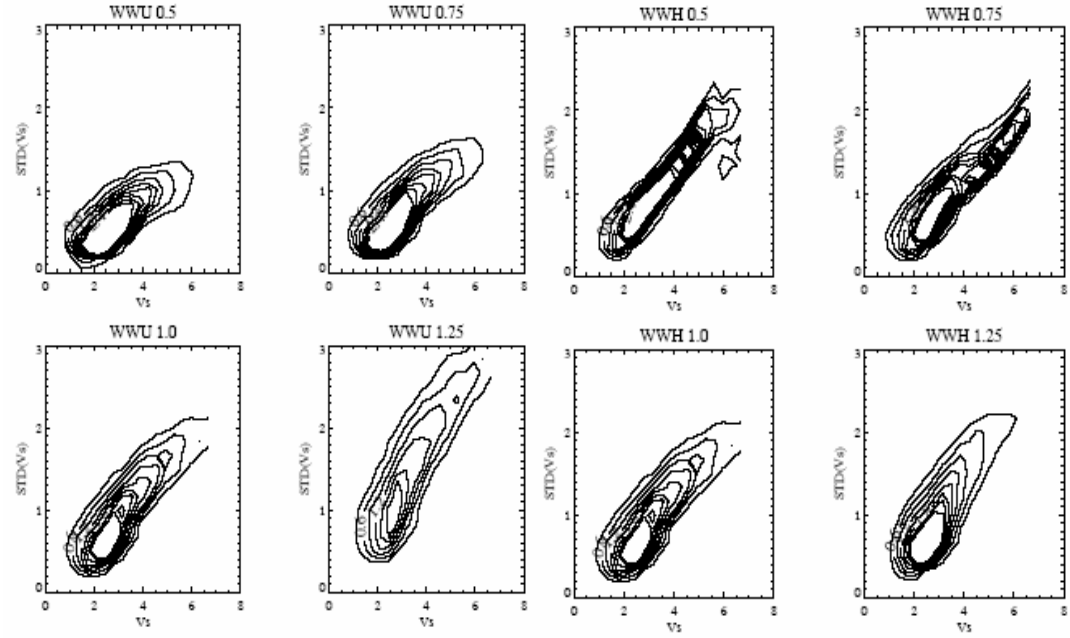


(c) Strength of momentum random force (d) Strength of entrainment fluctuations

**Figure 5.12** Model simulated standard deviations of surface wind speed plotted against surface wind speed with varying (a) large scale divergence ($\times 10^{-6}/s$), (b) entrainment ratio, (c) Strength of momentum random force ($4.5\times 10^{-5}/s$), and (d) Strength of entrainment fluctuations ($1\times 10^{-3} m/s$).

Figure 5.13 is the model simulated skewness of surface wind speed plotted against surface wind speed with varying (a) large scale divergence ($\times 10^{-6}/s$) , (b) entrainment ratio, (c) Strength of momentum random force ($4.5\times 10^{-5}/s$)), and (d) Strength of entrainment fluctuations ($1\times 10^{-3} m/s$) . Skewness is increased with wind speed in when wind speed is smaller than a critical value due to buoyancy effect; and decreased with wind speed in large wind regimes. The relationship between skewness and its mean value is greatly influenced by large scale divergence, the strength of momentum fluctuations, and the strength of entrainment fluctuations. Increasing large scale divergence or decreasing strengths of entrainment fluctuations both result in the shift of critical wind speed value toward larger values. In other words, the tendency toward extremely large wind speed is enhanced when large scale divergence is strong and/or the strength of entrainment fluctuations due to unit are cloud top radiative cooling perturbation become small. Skewness values become larger in most wind speed regimes when the strength of wind momentum fluctuations increases. Skewness decreases faster with mean wind speed when the entrainment ratio is increased.

## 5.6 Influence of Various Factors on Local Relationships between Moments of Surface Wind Speed and Ocean Surface SST

As shown in section 5.4, the standard deviation has two equilibrium values when SST is between a cold value and a warm value. Figure 5.14 Model simulated standard deviations of surface wind speed plotted against ocean surface SST with varying (a) large scale divergence ($\times 10^{-6}/s$) , (b) entrainment ratio, (c) Strength of momentum random

force $(4.5\times10^{-5}/s)$), and (d) Strength of entrainment fluctuations $(1\times10^{-3}m/s)$. The high equilibrium value is developed in most SST regimes when large scale divergence become stronger, strengths of cloud entrainment fluctuations become weaker, and entrainment ratio become small. The low equilibrium value is developed in most SST regimes when large scale divergence is small, strengths of cloud entrainment fluctuations become large, and the entrainment ratio become large. Increasing strengths of momentum fluctuations increases the standard deviation value.

Influences of various factors on the model simulated relationships between surface wind speed skewness and ocean surface SST are found to be not significant in the model experiment runs (which are not shown here).

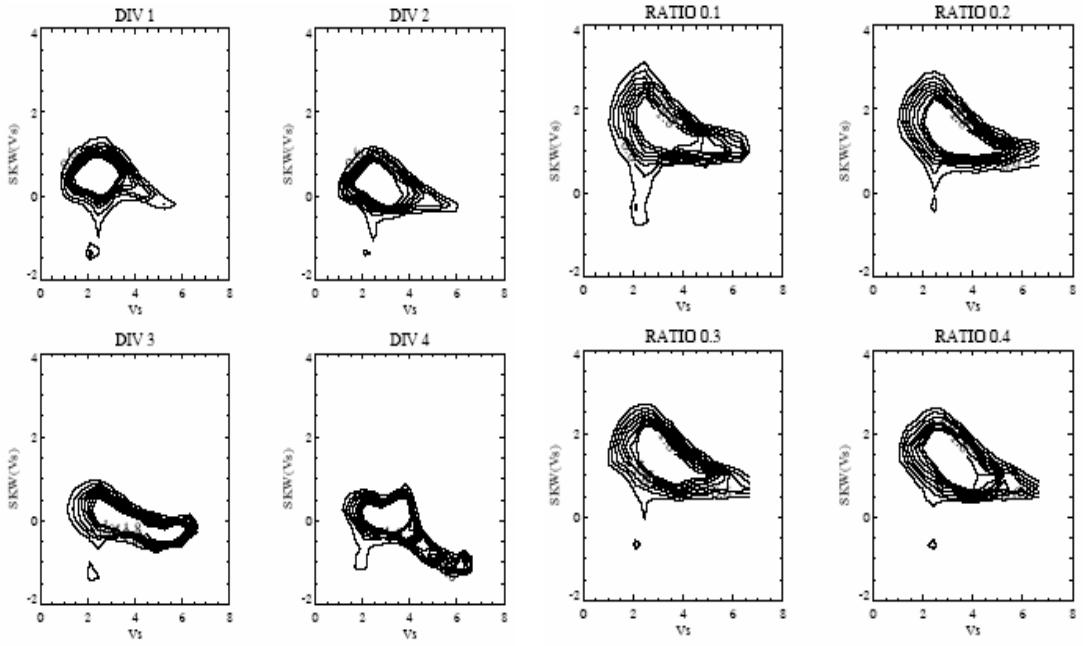


(a) Large scale divergence ($\times 10^{-6}/s$) (b) Entrainment ratio

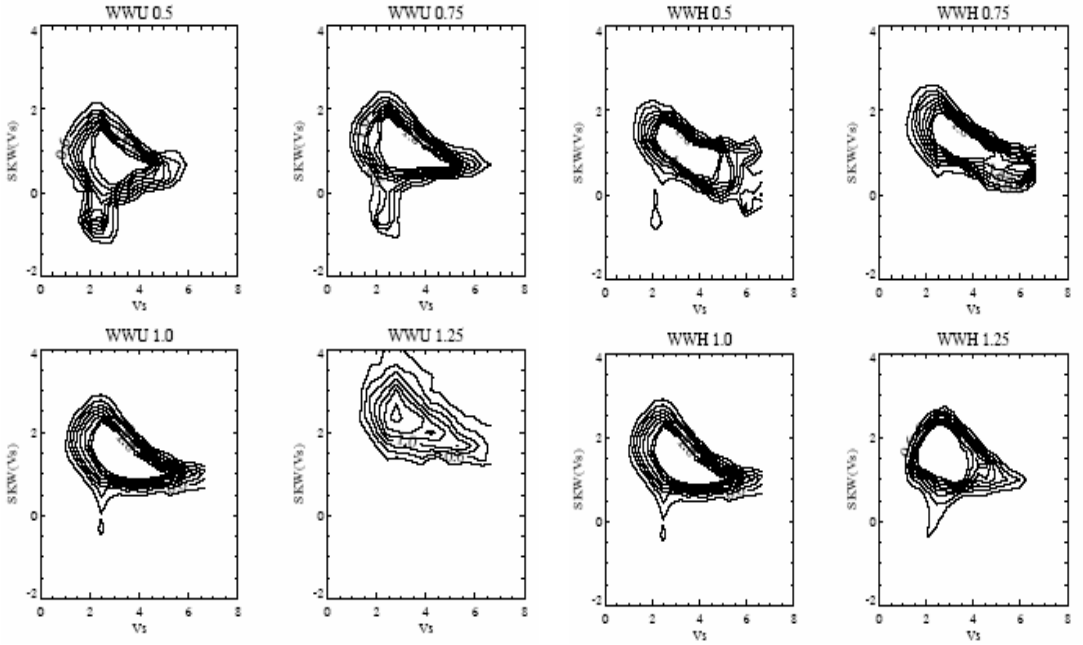


(c) Strength of momentum random force (d) Strength of entrainment fluctuations

**Figure 5.13** Model simulated skewness of surface wind speed plotted against surface wind speed with varying (a) large scale divergence ($\times 10^{-6}/s$), (b) entrainment ratio, (c) Strength of momentum random force ($4.5\times 10^{-5}/s$), and (d) Strength of entrainment fluctuations ($1\times 10^{-3} m/s$).

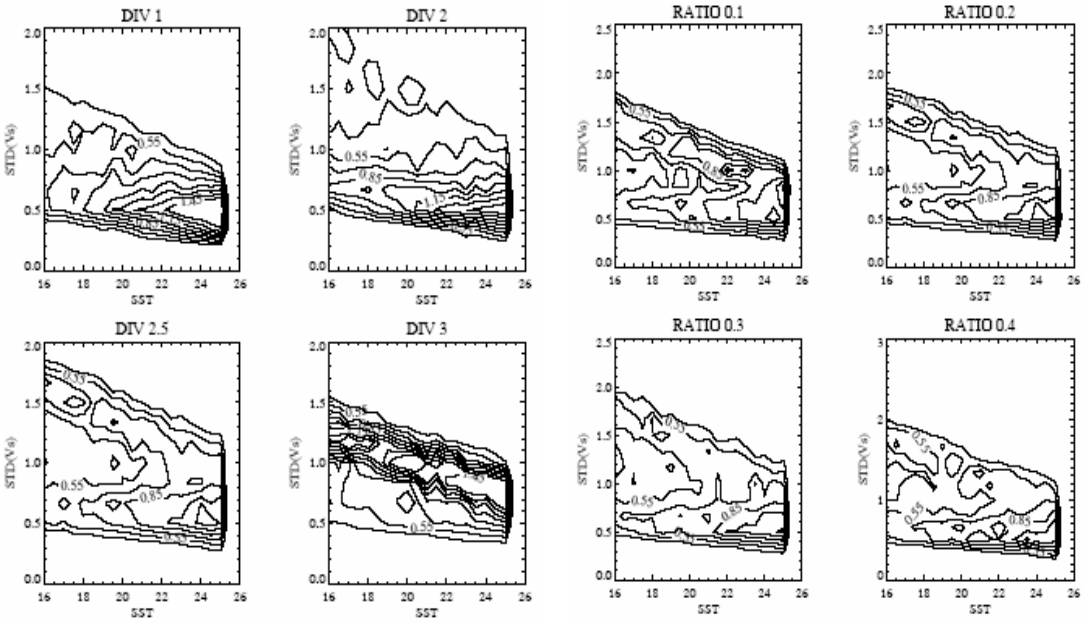


(a) Large scale divergence ($\times 10^{-6}/s$) (b) Entrainment ratio

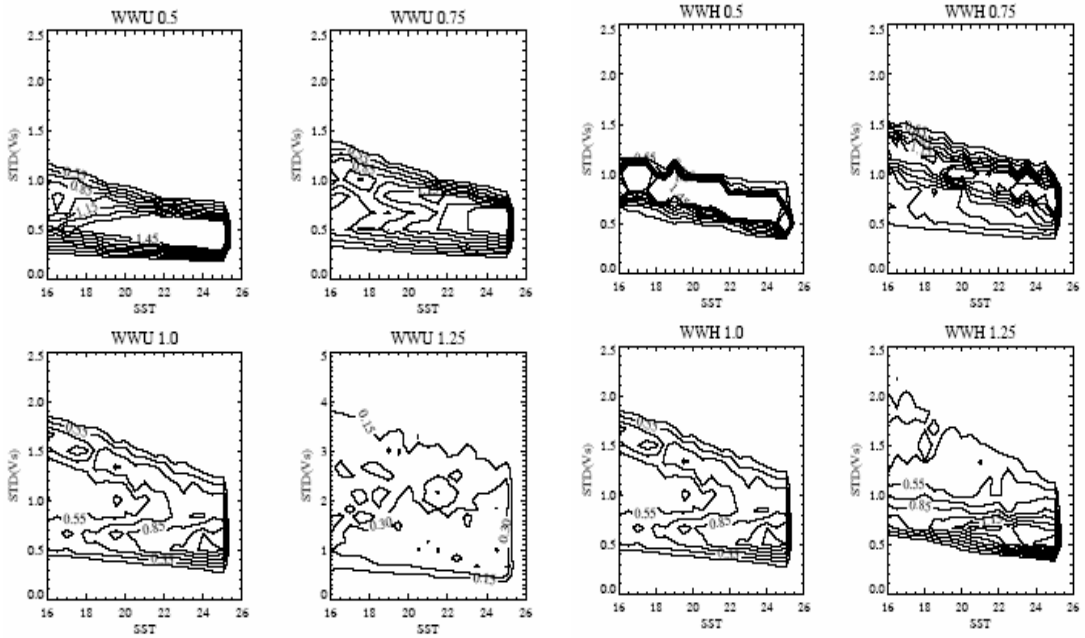


(c) Strength of momentum random force (d) Strength of entrainment fluctuations

**Figure 5.14** Model simulated standard deviations of surface wind speed plotted against ocean surface SST with varying (a) large scale divergence ($\times 10^{-6}/s$), (b) entrainment ratio, (c) Strength of momentum random force ($4.5\times 10^{-5}/s$), and (d) Strength of entrainment fluctuations ($1\times 10^{-3} m/s$).

## 5.7 Conclusions

This chapter is aiming to understand influences of ocean surface SST, large scale divergence, and marine low clouds on the mean state and the probability distribution of local ocean surface wind in the southeast Pacific. A simple conceptual model was developed based on the following observed physical concepts: persistent marine stratus and stratocumulus exist in the broad area of large scale subsidence regions, where the lower troposphere is characterized by a moist, cold boundary air topped by dry, hot free air below a trade wind inversion. Surface pressure gradients are determined by ocean surface SST and boundary layer height variations. The later is driven by cloud top radiative cooling and surface flux in the south east Pacific. When large scale divergence becomes larger, greater amounts of dry static energy and momentum are transported from the free atmosphere into the boundary layer; more marine boundary clouds are developed, which leads to the mixing layer deepening due to stronger cloud top radiative cooling. The resulting increase of surface winds further enhances the ocean surface flux and the horizontal transport of available dry inhibition energy (ADIN), which further increases boundary layer clouds. The interactions between clouds, large scale divergence, and surface wind are strongly affected by ocean surface SST. When ocean surface is warmer, the cloud top temperature inversion becomes weaker while the mixing layer becomes deepened. The surface pressure gradients can either be increased or decreased depending on which factors dominate the inversion strength or the boundary layer height. The change of ADIN horizontal transport due to SST related surface winds change leads to

the change of marine cloud fractions, which further change the convective boundary layer height.

The model based physical picture suggests the local positive relationships between the mean state of ocean surface winds and ocean surface SST, large scale divergence, and marine boundary clouds. It is supported by three-year QuikSCAT surface wind observations and fifteen-year ERA40 monthly reanalysis data. The mean state and moments of QuikSCAT non-seasonal surface winds are successfully simulated when random fluctuations due to horizontal eddy transport and cloud internal variations are added to the simple conceptual model. The standard deviation of surface wind speed increases with increasing surface wind but has multiple equilibrium relationships with ocean surface SST. Surface wind skewness decreases with wind speed in a large wind regime due to surface friction effect. However it increases with wind speed in the buoyancy controlled small wind regime. Model sensitive tests suggest large scale divergence, and strengths of momentum and cloud fluctuations have significant effects on the surface wind PDF and its relationship with ocean surface SST and surface wind speed. Implication of marine boundary clouds for Walker Circulation and tropical waves is a future study. Theoretical analysis of model's nonlinear dynamics and parameterization of surface wind PDF based on surface wind speed, SST, marine clouds, and large scale divergence will also be addressed in the future.

# CHAPTER 6

# SUMMARY AND FUTURE RESEARCH

## 6.1 Synthesis of How Clouds Interact through Teleconnection with Large Scale Flows in the Tropics and Subtropics

Marine boundary clouds are of central importance for the earth surface energy budget, tropical dynamics, and air-sea interactions. They play significant roles in climate change modeling and weather predictions. However, the physical processes associated with boundary layer clouds and their interactions with large scale flows are poorly understood and their representation in climate models still leaves much to be desired. This dissertation improves our understanding on the interactions between marine boundary clouds and large scale flows over the subtropical oceans, and better represents the monthly, seasonal, and interannual variations of marine low cloud amounts in subtropical MSC regions. The mean states and the non-seasonal variations of ocean surface wind are also better simulated when the influences of ocean SST, large scale divergence, and marine boundary clouds are included in a simple ocean surface wind model. The key idea for understanding marine boundary clouds is that in climate space and time scale, marine boundary clouds are tightly coupled with the large scale circulation in maintaining a preferred lower troposphere convective inhibition energy such that the redistribution of energy in efficient over tropical and subtropical oceans.

The interaction between deep convection and large scale flows are extensively studied and modeled using the QE constraint within tropical atmosphere. Recent study of

Neelin and Su (2005) has applied QE theory in understanding and simulating the moist teleconnection mechanisms for the tropical South American and Atlantic Sector. They found that the leading mechanism for drought in eastern equatorial South American is that QE mediation of teleconnected tropospheric temperature anomalies tends to provide moisture gradients between the strong convective regions and the nearby non-convective regions. Their physical picture is incomplete because the role of marine boundary clouds in adjusting and modifying boundary layer wind, moisture, and surface flux are neglected. This limits the application of their proposed mechanisms to land areas where the remote effects of marine boundary clouds are secondary.

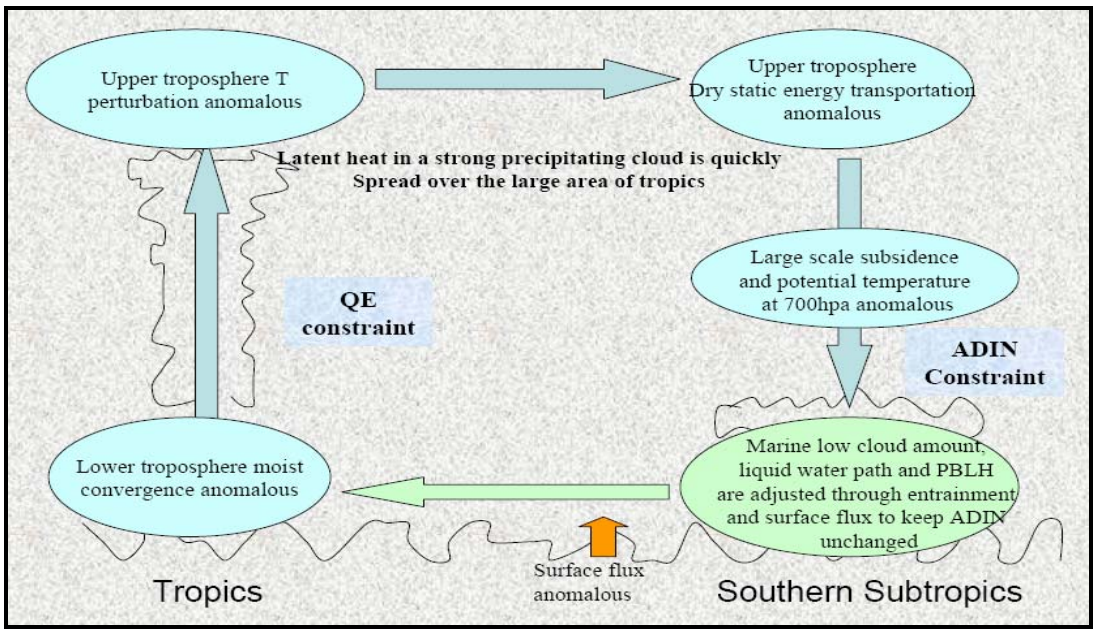


**Figure 6.1** Cartoon of synthesized teleconnection pictures over tropical and subtropical oceans

Figure 6.1 shows how clouds interact with large scale flows over tropical and subtropical oceans. The role of quasi-equilibrium links lower troposphere moist

convergence anomalies to upper troposphere temperature anomalies in tropical convective regions. The latent heat released in a strong precipitation cloud is quickly spread over the most tropical regions. Extra dry static energy is transported from tropics to subtropics in the upper troposphere, resulting in descent anomalies and potential temperature anomalies just above the trade wind inversion. Marine boundary clouds, liquid water path, and boundary layer height have to be adjusted in a way to radiate back the extra energy into space in order to maintain the lower troposphere available dry energy (ADIN). Both the near surface return flow and the surface flux are influenced by ADIN constraint. The effects of the ADIN constraint on lower troposphere moisture convergence variations and precipitation variations in tropics are subjects for future research. Understanding implications of marine boundary clouds for Walker circulation and wave propagations can greatly improve ENSO forecast and tropical climate simulations, which will be addressed in future studies.

## 6.2 Current and Future Research in Simulating Cloud Interacts with Large Scale Flows in the Global Climate Models

Many convective models based on QE theory keep the environmental stratification profile unchanged. They need not be directly coupled with a dynamical core, and can be based only on the local temperature and humidity profiles in calculating convective heating and precipitations. This is not the case for marine boundary clouds. The adjusted time scale for deep convection is between minutes to hours. However, marine stratus and stratocumulus can persist for days. Dynamical transport of available energy variation has comparable timescales with cloud top radiative cooling variation. The developed new cloud cover scheme in Chapter 2 and Chapter 3 need both local and

non-local inputs. Current and future research in simulating marine boundary clouds for the NCAR CAM climate model is summarized in Figure 6.2.

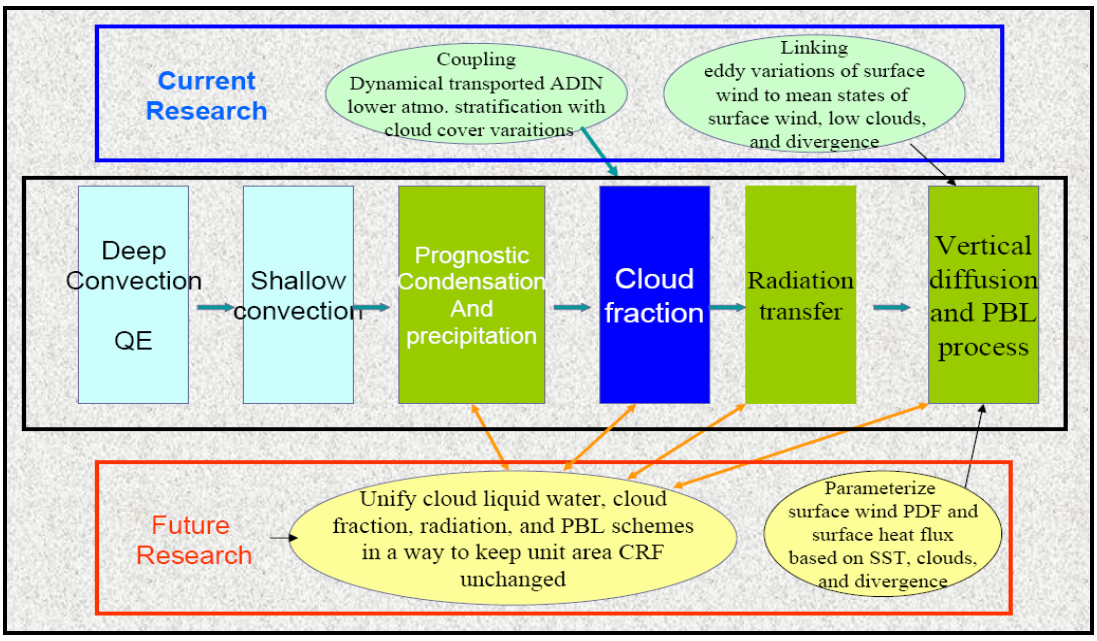


**Figure 6.2** Cartoon of current and future research in understanding and simulating how clouds interact with large scale flows in the NCAR CAMs.

It is shown in Chapter 3 that a significant increase of marine low cloud amounts didn't lead to corresponding increase of loud liquid water path in subtropical MSC regions. Therefore the seasonal variations of solar radiation at surface and TOA only showed a little change. To further improve the marine boundary cloud simulations, the cloud condensation and precipitation scheme, cloud fraction scheme, and boundary layer turbulence scheme have to be tightly coupled to keep the unit area cloud radiative cooling relatively unchanged in climate models. The surface wind PDF will be parameterized based on surface wind speed, ocean SST, marine clouds, and divergence. Ocean surface

fluxes can be estimated more accurately when ocean surface wind heterogeneity is considered in the surface flux scheme.

# REFERENCES


Arakawa, A. and W. H. Schubert, 1974: Interaction of a cumulus cloud ensemble with the large-scale environment, Part I. *J. Atmos. Sci*., 31, 674-701.

Bajuk, L., and C. B. Leovy, 1998a: Are there real interdecadal variations in marine low clouds. *J. Climate*, **11,** 2910–2921.

Bajuk, L., and C. B. Leovy, 1998b: Seasonal and interannual variations in stratiform and convective clouds over the tropical Pacific and Indian oceans from ship observations. *J. Climate*, **11,** 2922–2941.

Betts, A. K., 1990: A cloudiness transition in a marine boundary layer. *J. Atmos. Sci*., **47,** 1480–1497.

Bretherton, C., and M. C. Wyant, 1997: Moisture transport, lower-troposphere stability, and decoupling of cloud-topped boundary layer. *J. Atmos. Sci*., **54,** 148–167.

Bretherton, C.S., T. Uttal, C.W. Fairall, S.E. Yuter, R.A. Weller, D. Baumgardner, K. Comstock, R. Wood, and G. B. Raga, 2004: The EPIC 2001 Stratocumulus Study, *BAMS*, **85**, 967-977.

Bony S, and Dufresne JL, 2005: Marine boundary layer clouds at the heart of tropical cloud feedback uncertainties in climate models, *JRL*, **32**, Art. N. L20806, 2005.

Clement,A., and R. Seager, 1999: Climate and the tropical oceans. *J.Climate*, **13,** 3383–3401.

Chaboureau, J. P., F. Guichard, J. L. Redelsperger, and J. P. Lafore, 2004: The role of stability and moisture in the diurnal cycle of convection over land. *Q. J. R. Meteorol. Soc.*, **130**, 3105-3117.

Deardorff, J. W., 1980: Cloud top entrainment instability. *J. Atmos. Sci*., **37,** 131–147.

Dima I. and J.M. Wallace, 2003: On the Seasonality of the Hadley Cell, *JAS*, **60**, 1522-1526.

Emanuel, K.A., 1994: Atmospheric Convection. *Oxford University press*, 580pp.

Gill, A.E., 1980: Some simple solutions for heat-induced tropical circulation. *Q.J.R.Met. Soc.*, **106**, 447-462.

Grinsted A., J.C. Moore, and S. Jevrejeva, 2004: Application of the cross wavelet transform and wavelet coherence to geophysical time series. *Nonlinear Processes in Geophysics*, **11**, 561-566.

Isemer, H. and L. Hasse, 1991: The scientific Beaufort equivalent scale: Effects on wind statistic and climatology and oceanography. *Bull. Amer. Met. Soc.*, **79**, 1855-1870.

Jevrejeva S., J.C. Moore, and A. Grinsted, 2003: Influence of the Arctic Oscillation and El Nino-Southern Oscillation (ENSO) on ice conditions in the Baltic Sea: The wavelet approach. *JGR,* **108**, D214677.

Kalnay, E., M. Kanamitsu, R. Kistler, W. Collins, D. Deaven, L. Gandin, M. Iredell, S. Saha, G. White, J. Woollen, Y. Zhu, A. Leetmaa, B. Reynolds, M. Chelliah, W. Ebisuzaki, W. Higgins, J. Janowiak, K. C. Mo, C. Ropelewski, J. Wang, Roy Jenne and Dennis Joseph, 1996: The NCEP-NCAR 40-year reanalysis project. *BAMS*, **77,** 437–471.

Klein, S. A., and D. L. Hartmann, 1993: The seasonal cycle of low stratiform clouds. *J. Climate*, **6,** 1587–1606.

Klein, S. A., D. L. Hartmann, and J. R. Norris, 1994: On the relationships among low-cloud structure, sea surface temperature, and atmospheric circulation in the summertime northeast Pacific. *J. Climate*, **8,** 140–155.

Klein, S. A., 1997: Synoptic variability of low-cloud properties and meteorological parameters in the subtropical trade wind boundary layer. *J. Climate*, **10,** 2018–2039.

Kiehl, J. T., J. J. Hack, and J. W. Hurrell, 1998: The energy budget of the NCAR Community Climate Model: CCM3. *J. Climate*, **11,** 1151–1178.

Larson, K., and D. L. Hartmann, 1999: The role of clouds, water vapor, circulation, and boundary layer structure in the sensitivity of the tropical climate. *J. Climate*, **13,** 2359–2374.

Lilly, D.K, 1968: Models of cloud-topped mixed layers under a strong inversion. *Q. J. R. Meteor. Soc*., **94,** 292–309.

Lindzen R.S. and S. Nigam, 1987, On the Role of Sea Surface Temperature Gradients in Forcing Low-Level Winds and Convergence in the Tropics, JAS.

Lorenz, Edward N. (1963). "Deterministic Nonperiodic Flow." *J. Atmospheric Sciences* **20**: 130-41.

Mapes, B., and R. A. Houze, JR., 1992: An integrated view of the 1987 Australian monsoon and its mesoscale convective systems. I: Horizontal structure. *Q. J. R. Meteor. Soc*., **118**, 927-963.

Mansbach, D., and J. Norris, 2006: Low-level cloud variability over the equatorial cold tongue in observations and models, *J. Climate*, submitted.

Monahan, A.H., 2005: Stochastic Dynamics of Sea Surface Winds. Proceedings, Workshop on Representation of Sub-Grid Processes Using Stochastic Dynamic Models, ECMWF, 6-8 June 2005.

Monahan, A.H., 2006: The Probability Distribution of Sea Surface Wind Speeds. Part I: Theory and SeaWinds Observations, *J. Climate*, **19**, 497-520, 2006.

Neelin J. D. and N. Zeng, 2000: A Quasi-Equilibrium Tropical Circulation Model-Formaulation, *J. Atmos. Sci.*, **57**, 1741-1766.

Nigam S., The annual warm to cold transition in the eastern equatorial Pacific: diagnosis of the role of stratus cloud-top cooling, *J. Climate*, 1997, 2447-2467.

Norris, J.R., 1994: On the relationships among low-cloud structure, sea surface temperature and atmospheric circulation in the summertime northeast pacific. *J. Climate*, **8,** 1140–1155.

Norris, J.R. and C. B. Leovy, 1994: Interannual variability in stratiform cloudiness and sea surface temperature. *J. Climate*, **7,** 915–925.

Norris, J.R, 1997: Synoptic variability of low-cloud properties and meteorological parameters in the subtropical trade wind boundary layer. *J. Climate*, **10,** 1018–1039.

Norris, J.R., 1998a: Low cloud type over the Ocean from Surface Observations. PART I: Relationship to Surface Meteorology and the Vertical Distribution of Temperature and Moisture. *J. Climate*, **11**, 369-382.

Norris, J.R., 1998b: Low cloud type over the Ocean from Surface Observations. PART II: Geographical and Seasonal Variations. *J. Climate*, **11**, 369-382.

Parker, D. J., 2002, The response of CAPE and CIN to tropospheric thermal variations. *Q. J. R. Meteor. Soc.*, **128**, 119-130.

Park S, and C.B. Leovy, 2004, Marine low-cloud anomalies associated with ENSO. *J. Climate, **17**, 3448-3469.*

Petersen, E. L., N. G. Mortensen, L. Landberg, J. Hojstrup, and H. P. Frank, 1998: Wind power meteorology. Part I: Climate and turbulence. *Wind Energy*, **1**, 25-45.

Randall, D. A., 1980, Entrainment to stratocumulus layer with distributed radiative cooling. *J. Atmos. Sci.*, **37,** 148–159.

Randall, D.A., and J. Wang, 1992: The moist available energy of a conditionally unstable atmosphere, *J. Atmos. Sci.*, **49**, 240-255.

Rossow, W. B. and Y. C. Zhang, 1995: Calculation of surface and top of atmosphere radiative fluxes from physical quantities based on ISCCP data sets 2: validation and first results. *JGR*, **100,** D1, 1167–1197.

Rossow, W.B. and R.A. Schiffer, 1991: ISCCP Cloud Data Products, *BAMS*, **72**, 1-20.

Rozendaal MA, Rossow WB, 2003: Characterizing some of the influences of the general circulation on subtropical marine boundary layer clouds, *JAS*, **60**, 711-728.

Siebesma, A. Pier, et al, 2003: Cloud representation in general circulation models over the northern Pacific Ocean: A EUROCS intercomparison study. *Q. J. R. Meteorol. Soc*. 130, 3245-3267.

Slingo, J. M., 1980: A cloud parameterization scheme derived from GATE data for use with a numerical model. *Q. J. R. Meteorol. Soc*. **106,** 747–770.

Slingo, J.M., 1987: The development and verification of a cloud prediction scheme for the ECMWF model, *Q. J. R. Meteorol. Soc.*, **113,** 899–927.

Smagorinsky, J., 1960: On the dynamical prediction of large-scale condensation by numerical methods. *Geophys. Mon.*, **5,** 71–78. American Geophysical Union, Washington, U.S.A.

Smith, R. N. B., 1990: A scheme for predicting layer clouds and their water content in a general circulation model. *Q. J. R. Meteorol. Soc.*, **116,** 435–460.

Stevens, B., W. R. Cotton, G. Feingold, and C. Moeng, 1998, Large-eddy simulations of strongly precipitating, shallow, stratocumulus-topped boundary layers. *J. Atmos. Sci.*, **55,** 3136–3638.

Stevens, B., 2002: Entrainment in stratocumulus topped mixed layers, *Q.J.R.Meteorol. Soc.*, **128**, 2663-2690.

Stevens, B., 2005, Atmospheric moist convection. *Annu. Rev. Earth Planet. Sci.*, **33**, 605-643.

Stevens, B., Y. Zhang, and M. Ghil, 2006: Stochastic effects in the representation of stratocumulus-topped mixed layers. *ECMWF Workshop on Representation of Sub-grid Processes Using Stochastic-Dynamic Models,* June 2005, Shinfield Park, Reading, UK.

Sundqvist, H., 1988: Parameterization of condensation and associated clouds in models for weather prediction and general circulation simulation. Physically-Based Modelling and Simulation of Climate and Climate Change, M. E. Schlesinger, Ed., Kluwer, 433–461.

Tailleux, R., and J. Y. Grandpeix, 2004: On the seemingly incompatible parcel and globally integrated views of the energetics of triggered atmospheric deep convection over land. *Q. J. R. Meteor. Soc*., **130**, 3223-3243.

Teixeira, J., 2001: Cloud fraction and relative humidity in a prognostic cloud fraction scheme, *Monthly Weather Review*, **129,** 1750–1753.

Tiedtke, M., 1993: Representation of clouds in large-scale models. *Monthly Weather Review*, **12,** 3040–3061.

Thompson, K, R. Marsden, and D. Wright, 1983: Estimation of low-frequency wind stress fluctuations over the open ocean. *J. Phys. Oceanogr.*, **13**, 1003-1011.

Tompkins, A., 2001: A prognostic parameterization for the subgrid-scale variability of water vapor and clouds in large-scale models and its use to diagnose cloud cover. *J. Atmos. Sci., **59,*** 1917–1942.

Torrence C. and G.P. Compo, 1998: A practical guide to wavelet analysis. *BAMS*, **79**, 61-78.

Wanninkhof, R., S. C. Doney, T. Takahashi, and W. R. McGillis: 2002, The effect of using time-averaged winds on regional air-sea CO2 fluxes. *Gas Transfer at Water Surfaces,* M. A. Donelan, W. M. Drennan, E. S. Saltzman, and R. Wanninkhof, eds., American Geophysical Union, 351-356.

Wood, R., and C. Bretherton, 2006a: On the relationship between stratiform low cloud cover and lower tropospheric stability. *J. Climate,* submitted.

Wood, R., and D.L. Hartmann, 2006b: Spatial variability of liquid water path in marine boundary layer clouds. Part I: the importance of mesoscale cellular convection. *J. Climate*, **19**, 1748-1764.

Zhang, G. J., and N. A. McFarlane, 1995: Sensitivity of climate simulations to the parameterization of cumulus convection in the Canadian Climate Centre general circulation model, *Atmosphere-Ocean*, **33**, 407–446.

Zhang, Y.-C., W. Rossow, and A.A. Lacis, 1995: Calculation of surface and top of atmosphere radiative fluxes from physical quantities based on ISCCP data sets 1: method and sensitivity to input data uncertainties. *JGR*, **100,** D1, 1149 –1165.

Zhang, Y.-C., W. Rossow, and A. A. Lacis, V. Oinas, and M. I. Mishchenko (2004), Calculation of radiative fluxes from the surface to top of atmosphere based on ISCCP and other global data sets: Refinements of the radiative transfer model and the input data, J. Geophys. Res., **109,** D19105, doi: 10.1029/2003JD004457.

Zhang, Y., J.M. Wallace, and D.S. Battisti, 1997: ENSO-like interdecadal variability: 1900-93: *J. Climate,* 10, 1004-1020.

Xu HM., Wang YQ, Xie SP, 2004: Effects of the Andes on eastern Pacific climate: A regional atmospheric model study, *J.Climate* **17**, 589-602.

Xu HM., Xie SP, Wang YQ, 2005: Subseasonal variability of the southeast Pacific stratus cloud deck “, *J.Climate,* **18**, 131-142.

Wyant MC, Bretherton CS, Bacmeister JT, Kiehl JT, Held IM, Zhao M, Klein SA, Soden BJ (2006) A comparison of low-latitude cloud properties and their response to climate change in three AGCMs sorted into regimes using mid-tropospheric vertical velocity. *Climate Dynamics,* **27**(2-3), 261.